

12-2019

## Wall-Jet Turbulence and Mixing Control by Way of a Pulsed Inlet Velocity

Cristale D. Garnica Vallejo

Follow this and additional works at: <https://commons.erau.edu/edt>

 Part of the [Aerospace Engineering Commons](#)

---

This Thesis - Open Access is brought to you for free and open access by Scholarly Commons. It has been accepted for inclusion in Dissertations and Theses by an authorized administrator of Scholarly Commons. For more information, please contact [commons@erau.edu](mailto:commons@erau.edu).

WALL-JET TURBULENCE AND MIXING CONTROL BY WAY OF A PULSED  
INLET VELOCITY

A Thesis

Submitted to the Faculty

of

Embry-Riddle Aeronautical University

by

Cristale D. Garnica Vallejo

In Partial Fulfillment of the

Requirements for the Degree

of

Master of Science in Aerospace Engineering

December 2019

Embry-Riddle Aeronautical University

Daytona Beach, Florida

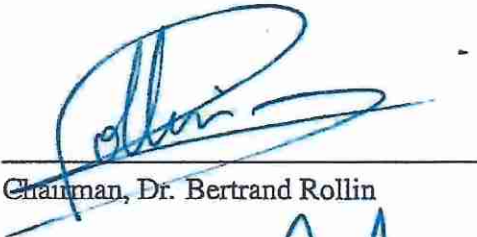
WALL-JET TURBULENCE AND MIXING CONTROL BY WAY OF A PULSED  
INLET VELOCITY

by

Cristale D. Garnica Vallejo

A Thesis was prepared under the direction of the candidate's Thesis Committee Chair, Dr. Bertrand Rollin, Department of Aerospace Engineering, and has been approved by the members of the thesis committee. It was submitted to the Office of the Senior Vice President for Academic Affairs and Provost, and was accepted in partial fulfillment of the requirements for the Degree of Master of Science in Aerospace Engineering.

THESIS COMMITTEE



---

Chairman, Dr. Bertrand Rollin



---

Member, Dr. Ebenezer Gnanamanickam



---

Member, Dr. Reda Mankbadi



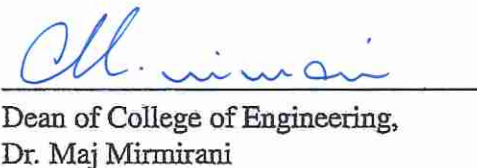
---

Graduate Program Coordinator,  
Dr. Magdy Attia

12-5-2019

---

Date



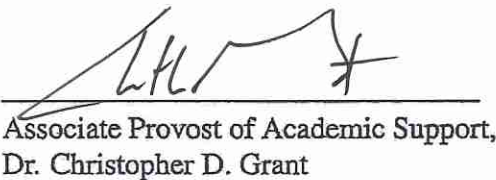
---

Dean of College of Engineering,  
Dr. Maj Mirmirani

12/5/2019

---

Date



---

Associate Provost of Academic Support,  
Dr. Christopher D. Grant

12/5/19

---

Date

## ACKNOWLEDGMENTS

I would like to express my gratitude to the individuals who helped me accomplish this work. Firstly, I would like to express my sincere recognition to my advisor Dr. Bertrand Rollin for the continuous support and great guidance throughout my graduate studies.

In addition to my advisor, I would like to thank the rest of my thesis committee: Dr. Gnanamanickam and Dr. Mankbadi, for their insightful comments and contribution to this work.

I am very grateful for Christina Groenenboom and her family who provided me with unfailing support and continuous encouragement throughout my years of study. A special thank you to my loving partner, Adam Berlier, who has been there for me in every step and my caring friends, especially Patricia Velasco, who has gone through this journey with me. Thank you for the countless stimulating discussions, for the sleepless nights working together, and for all the fun we have had.

Last but not least, this work is dedicated to my loving family that despite the distance they have been the inspiration for my success, without their support this accomplishment could not be possible.

## TABLE OF CONTENTS

	Page
LIST OF TABLES . . . . .	vi
LIST OF FIGURES . . . . .	vii
SYMBOLS . . . . .	xii
ABBREVIATIONS . . . . .	xiv
ABSTRACT . . . . .	xv
1. Introduction . . . . .	1
1.1. Motivation . . . . .	1
1.2. Wall-Jet Physical Description . . . . .	2
1.3. Review of Previous Work . . . . .	4
1.4. Scope and Outline . . . . .	16
2. Analysis Tools for Wall-Bounded Turbulent Flows . . . . .	17
2.1. Statistical Description of Turbulent Flows . . . . .	17
2.1.1. Mean Flow Properties . . . . .	19
2.1.2. Turbulent Statistics and Kinetic Energy . . . . .	20
2.1.3. Scaling Parameters . . . . .	24
2.2. Turbulent Structures . . . . .	26
2.3. Kelvin-Helmholtz Instability . . . . .	32
2.4. DNS Approach . . . . .	33
3. Numerical Method . . . . .	35
3.1. PyFR . . . . .	35
3.1.1. Spatial Discretization . . . . .	36
3.1.2. Time Discretization . . . . .	42
3.2. Nek5000 . . . . .	43
3.2.1. Spatial Discretization . . . . .	45
3.2.2. Time Discretization . . . . .	50
3.2.3. Tripping Force . . . . .	51
4. Compressible Wall-Jet . . . . .	54
4.1. Computational Set-up . . . . .	54
4.1.1. Inlet and Boundary Conditions . . . . .	55
4.2. Results . . . . .	57
4.2.1. Instantaneous Fields . . . . .	57
4.2.2. Mean Flow Characteristics . . . . .	59

	Page
4.2.3. Turbulent Statistics . . . . .	64
4.3. Conclusions . . . . .	66
5. Incompressible Wall-Jet . . . . .	69
5.1. Computational Set-up . . . . .	69
5.1.1. Inlet and Boundary Conditions . . . . .	70
5.2. Refinement Study . . . . .	74
5.2.1. Mean Flow Characteristics . . . . .	74
5.2.2. Turbulent Statistics . . . . .	77
5.3. Detailed Statistical Analysis . . . . .	79
5.3.1. Instantaneous Velocity Characteristics . . . . .	79
5.3.2. Mean Flow Characteristics . . . . .	85
5.3.3. Turbulent Statistics . . . . .	91
5.3.4. Turbulent Structures . . . . .	99
5.4. Perturbation Parametric Analysis . . . . .	103
5.5. Conclusions . . . . .	110
6. Summary and Future Work . . . . .	112
REFERENCES . . . . .	118

## LIST OF TABLES

Table	Page
3.1. PyFR Capabilities . . . . .	36
3.2. NEK5000 Capabilities . . . . .	44
4.1. Compressible Case Study Description . . . . .	56
5.1. Incompressible Case Study Description . . . . .	72
5.2. Incompressible Case - Mesh Description . . . . .	73

## LIST OF FIGURES

Figure	Page
1.1. Schematic Representation of a Planar Wall-Jet. . . . .	3
1.2. A still shot of a PWJ shear layer showing the formation and evolution of the Kelvin-Helmholtz instability (Gnanamanickam et al., 2017). . . . .	9
1.3. Mean streamwise velocity and turbulent kinetic energy (tke) profiles at 30h for outer and inner scaling respectively (Naqavi et al., 2018). . . . .	13
2.1. Reynolds Decomposition of $u_i$ . . . . .	20
2.2. Kelvin-Helmholtz Instability Evolution described by Gogineni and Shih (1997). . . . .	27
2.3. Schematic diagram showing different turbulent fluid motions according to quadrant analysis procedure (Saha et al., 2017). . . . .	28
2.4. (a) Schematic of a hairpin eddy attached to the wall; (b) signature of the hairpin eddy in the streamwise-wall-normal plane (Adrian et al., 2000). . . . .	29
2.5. Iso-surfaces of the second invariant of the velocity gradient tensor in the wall jet (Naqavi et al., 2017). . . . .	31
2.6. Kelvin-Helmholtz Instability Evolution. . . . .	32
3.1. Solution points (blue) and flux points (orange) in a triangular and quadrilateral element in physical space. The normal vectors for the quadrilateral element are represented in black (Witherden et al., 2014). . . . .	39
3.2. Point distributions for velocity and pressure using $P_N - P_{N-2}$ method by Paul F. Fischer and Kerkemeier (2008). . . . .	46
3.3. Spectral element methods (SEM) grid (Offermans, 2017). . . . .	48
3.4. Mapping between local (left) and global (right) numbering for a domain of two spectral elements (Offermans, 2017). . . . .	49
4.1. Compressible Wall-Jet Mesh. . . . .	55
4.2. Compressible Wall-Jet Boundary Conditions. . . . .	56



Figure	Page
4.3. Instantaneous velocity, density, and pressure fields for the three compressible case at $t = 6.75s$ . Red square highlights pure Kelvin-Helmholtz instabilities, black rectangle the vortices produce by the roughness, and the yellow oval focuses on the primary and secondary vortex process undergoing the flow. . . .	58
4.4. Decay of maximum mean stream-wise velocity, $U_m$ as a function of the streamwise position normalized with the inlet height. Data compared to Tang et al. (2015) blue line and Barenblatt et al. (2005) red line. . . . .	60
4.5. Wall-normal position $y_m$ of the maximum mean stream-wise velocity $U_m$ as a function of the over stream-wise position $x$ . Values normalized by the inlet height. Data compared to Tang et al. (2015) magenta dashed line and Naqavi et al. (2018) green $\diamond$ . . . . .	61
4.6. Skin friction coefficient as a function of the local Reynolds number. Data compared to Tachie et al. (2004). . . . .	62
4.7. Mean stream-wise velocity profiles scaled using outer parameters. Data compared to Naqavi et al. (2018). . . . .	63
4.8. Mean stream-wise velocity profiles scaled using inner parameters. Left figure $x/h = 20$ and right figure $x/h = 30$ . Blue line $\langle u^+ \rangle = y^+$ and red line $\langle u^+ \rangle = A \ln(y^+) + B$ . . . . .	64
4.9. Reynolds stresses profiles at two stream-wise positions scaled with outer parameters. Left figure stream-wise $\langle u'u' \rangle$ - right figure $\langle v'v' \rangle$ . . . . .	65
4.10. Reynolds stresses profiles at two stream-wise positions scaled with inner parameters. Top figures stream-wise $\langle u'u' \rangle$ - bottom figures $\langle v'v' \rangle$ . . . . .	66
5.1. Incompressible Wall-Jet Boundary Conditions. . . . .	70
5.2. High resolution mesh with $E_x = 30 \times E_y = 30 \times E_z = 4$ . . . . .	72
5.3. Mean streamwise and normal velocity at various streamwise positions ( $x/h = 25, 31.25, 37.5$ ) for the baseline and the forced case ( $Sr = 0.0048$ with $A = 0.1U_{in}$ ). . . . .	74
5.4. Mean streamwise velocity for the baseline and the force case at $x/h = 25$ . Data compared with Naqavi et al. (2018). . . . .	75
5.5. Skin friction coefficient as a function of the local streamwise position. Data is compared to the conventional $7^{th}$ power law and the $7^{th}$ power law with empirical data. . . . .	76

Figure	Page
5.6. Decay of maximum mean streamwise velocity as a function of the streamwise position normalized by the inlet height. Data compared to Tang et al. (2015) orange line, George et al. (2000) purple line, and Barenblatt et al. (2005) yellow line. . . . .	77
5.7. Reynolds stresses and turbulent kinetic energy profiles scaled with outer parameters. a. streamwise $\langle u'u' \rangle$ - b.wall-normal $\langle v'v' \rangle$ - c.spanwise $\langle w'w' \rangle$ and d. turbulent kinetic energy $\langle k' \rangle$ . . . . .	78
5.8. Instantaneous velocity in an xy plane at $t = 0.0504s$ . Figures at the left present results for low resolution grid, and figures at the right presents results for high resolution grid. . . . .	81
5.9. Instantaneous velocity in an xz plane at $t = 0.0504s$ . Figures are taken at $y^+ \sim 7$ . Left figures present results for low resolution grid, and right figures presents results for high resolution grid. . . . .	83
5.10. Instantaneous velocity in an xz plane at $t = 0.0504s$ at two positions $x/h = 30$ and $x/h = 40$ . Left figures show results for low resolution grid, and right figures show results for high resolution grid. . . . .	84
5.11. Mean stream-wise and normal velocity at positions $x/h = 30$ and $35$ , left and right figures respectively. For the baseline and the forced case ( $f = 12Hz$ with <i>Amplitude</i> = $0.4U_{in}$ ) the low resolution and high resolution grids are compared with Naqavi et al. (2018). . . . .	85
5.12. Normal velocity at positions $x/h = 35$ . For the baseline and the forced case ( $f = 12Hz$ with <i>Amplitude</i> = $0.4U_{in}$ ) the low resolution and high-resolution grids. Excludes low-resolution baseline for close-up. Data compared with Naqavi et al. (2018). . . . .	86
5.13. Mean streamwise velocity for the baseline and the force case at $x/h = 30$ (solid line) and $x/h = 35$ (dashed line). Data compared with Naqavi et al. (2018) and with conventional scaling functions for turbulent boundary layers. . . . .	87
5.14. Decay of maximum mean streamwise velocity, $U_m$ as a function of the streamwise position normalized with the inlet height. Data compared to Tang et al. (2015) dashed magenta line and Banyassady and Piomelli (2014) red dashed line. . . . .	88
5.15. Wall-normal position $y_m$ of the maximum mean streamwise velocity $U_m$ as a function of the local streamwise position $x/h$ . Data compared to Tang et al. (2015) green dashed line and Naqavi et al. (2018) red dashed line. . . . .	89

Figure	Page
5.16. Wall jet spreading rate in the outer region. Data compared to Naqavi et al. (2018) blue line, Tang et al. (2015) red line, and Launder and Rodi (1983) yellow line. . . . .	89
5.17. Wall jet spreading rate in the inner region. Data compared to Naqavi et al. (2018) blue line, and Tang et al. (2015) red line. . . . .	90
5.18. Skin friction coefficient as a function of the local streamwise position. Data is compared to the conventional $7^{th}$ power law. . . . .	91
5.19. Reynolds stresses and turbulent kinetic energy profiles scaled with outer parameters. a. streamwise $\langle u'u' \rangle$ - b.wall-normal $\langle v'v' \rangle$ - c.spanwise $\langle w'w' \rangle$ and d. turbulent kinetic energy $\langle k' \rangle$ . Data compared to Naqavi et al. (2018) at $x/h = 30$ (blue $\star$ ) and $x/h = 30$ (orange $\blacksquare$ ) and LES data by Banyassady and Piomelli (2014) (yellow $\blacklozenge$ ). . . . .	93
5.20. Reynolds stresses and turbulent kinetic energy profiles scaled with inner parameters. a. streamwise $\langle u'u' \rangle$ - b.wall-normal $\langle v'v' \rangle$ - c.spanwise $\langle w'w' \rangle$ and d. turbulent kinetic energy $\langle k' \rangle$ . Data compared to Naqavi et al. (2018) at $x/h = 30$ (blue $\star$ ) and $x/h = 30$ (orange $\blacksquare$ ) and LES data by Banyassady and Piomelli (2014) (yellow $\blacklozenge$ ). . . . .	94
5.21. Outer scaled Reynolds shear stress profiles at $x/h = 30$ and $x/h = 35$ . Data is compared with Naqavi et al. (2018). . . . .	95
5.22. Inner scaled Reynolds shear stress profiles at $x/h = 30$ and $x/h = 35$ . Data is compared with Naqavi et al. (2018). . . . .	96
5.23. Profiles of triple velocity correlations scale with inner variables. Data compared with Eriksson (2003) (magenta), and Naqavi et al. (2018)(green). . . . .	98
5.24. Instantaneous vorticity field at $t = 0.08s$ of the high resolution baseline (top) and the forced case (bottom). . . . .	100
5.25. Iso-surfaces associated to the Q-criterion for the outer layer of the baseline (top) and the forced case (bottom). The iso-surfaces are coloured with local velocity magnitude. . . . .	101
5.26. Iso-surfaces associated to the Q-criterion for the inner layer of the baseline (top) and the forced case (bottom). The iso-surfaces are coloured with local velocity magnitude. . . . .	102

Figure	Page
5.27. Instantaneous velocity in an xy plane at the high peak velocity. Figures at the top present results for $f = 12Hz$ at $20\%U_{in}$ (left) and $40\%U_{in}$ (right), and figures at the bottom presents results for $f = 50Hz$ at $20\%U_{in}$ (left) and $40\%U_{in}$ (right). . . . .	105
5.28. Instantaneous velocity in an zy plane at the high peak velocity. Figures at the top present results for $f = 12Hz$ at $20\%U_{in}$ (left) and $40\%U_{in}$ (right), and figures at the bottom presents results for $f = 50Hz$ at $20\%U_{in}$ (left) and $40\%U_{in}$ (right). . . . .	106
5.29. Instantaneous velocity in an xy plane at the low peak velocity. Figures at the top present results for $f = 12Hz$ at $20\%U_{in}$ (left) and $40\%U_{in}$ (right), and figures at the bottom presents results for $f = 50Hz$ at $20\%U_{in}$ (left) and $40\%U_{in}$ (right).	108
5.30. Instantaneous velocity in an xz plane at the low peak velocity. Figures at the top present results for $f = 12Hz$ at $20\%U_{in}$ (left) and $40\%U_{in}$ (right), and figures at the bottom presents results for $f = 50Hz$ at $20\%U_{in}$ (left) and $40\%U_{in}$ (right).	109

## SYMBOLS

$u$	velocity
$M$	Mach number
$\rho$	Density
$\mu$	Dynamic viscosity
$\nu$	Kinematic viscosity
$h$	Jet inlet height
$U_m$	Maximum stream-wise velocity
$U_c$	Co-flow velocity
$U_{in}$	Inlet velocity
$u'$	Fluctuation velocity
$U$	Mean velocity
$u_\tau$	Friction velocity
$y_m$	Position of $U_m$
$y_{1/2}$	Position of half width $(U_m - U_c)/2$ or $U_m/2$
$y_{1/2(in)}$	Position of inner half width $U_m/2$
$y^+$	Wall units
$u, v, w$	Stream-wise, wall-normal and spanwise velocity
$P$	Pressure
$Re$	Reynolds number
$k$	Turbulent kinetic energy
$\tau$	Shear stress
$\sigma_i$	Standard deviation of property $i$
$\langle \rangle$	Mean
$x'$	Fluctuation of property $x$
$f$	Frequency

$t$	Time
$C_f$	Coefficient of friction
$E_x$	Element count in direction x
$N_x$	Gridpoint count in direction x
$Sr$	Strouhal number

## ABBREVIATIONS

BD	Backward Difference
DNS	Direct Numerical Simulation
EXT	Extrapolation Method
FD	Finite Difference
FE	Finite Element
FR	Flux Reconstruction
FV	Finite Volume
KHI	Kelvin-Helmholtz Instabilities
RK4	Runge Kutta 4th Order
RK5	Runge Kutta Fehlberg
RMS	Root Mean Squared
SEM	Spectral Element Method
PDF	Probability Density Function

## ABSTRACT

Understanding wall-jet-induced turbulence and mixing is an important challenge in modern engineering, as drag reduction and mixing enhancement are attainable by modifying the flow development. Simulations are performed to investigate the effect on skin friction and flow mixing due to introducing controlled perturbations, at the initial shear layer of a planar wall-jet using jet inlet cyclic pulsing. The billow production by the Kelvin-Helmholtz instability, the instability that drives turbulence in a wall-jet, is modified by the excitation of the inlet velocity profile by a sine wave perturbation. Two types of wall-jet simulations are carried out, a two-dimensional compressible case at  $Re_{in} = 5000$  using the PyFR solver and a three-dimensional incompressible case at  $Re_{in} = 6000$  using the Nek5000 solver. The compressible wall-jet simulation indicates that the addition of a sine wave perturbation of 1% on the inlet velocity, at the initial shear layer, increases the wall-normal turbulence intensity at a Strouhal number (Sr) of 0.05 and reduces the turbulence intensity in all directions at a Sr of 0.25. The incompressible wall-jet simulations show that a perturbation of magnitude 40% of the inlet velocity at a low Sr number of 0.0048 damps turbulence and leads to skin friction reduction. The forced wall-jet experiences a repetitive re-laminarization process that delays transition as well as separation from the wall. A qualitative parametric analysis of the perturbation of the global behavior of the flow development on a plane wall-jet under forced velocity profiles is also presented. Cases at  $Sr = 0.0048$  experience a reduction in the number of turbulent structures while becoming more stable, indicating potential drag reduction. Cases at  $Sr = 0.02$  experience a frequent energy re-supply from the inlet that helps



maintain large turbulent structures at further downstream locations, useful for mixing related applications.

## 1. Introduction

In a rapidly evolving world, modern technologies search new techniques to modify turbulence and turbulence flows. The ability to manipulate the flow development as desired is of immense practical importance. To enhance aerodynamics performance, improve heat transfer capabilities, and reduce noise, flow control techniques provide different methods to manipulate boundary layers structure, vortices and wake flow for engineering benefits. Flow control uses the fluid mechanics knowledge of a certain phenomenon to affect the evolution of a flow. For instance, modifying large scale structures in a wall-bounded flow to reduce skin friction, delaying separation point on an airplane wing to enhance aerodynamic performance, or triggering turbulence to increase the mixing in a combustion chamber.

### 1.1 Motivation

Multiple types of flow control strategies such as active, passive, open-loop, closed-loop, etc. have been developed and studied over the years, and some have provided significant engineering advantages. The focus of this study will involve flow control applied to wall-bounded flows and specifically to wall-jets. Wall-jets are a very common flow configuration in nature and the turbulent wall-jet dynamics include interesting phenomena with close resemblance to numerous engineering applications related to fluid mechanics, aerodynamics, and heat transfer. Therefore, the study of wall-jets is of paramount importance for arising applications in thermal protection, mixing, combustion, and noise generation. In a practical example, wall-jets are employed for film-cooling the lining walls of gas-turbine combustion chambers. A cool layer of fluid parallel to the wall is introduced to provide protection from a hot external stream. This layer behaves as a

wall-jet and it is used to modify the heat and mass transfer by Launder and Rodi (1983). Further, wall jets are used to enhance the internal mixing in the near-wall of combustion chambers. The efficiency of mixing rates plays a key role in combustion and thermal efficiency, and engine-out emissions (Pouransari et al., 2011).

In the case of separation control, the manipulation of the flow aims to achieve enhanced near-wall momentum and increased mixing between the wall jet and the outer flow to suppress separation (Naqavi et al., 2018). On the other hand, for film-cooling applications, the jet, and ambient flow should reduce mixing between layers. The versatility of this flow configuration is shown with the opposite requirements for these applications. To obtain maximum benefit from modifying the turbulence in the flow one requires a better understanding of the flow development with and without control measurements. In addition to its diverse applications, a wall jet is a practical flow configuration for resolving the intricate interactions between the layers structures in a turbulent boundary layer. This particular flow provides a larger degree of flexibility and controllability of flow parameters than a boundary layer. Consequently, one can alter the vorticity in the outer layer without a concomitant alteration in the momentum input which might also change the susceptibility of the wall jet to external perturbations (Katz et al., 1992).

## **1.2 Wall-Jet Physical Description**

A wall-jet is obtained when a stream of fluid is directed tangentially along a flat surface in the presence or absence of an external stream. Different types of wall-jet can arise depending on the type of jet, wall-boundary and inlet conditions, nozzle geometry and flow injection. Despite variety in type, all wall-jets are characterized by similarities with

two distinct flow regimes: (i) An inner flow stream from the wall to the maximum stream-wise velocity, which behaves like a conventional boundary layer and (ii) An outer stream from the maximum stream-wise velocity to the ambient flow is similar to a canonical free shear flow. This simplified view is an incomplete description of the flow configuration, because of the interaction between the inner and outer layers which creates a unique complex flow field, where different kinds of large scale structures from each layer interact with each other causing turbulence. Considering the presence of the wall constraint combined with the structure interaction, the flow field is a single interacting wall-bounded flow entailing turbulent structures that resemble those seen in a free shear layer as well as within boundary layers (Gnanamanickam et al., 2019).

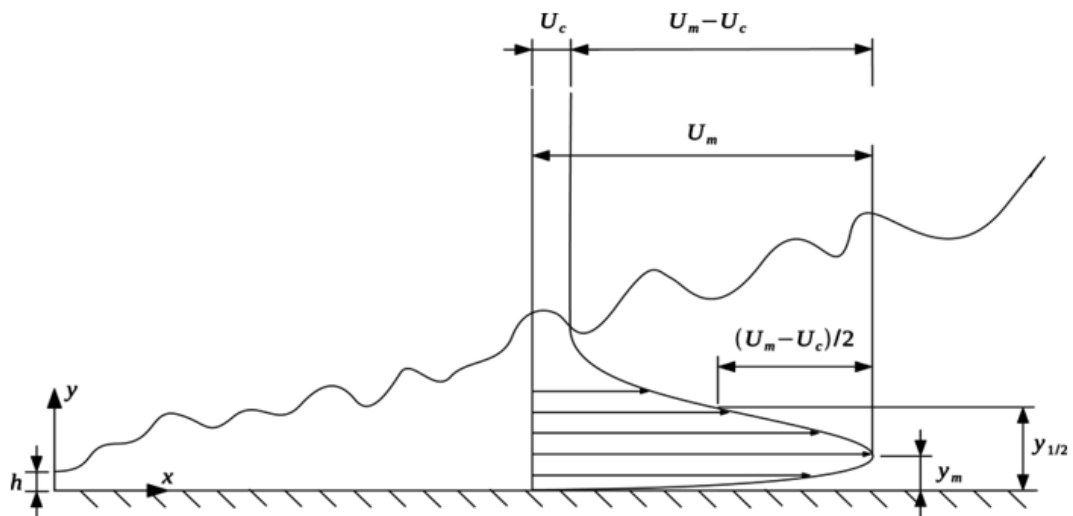


*Figure 1.1* Schematic Representation of a Planar Wall-Jet.

Figure 1 shows the schematic of a plane turbulent wall-jet with an external stream, where the inlet height of the jet is represented by  $h$ . The maximum streamwise velocity,

$U_m$ , separates the two characteristic layers on the flow, and  $y_m$  is the correspondent wall-normal position.  $U_c$  is the velocity of the external stream or co-flow being deployed to ensure large vortices propagate out of the domain. The parameter  $y_{1/2}$  denotes the wall-normal location where  $U = U_m/2$  for a wall-jet without external stream and  $U = (U_m - U_c)/2$  for a wall-jet with a co-flow and it is used for outer scaling. There is also a half-width denoted  $(y_{1/2})_{in}$  correspondent to  $U = U_m/2$  which characterizes the thickness of the inner region.  $(y_{1/2})_{in}$  is not shown in Fig. 1.1, but is a common length scale used for inner scaling. The inlet wall jet Reynolds number can be defined as  $Re = U_{in}h/\nu$ , where  $h$  is the slot height,  $U_{in}$  is the jet slot exit velocity and  $\nu$  is the kinematic viscosity.

### 1.3 Review of Previous Work

The term "wall-jet" was formally introduced by Glauert in 1956 and provides the first similar solution known for the flow configuration (Glauert, 1956). The solution proposed by Glauert consists of the division of the flow into two layers. First, the inner layer is considered as a boundary layer with a freestream velocity corresponding to  $U_m$  and a boundary layer thickness equivalent to  $y_m$ . Second, the outer layer is described as free-shear flow, which initial point is  $y_m$  and expands to the ambient conditions. This solution was also considered by Schwarz and Cosart (1961) and Myers et al. (1963) in their corresponding work. However, this simple description was discarded as a complete similarity due to the lack of fidelity in predictions. On one hand, the inner layer behaves closely to a boundary layer, but due to the interaction with the outer layer, the behavior is not identical. On the other hand, the outer wall is influenced by the presence of the wall

and it does not expand like a perfect free-jet (Glauert, 1956). In an attempt to determine suitable scaling laws for wall-jets, multiple experimental and computational studies have been performed over the years. Two compilations of this work are papers by Launder and Rodi (1983) for studies before 1980, in which they provide a review over theoretical, experimental and early RANS studies. Banyassady and Piomelli (2014) presented a review for later studies.

To explain the behavior of both layers, the studies sought scaling laws for the mean profiles based on different parameters such as jet inlet, Reynolds number, and viscosity. Among the experimental studies, it has been found that the wall-jet reaches self-similarity at a streamwise distance greater than 20 times the inlet height. This conclusion was drawn from the jet spreading rate, scaled by the jet half-height ( $y_{1/2}$ ). Using this, Wygnanski et al. (1992) and Irwin (1973) found good scaling agreement on the mean velocity profile by using  $y_{1/2}$  and  $U_m$ . However, Wygnanski et al. (1992) showed that second-order turbulent statistics do not converge using this conventional outer scaling lengths. Narasimha et al. (1973) proposed a different perspective than the traditional scaling parameters by scaling the mean properties by the inlet momentum flux and the kinematic viscosity. After reconsideration and analysis on Narashima's parameters, Launder and Rodi (1983) discarded the novel parameters because of poor two-dimensionality on the data sets.

George et al. (2000), suggested that there is a possibility of a complete similarity solution as the Reynolds becomes infinitely large. Hence, at finite Reynolds number, there might not be suitable scaling laws that can collapse all the data (George et al., 2000). This conclusion is drawn by the wide separation of scales inevitably present between the

near-wall region and the outer shear layer. The inner region turbulence is governed by the near-wall effects, where characteristic scales end to the viscous boundary layer scales whereas the turbulence in the outer region is governed by the free shear layer scales, where the turbulence scales are similar to those found in free-shear flows. For inner scaling, George et al. (2000) proposed friction velocity,  $u_\tau$  and  $v/u_\tau$  for the stream-wise and the normal direction respectively on the inner layer.

For the outer layer, he proposed conventional outer scaling ( $y_{1/2}$  and  $U_m$ ) (George et al., 2000). The scaling proposed by George et al. (2000) is applied by Eriksson (2003) and Rostamy et al. (2011) in their respective studies, they found that the stream-wise mean velocity profile, as well as, Reynolds stresses scale with his parameters. Barenblatt et al. (2005) showed two self-similar layers in their study, outer and wall layer, where the slot inlet height is shown to have a strong influence on the flow development. The mean velocity profiles are scale using the maximum stream-wise velocity,  $U_m$  for both layers, while for the normal direction the correspondent length scale is  $y_{1/2}$  for the outer layer and  $(y_{1/2})_{in}$  for the wall layer (Barenblatt et al., 2005).

The experimental study of 2015, agrees with Barenblatt's scaling parameters as results collapsed in mean velocity profiles. Although scaling parameters agree for various studies, the near-wall region where the log-law ( $U^+ = Ay^+ + B$ , where  $A = 2.44$  and  $B = 5.0$  for a zero pressure gradient boundary layer) applies does not seem to find accordance for the planar wall-jet law constants. Few studies by (Eriksson et al., 1998) and Dejoan and Leschziner (2005) suggested that the law constants are the same as for a zero pressure

gradient boundary layer, however a wide range of studies present scatter data for these constants.

For a wall-jet in the presence of an external stream, the previous scaling does not converge perfectly, a wall jet does not present self-similarity with the same velocity and length scales as a wall-jet without external stream. By studying a wall-jet developed in a moving stream, Zhou and Wygnanski (1993) determine that the normalized mean velocity profile depends on two velocity scales and two length scales. These velocity and length scales are given by the momentum flux at the nozzle, the viscosity of the fluid, and the initial velocity ratio between the jet inlet and the freestream at the desired position defined by  $R = (U_j - U_\infty)/(U_j + U_\infty)$ . By applying different a series of jet velocity ratios  $M = \frac{U_j}{U_\infty}$  where  $U_j$  is the jet inlet velocity and  $U_\infty$  is the external stream, Naqavi et al. (2014) found that the scaling parameters for the outer region are dependent on the M range previously defined, while in the inner region parameters are almost independent of the inlet of M and scaling with inner parameters converged.

Additionally, Naqavi et al. (2014) discovered that wall-jets than maintained a ratio  $M < 1$  developed von Karman type shed vortices in the wake region, while ratios of  $M > 1$  endure Kelvin Helmholtz instabilities and the space between billows is narrow down. For wall-jets in a moving stream, the scaling for the outer region is mainly affected. To reduce scaling discrepancies, 2007 used an adjusted version of the traditional outer scaling,  $\frac{U-U_c}{U_m-U_c}$ , where the  $U_c$  term is the velocity of the external stream (Ahlman et al., 2007).

To understand the flow development over different circumstances, the influence of roughness over the surface was thoroughly studied by experiments and simulations.



Tachie et al. used multiple wall-jets with different types of surface roughness at a range of Reynolds numbers from 5900 to 12500 with the to study the effects of roughness over the surface using Laser Doppler Anemometry (LDA). Their study reported that surface roughness does not influence the spreading rate of the maximum mean velocity.

According to their results, skin friction increased between 15 % and 30 % when roughness was present on the surface. When analyzing the effects on the scaled outer layer, Tachie et al. (2004) found that the surface roughness does not have major influence in the Reynolds stresses. To study the repercussion on the flow mean characteristics and turbulence properties caused by surface roughness, Smith utilized Hot-Wire Anemometer over various wall-jets. Smith targeted the analysis of roughness physical size and wall-jet inlet Reynolds number to measure the streamwise Reynolds number. His study concluded that the Reynolds stresses are dependent on the Reynolds number and the roughness size. He suggested that at a given Reynolds number as the roughness size increases, the level of the stream-wise Reynolds stress decreases in the inner layer (Smith, 2008).

With more focus into the application of wall-jets, studies have revolved around understanding the inner-outer layer interaction and the development and synergy of large-scale structures. To analyze these parameters, one should study the turbulence characteristics of the flow including, turbulent structures, turbulent kinetic energy and Reynolds stress budgets for both layers. Bradshaw and Gee (1962) were pioneers on the study of turbulence on a wall-jet as they took the first measurements of turbulence quantities in a smooth wall jet configuration. In their study, a finite value of the shear stress at the point of stream-wise maximum velocity,  $U_m$ , was observed. To quantify the

turbulence phenomena, studies presented Reynolds stresses by the means of turbulence intensity or Reynolds Stress budgets.

Turbulence intensity for a planar wall-jet exhibits two characteristic peaks as shown in Figure 1.3. According to Zhou et al. (1996), the inner turbulence intensity peak occurs at  $y^+ \approx 15$  and has a lower magnitude than the outer peak. Naqavi et al. (2014) suggests that the near-wall Reynolds stresses and turbulence productions have strong boundary layer characteristics. The outer peak is analogous to the outer turbulence intensity peak seen in the adverse pressure gradient boundary layers (Harun et al., 2013). For the particular case of a planar wall-jet, Reynolds stresses are scaled by regions. The outer layer scales with squared maximum streamwise velocity,  $U_m^2$ , while the inner layer scales with squared friction velocity,  $u_\tau^2$  as suggested by Banyassady and Piomelli (2014).

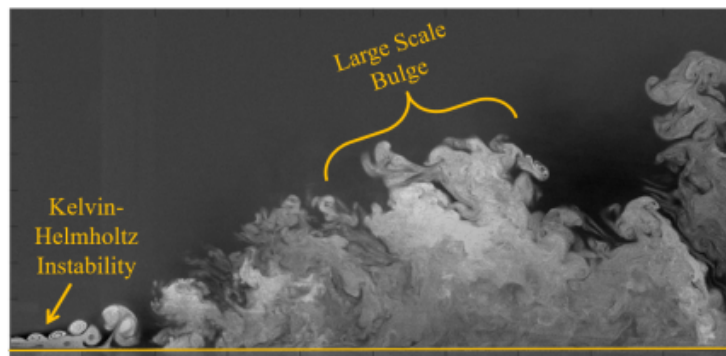


*Figure 1.2* A still shot of a PWJ shear layer showing the formation and evolution of the Kelvin-Helmholtz instability (Gnanamanickam et al., 2017).

On the experimental side, the only results related to turbulence analysis are presented by Irwin (1973) and Zhou and Wygnanski (1993). For experiments previous to Particle Image Velocimetry (PIV) flow visualization technique, measurements in the inner region were not achievable, hence, the turbulence analysis is performed just for the outer region.

Experimental results related to turbulence properties are a combination of measurements and assumptions, which includes extrapolation of data. Although experimental studies provide accurate sets of data, it exists multiple incentives that shift the attention to simulations.

Computational methods provide highly detailed and physically reliable information, which gives great insight into turbulence properties such as transitional features and confirming suggested scaling and similarities. One of the main advantages of simulations is the ability to determine Reynolds stresses budgets, which are fundamental to understand the layer interaction on a wall-jet configuration. Knowledge surrounding all scales of motion involved in wall-jet development demands numerical techniques such as Large Eddy Simulations (LES) and Direct Numerical Simulations (DNS). A highly resolved LES of a plane wall jet was performed by 2005 to identify turbulent mechanisms on the flow development. Their work captures a wall-jet at Reynolds number of  $Re = 9700$  and presents an analysis of turbulent kinetic energy and Reynolds stresses to interpret the variation of second moments. Dejoan and Leschziner (2005) concluded that turbulent diffusion transfers turbulent kinetic energy from the inner and outer layers to the interaction region. Compared to experimental studies, the earlier LES work has good agreement with Eriksson et al. (1998) experimental results.

A recent LES study is presented by Banyassady and Piomelli (2014), where the effect of roughness on the wall-jet surface is studied. Considering, a long domain up to  $35h$  at a Reynolds number of  $Re = 7500$ , where the flow reaches a fully developed state, they make a comparative analysis between smooth and rough surfaces wall-jets. These simulations

showed that roughness does not affect the outer layer. Therefore, turbulence structures and scaling parameters for the outer layer are not affected by the roughness. Their analysis led them to the conclusion that roughness redistributes wall-normal and spanwise turbulence towards isotropy. In a further study, Banyassady and Piomelli (2014) performed LES and used probability density functions to analyze layer dependency on planar and radial wall-jets. Banyassady and Piomelli (2015) in their conclusion they agreed with George et al. (2000), that the level of influence of the outer layer on the inner layer is practically zero for infinitely large Reynolds numbers and a larger scaling overlap region as local Reynolds number decreases.

Since the complexity of wall-jets causes the presence of particularly small scales it is important to utilize highly resolved direct numerical simulations (DNS). These studies require more computational power as the Reynolds numbers increases. Pioneering DNS studies on wall-jet were performed on the transitional regime and as computational power improved over time turbulent wall jet simulations have been refined. Visbal et al. (1998) presented a DNS study in the transitional regime with a focus on flow control as the wall-jet is being forced (Visbal et al., 1998). The study concluded that with adequate forcing amplitude the formation of phase-locked vortices is observed close to the jet exit. These vortices are transported stably for a two-dimensional wall-jet, while for a three-dimensional wall-jet these vortices caused the loss of coherence in both inner and outer regions.

One of the first DNS studies on turbulent and compressible isothermal wall-jet was carried out by Ahlman et al., which characterized the inner layer as a turbulent zero

pressure gradient boundary layer (from  $y^+ = 0$  to  $y^+ = 13$ ) and the outer layer as a free shear flow scaled with a self-similarity as plane jets. Their study was limited to a Reynolds number of 2000 and focuses on wall-jet dynamics and mixing properties.

Ahlman et al. (2007) studied inner and outer scalings showing self-similarity behavior at several downstream locations. Results were in good agreement with Ericksson's experimental study (Eriksson et al., 1998). Later, Ahlman et al. (2009) expanded their study by investigating turbulent and compressible non-isothermal wall-jets at higher Reynolds numbers. This study utilized a significant density gradient between the jet and the surroundings to analyze the development of the flow for combustion and cooling applications (Ahlman et al., 2009).

Ahlman's work is followed by a series of papers by Pouransari et al. (2011, 2013, 2014, 2015, 2016), who studied wall-jets flow characteristics and scalar concentration for combustion applications. These studies are confined to low Reynolds numbers between 2000 and 6000. Pouransari et al. (2013) aimed to analyze the effects of mixing related to chemical reaction and heat release. Some of the findings that were drawn by the simulations are, that heat release delays the transition and increases density, pressure, and species concentration fluctuations. By varying the Reynolds number, they concluded that the flames and turbulent structures thickness is reduced as the Reynolds number increases (Pouransari et al., 2014).

Naqavi et al. (2017) used DNS simulations on a wall-jet to study the heat transfer process. Their study presented scaling for thermal properties including mean temperature and wall-normal heat fluxes. The resulting mean velocity, Reynolds stresses, and thermal

scaling converged and compared well with the available data from various wall jet studies (Naqavi et al., 2017).

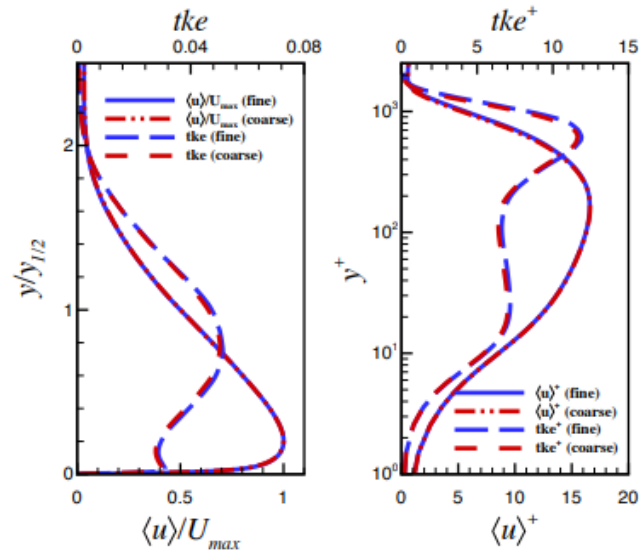


Figure 1.3 Mean streamwise velocity and turbulent kinetic energy (tke) profiles at 30h for outer and inner scaling respectively (Naqavi et al., 2018).

To expand the knowledge of the flow physics, Naqavi et al. (2018) conducted a DNS of a classical wall-jet with the highest known Reynolds number ( $R_e = 7500$ ) to date. This study provides fully balanced, explicitly calculated budgets for the turbulence kinetic energy, mean flow statistics, and Reynolds normal and shear stress profiles. In addition, the study analyzed layer interaction by means of turbulent diffusion and concluded that energy in the outer region transfers to the spanwise direction in the inner region (Naqavi et al., 2018). Since previous experimental and computational studies have provided an understanding of the flow physics, it is as well important to study the manipulation of the turbulence of a wall-jet to obtain engineering benefits.

According to Schober and Fernholz (2000), large scale coherent structures play a key role in the transverse momentum transport of turbulent shear flows and mixing layers.

Hence modifying the global characteristics of a wall-jet can ultimately provide drag increase or reduction as well as enhance mixing. Previous experimental studies have analyzed the manipulation of turbulent structures by the excitation of the shear-layer instability or its subharmonics. Katz et al. (1992) and Zhou et al. (1996) investigated the influence of acoustic excitation on the coherent structures of a plane wall-jet. In 1996, Zhou et al. (1996) concluded that the momentum exchange between the wall-jet and the entrainment is depended on large-scale structures, which coherence is increased due to the forcing at the inlet. Katz et al. (1992) achieved a reduction of the skin friction of up to 30%, but only when the acoustic excitation amplitude equals 20% of the wall-jet inlet velocity.

Based on these studies, Schober and Fernholz (2000) analyzed the turbulence control in a wall-jet by the means of an oscillating wire at the inlet nozzle. As a result of introducing a perturbation in the initial shear layer, turbulence structures are significantly modified. Schober and Fernholz (2000) draws an interesting criterion for inlet perturbation, proposing that low oscillation frequencies lead to the formation of large vortices, which increase in size over several stages of vortex pairing causing skin friction reduction. Tsai et al. (2007) performed Reynolds Average Navier-Stokes Simulations (RANS) to analyze the effect of external turbulence produced by a mixing box. Their results concluded that external velocity perturbations cause a significant influence on the growth of the jet. Increasing the mean thickness of the jet resulted in a slight decrease in the skin friction. The velocity fluctuations also increase in the mixing layer and interact with the flow in the inner layer. This interaction will consequently caused an amplification of the turbulence

kinetic energy in the inner region. Bursting in the mixing layer appears to be stimulated by the external turbulence, which transports energy to the wall region (Tsai et al., 2007).

Targeting large scale motions and scale interaction, 2019 studied a classical wall-jet. The study observed that the large-scales of the flow amplitude modulate the finer scales, which ultimately resulted in skin friction reduction. Their study concluded that it exists transport of turbulent kinetic energy from the regions of peak production to the in-between region (Gnanamanickam et al., 2019). Bhatt (2019) used the same experimental facility as Gnanamanickam et al. (2019) and forced the wall-jet by the mean of a pulse at different frequencies (driven by a speaker). The perturbation at the inlet modify the turbulence behavior of the flow, and a reduction of skin friction and an increase in turbulent intensity is observed for all studied frequencies. Introducing perturbations modifies the transport of the energetic large-scales between the inner and outer region which resulted in the transport of momentum from the inner region to the outer region. The effects on inner-outer layer interaction contribute to skin friction reduction. The major contribution to skin-friction reduction is observed at 12 Hz (Bhatt, 2019).

Base on previous work, the study in this thesis will focus on a planar wall-jet which is exposed to inlet perturbations by the means of a sine wave. Since previous studies of the forced turbulent planar wall-jet showed that manipulating the outer shear layer strongly influences the near-wall region, the objective is to characterize the scale interaction and the effects of the pulsing inlet over mixing and skin friction in a wall-jet. The periodic forcing of the jet intensity can be characterized as active flow control and in engineering can be identified as a blowing-suction technique. For a wall-jet, the kinetic-energy balance



in a modulated flow enables one to assess in principle the interaction occurring between coherent motions and the incoherent turbulence.

#### **1.4 Scope and Outline**

In order to study all turbulence length scales present on a wall-jet configuration, direct numerical simulations (DNS) are performed. The scope of this work entails the study of flow physics with emphasis on turbulence analysis and particular interest on the scale interaction. A classical wall-jet and a forced wall-jet will be compared to study the effects of inlet jet perturbation on turbulent structures.

This manuscript is organized as follows. A comprehensive introduction including motivation and background was given in Chapter 1. Turbulent quantities and statistical analysis methods are presented in chapter 2. Chapter 3 presents The numerical approach use through out each case. Chapter 4 presents simulations of a two-dimensional compressible wall-jet. It entails governing equations, numerical method, flow configuration, results, and conclusions. Chapter 5 focuses on a three-dimensional incompressible wall-jet. Chapters 4 and 5 results will present the instantaneous snapshots of the flow field, turbulent statistics, and flow visualization of turbulent structures (for the three- dimensional case). Each case will also analyze the influence of the jet pulsing over mixing and skin friction. Conclusions for each case will be presented at the end of Chapter 4 and 5. Summary and Future Work are drawn in Chapter 6.

## **2. Analysis Tools for Wall-Bounded Turbulent Flows**

Most flow phenomena in our everyday surroundings, whether it is the air over a plane or the fuel inside a car engine, involve turbulence. Modern technology encounters the need to predict quantitatively the behavior of turbulent flows. These types of flows are characterized as complex and are not trivial to understand because of the wide ranges of length and velocity scales. For this study, wall-bounded turbulent flows are of particular interest as they are commonly found in diverse fields such as biology, geology, etc., but most interesting for engineering technologies associated with drag, acoustics or heat transfer. Wall turbulence encompasses the richest spectrum of scales from the small scales influencing the stress and the energy close to the wall to the large scales at the edge of the flows. It is important to notice that the range of scales increases as the Reynolds number increases, as well as, the interaction between scales.

### **2.1 Statistical Description of Turbulent Flows**

Turbulent flows are characterized by the presence of random and chaotic processes and the diversity of turbulence structures, and their behavior has been widely studied over the years. Even though different techniques have been applied, to this day there is not an exact description of the phenomena of turbulence as it is highly influenced by multiple factors including geometry, initial conditions, and boundary conditions. However, a few fundamental characteristics can be defined to describe a turbulent flow process. The following characteristics are highly dependent of the environment in which the flow develops Tennekes et al. (1972).

- Irregularity: refers to the random processes which do not allow an inherent solution for the phenomena; hence, turbulent flows require statistical analysis. Due to the non-linearity and randomness of turbulence, it is extremely challenging to understand turbulence in its entirety.
- Diffusivity: the characteristic responsible to enhance mixing and increase turbulent transport of mass, momentum, and energy Tennekes et al. (1972). For engineering application, this characteristic is essential as it is involved with flow separation, heat transfer and momentum transport.
- Large Reynolds numbers: turbulence regime is defined at higher Reynolds number, where the flows become unstable and the presence of instabilities is notable due to the interaction of viscous and non-inertial terms.
- Three-dimensional vorticity fluctuations: Turbulent flows are characterized by a strong three-dimensional vortex generation mechanism generated by high levels of fluctuating parameters. Turbulent flows are characterized by rotationality.
- Dissipation: is the process where the turbulent kinetic energy is transformed into internal energy by viscous shear stresses. Turbulence is always dissipative and requires a continuous energy supply or else the flow decay.
- Wide range of length and time scales: as turbulence entails small scales characteristics to near the wall-behavior to large scale motions observe at free flows.

Turbulent scales have been defined to characterized the eddies in turbulent flows. These scales guide computational simulators to determine the size of the cells on a grid, the

refinement needed and the time step for the simulations. Smallest eddies are governed by two important parameters, kinematic viscosity, and turbulent kinetic energy dissipation as a function of time. Equation 2.1 is known as Kolmogorov length scale and Equation 2.2 is the time scale for the smallest eddies (Pope, 2001).

$$\eta_k = \left( \frac{\nu^3}{\varepsilon} \right)^{1/4} \quad (2.1)$$

$$\tau_k = \left( \frac{\nu}{\varepsilon} \right)^{1/2} \quad (2.2)$$

As discussed in the characteristics of turbulence, the study of turbulent flows heavily relies on statistical and probabilistic analysis due to the presence of random variables. Since velocity, pressure and density are characterized as random variables in a turbulent flow, their value is inherently unpredictable. The use of probability density functions (PDF) is required to help characterize the flow development. A PDF will provide the probability per unit distance in the sample space of a variable. Other important tools that are used for statistical analysis include ensemble average, different order of moments and flow visualization (Pope, 2001). The following sections will briefly discuss the definition of the tools being used for the analysis of the flow subject of this study.

### 2.1.1 Mean Flow Properties

Using Reynolds decomposition, a turbulent parameter,  $u_i$  can be decomposed into the mean,  $U_i$ , and fluctuation,  $u_i'$  components as shown in Figure 2.1 and Equation 2.3 (Pope, 2001).

$$u' = u - U \quad (2.3)$$

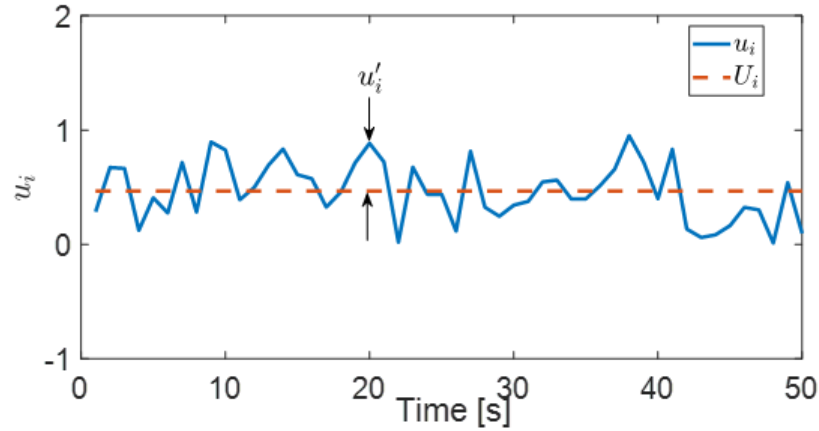


Figure 2.1 Reynolds Decomposition of  $u_i$ .

The ensemble average, shown in Equation 2.4, is used to obtain the arithmetic mean of the turbulent parameters. The use of ensemble average is based on the assumption of independent statistical events, even though the definition requires an infinite number of events it provides a good approximation for the mean.

$$\langle u_i \rangle = \lim_{N \rightarrow \infty} \frac{1}{N} \sum_{n=1}^N (u_i)_n \quad (2.4)$$

From the ensemble average of velocity, density and pressure, fluid mechanics defined flow parameters that help describe the turbulent phenomena. Among these parameters are the wall shear stress, mean velocity profiles, friction coefficient, velocity decay, Reynolds numbers, etc (Pope, 2001).

### 2.1.2 Turbulent Statistics and Kinetic Energy

For the analysis of the fluctuating component of the turbulent parameters, Probability Density Functions (PDFs) and corresponding moments are defined. These functions will

provide a complete description of the turbulent parameter at a given space and time.

Mathematically a PDF is written as Equation 2.5. The PDF is constructed using all values of the turbulent variable at a fixed location on the sample space at different times.

$$\langle u_i^n \rangle = \int_{-\infty}^{\infty} u_i^n P(u_i) du_i \quad (2.5)$$

where  $P(u_i)$  is the probability density function of the random variable  $u_i$ . Moments of the turbulent variable are defined using the PDF, and depending on the order will provide different aspects that will help characterize the flow. The first moment is the mean of the flow  $U$  or  $\langle u_i \rangle$ . The second moment is known as variance, shown in Equation 2.6,. It is defined as the mean-square fluctuation of the assigned property (Pope, 2001).

$$\langle u_i'^2 \rangle = \int_{-\infty}^{\infty} (u_i - U_i)^2 P(u_i) du_i \quad (2.6)$$

Taking the square root of the variance one can express the standard deviation of the property as shown in Equation 2.7. In the analysis of turbulent flows, this value is also known as the root mean square of the assigned property (Pope, 2001). Variance is used to study the turbulence intensity in different directions, this analysis allows us to visualize the peaks of fluctuations in each region of the flow.

$$\sigma_{u_i} = \sqrt{\text{var}(u_i)} = \langle u_i'^2 \rangle^{\frac{1}{2}} \quad (2.7)$$

When working with random variables, such as  $\hat{U}_i$ , it is more convenient to analyze the flow properties using standardization. The standardization of a random variable is shown in Equation 2.8, while the standardization of the moment is shown in Equation 2.9

$$\hat{U}_i = \frac{(u'_i - U_i)}{\sigma_{u_i}} \quad (2.8)$$

$$\hat{u}_i = \frac{\langle u_i^n \rangle}{\sigma_{u_i}^n} \quad (2.9)$$

where  $\sigma_{u_i}$  is the standard deviation of the property. Two standardizations over the velocity are used for this study. The first one is the skewness, which is the third moment of the velocity normalized by its variance as shown in Equation 2.10. This function reveals the information about the asymmetry of the velocity PDF. If the velocity PDF is symmetric about the mean, it has zero skewness. Positive skewness indicates that the PDF has a longer tail. Hence a positive skewness reveals that the fluctuation velocity is more likely to take positive values than negative values (Pope, 2001).

$$\frac{\langle u_j^3 \rangle}{(\langle u_j^2 \rangle)^{\frac{3}{2}}} \quad (2.10)$$

To study the mean kinetic energy associated with turbulent flow, turbulent kinetic energy (tke) is calculated. The turbulent kinetic energy of the flow is defined using the fluctuation component of the velocity in all directions, as shown in Equation 2.11

$$\kappa = \frac{1}{2} \left( \langle \overline{u'^2} \rangle + \langle \overline{v'^2} \rangle + \langle \overline{w'^2} \rangle \right) \quad (2.11)$$

The transport equation of the Reynolds-stress tensor can be written as Equation 2.12.

$$\frac{\partial}{\partial t} \overline{u_i u_j} = P_{ij} + \varepsilon_{ij} + D_{ij} + T_{ij} - \Pi_{ij}^s + \Pi_{ij}^t - C_{ij} \quad (2.12)$$

where  $P_{ij}$  is the production tensor

$$P_{ij} = -\overline{u_i u_k} \frac{\partial U_j}{\partial x_k} - \overline{u_j u_k} \frac{\partial U_i}{\partial x_k} \quad (2.13)$$

$\varepsilon_{ij}$  is the dissipation tensor

$$\varepsilon_{ij} = -2\nu \overline{\frac{\partial u_i}{\partial x_k} \frac{\partial u_j}{\partial x_k}} \quad (2.14)$$

$\Pi_{ij}^t$  is the pressure transport

$$\Pi_{ij}^t = -\frac{1}{\rho} \left( \frac{\partial}{\partial x_j} \overline{p u_i} + \frac{\partial}{\partial x_i} \overline{p u_j} \right) \quad (2.15)$$

$\Pi_{ij}^s$  is the pressure strain

$$\Pi_{ij}^s = -\frac{1}{\rho} \left( \overline{p \frac{\partial u_i}{\partial x_j}} + \overline{p \frac{\partial u_j}{\partial x_i}} \right) \quad (2.16)$$

$D_{ij}$  is the viscous diffusion

$$D_{ij} = \nu \frac{\partial^2}{\partial x_k^2} \overline{u_i u_j} \quad (2.17)$$

$T_{ij}$  is the turbulent transport

$$T_{ij} = -\frac{\partial}{\partial x_k} \overline{u_i u_j u_k} \quad (2.18)$$

$C_{ij}$  is the convection

$$C_{ij} = U_k \frac{\partial}{\partial x_k} \overline{u_i u_j} \quad (2.19)$$



and  $\rho$ ,  $\nu$ ,  $p$  are defined as the density, kinematic viscosity and pressure of the fluid respectively. For a planar wall-jet, the Reynolds stress balances will visually look like a combination of boundary layer and free-shear layer due to the inner and outer regions characteristic of the flow. According to Dejoan and Leschziner (2005), these budgets provide information related to the behavior of second moments of the flow and they are sought to understand the role that the interaction between layers plays on the development of turbulence on a wall-jet. The budget data has particular importance for wall-bounded flows as the influence of Reynolds stresses become strong near the wall. Mansouri observed in his study that the pressure-gain term near the wall is not of the same order as the production term away from the wall (Mansour et al., 1988). The importance is given in this study to the production terms which are more predominant near-the wall and can offer insight into the interaction between regions.

### **2.1.3 Scaling Parameters**

To characterize the wall turbulence two types of scales are defined: intrinsic and extrinsic. Extrinsic scales are assigned as desired by the experimentalist or computational simulation. For instance initial and boundary conditions, fluid properties, and external forces. Intrinsic scales result from the flow response subject to the extrinsic scales, some examples include boundary layer thickness or maximum velocity decay. It remains uncertain what is the appropriate scale for a meaningful description of the turbulent phenomena. As many studies have shown, scaling is used to determine the predictability over a certain flow. As described in the introduction, for wall-jets, many different scaling

lengths have been proposed, yet no common scaling parameter has been found to scale correctly both mean velocity and higher-order moment statistics (Davidson et al., 2012).

For a wall-jet configuration, the scaling laws depend on the region of the analysis. Commonly, the flow is analyzed by inner and outer scaling which have varied over multiple studies. To better understand the inner and outer separation, one takes the classical description of a flow which is divided into 4 layers:

1. Viscous sublayer:  $y^+ < 5$ ;  $U^+ = y^+$
2. Buffer layer:  $5 < y^+ < 30$ ;  $U^+ = f_1(y^+)$
3. Log layer:  $30 < y^+ < 0.15Re_\tau$ ;  $U^+ = \frac{1}{k} \ln y^+ + A$
4. Wake layer:  $y^+ > 0.15Re_\tau$ ;  $(U_\infty - U)^+ = f_2(\frac{y}{\delta})$

where  $y^+$  represent wall units defined in Equation 2.21 and  $k$  and  $A$  are constants that depend on the flow type. The inner scaling converges over the viscous, and the buffer layer. The outer scaling tends to agree on the wake layer. The logarithmic layer for a wall-jet is a section of overlap between inner and outer region where scaling have been dependent of the layout of the flow. Some of the parameters that have been explore for inner scaling include friction velocity, shown in Equation 2.20 and kinematic viscosity. Generally the inner region is scaled using wall units which are defined in Equation 2.21. Other scaling have been suggested including  $(y_{1/2})_{in}$  and it is taken into account to determine the convergence and predictability of the flow (Pope, 2001).

$$u_\tau = \sqrt{\frac{\tau_w}{\rho}} \quad (2.20)$$

$$y^+ = \frac{yu_\tau}{\nu} \quad (2.21)$$

For the outer region, it exists a dependence in whether the flow is developed in a still environment or in a moving fluid stream. Based on the presence or absence of an external stream, the proposed scaling will be the maximum stream-wise velocity,  $U_m$  or a combination of the stream-wise velocity and the velocity of the co-flow ( $U_m - U_c$ ) (Naqavi et al., 2014). The correspondent normal length scales that have been proposed include the slot inlet height and  $y_{1/2}$ . For this work, the laws applied by Naqavi et al. (2018), are mainly considered for results comparison.

## 2.2 Turbulent Structures

To describe the complex multi-scale and chaotic motions associated with turbulent flows, researchers have been able to describe elementary flow features known as turbulent structures or coherent structures. In these structures, vorticity is usually stochastic containing orderly elements. These elements are instantaneously coherent over the spatial extent of the turbulent flow structure. In other words, coherent structures are organized components of the vorticity which is phase-correlated over the entire space of the structure (Hussain, 1986). Coherent structures are characterized by high levels of coherent vorticity, production, Reynolds stress, and mass and heat transport.

The large-scale transport of mass, heat, and momentum without requiring high amounts of energy is done by these structures. Researchers have been able to identify these structures by flow visualization, conditional sampling techniques or statistical analysis

over the velocity fluctuations (Pope, 2001). Coherent structures are typically formed from instabilities in the flow. The initial or boundary conditions of a flow can trigger instabilities in which their growth is determined by evolutionary changes due to non-linear interactions with other coherent structures, or their decay onto incoherent turbulent structures (Hussain, 1986). The instability that drives this flow configuration is known as Kelvin Helmholtz instability. and will be explained more in detail in the following section. The evolution of the initial instability is shown in Figure 2.2, where different turbulent structures are illustrated, such as roll structure, ejections, as well as behavior near the wall.

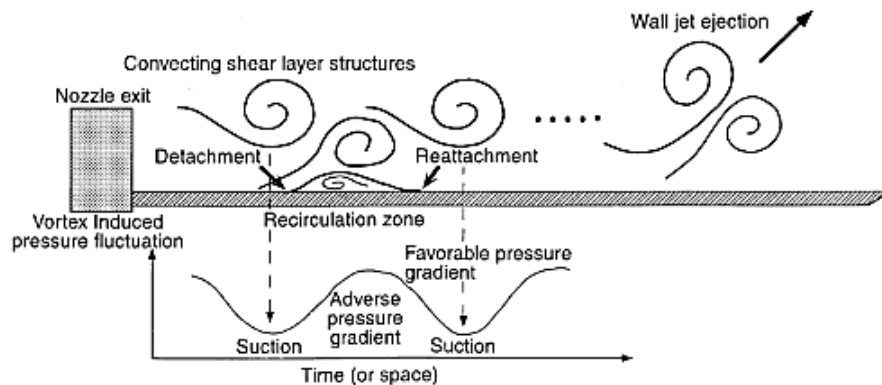


Figure 2.2 Kelvin-Helmholtz Instability Evolution described by Gogineni and Shih (1997).

For wall-bounded flows, Robinson (1991) characterized the coherent structures in eight categories:

1. *Low-speed streaks in the region  $0 < y^+ < 10$ .* At the near the wall region, these structures correspond to the relatively slow-moving fluid (stream-wise velocity equivalent of approximate half of the local mean). The fluid between the streak structures is known to be of fast motion Pope (2001). The streaky structure has been associated with quasi-streamwise vortices near the wall. These vortices are

counter-rotating vortex filaments on either side of the low speed streak Davidson et al. (2012).

2. *Ejections of low-speed fluid outward from the wall.* When the migration of a streak away from the wall is suddenly faster, the process is known as streak lifting or ejection. Ejections are fundamental for production of turbulent energy. In Figure 2.3, the  $u'v'$  space or the velocity fluctuation space is illustrated as four quadrants which are used to statistically define ejections as the points where the stream-wise fluctuation are negative and the normal fluctuations are positive. These points are known to be in the second quadrant,  $Q_2$  (Pope, 2001).

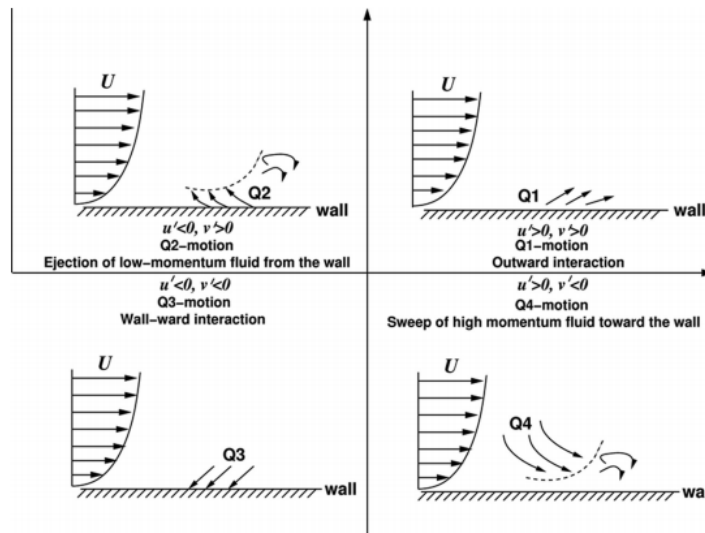


Figure 2.3 Schematic diagram showing different turbulent fluid motions according to quadrant analysis procedure (Saha et al., 2017).

3. *Sweeps of high-speed fluid toward the wall.* The movement of fluid away from the wall cause a counter action of high speed fluid toward the wall referred as sweeps. Sweeps like ejections are important produce turbulent energy. In Figure 2.3, the  $u'v'$

space representing sweeps is the fourth quadrant,  $Q_4$ , where the stream-wise fluctuations are positive and the normal fluctuations are negative Pope (2001).

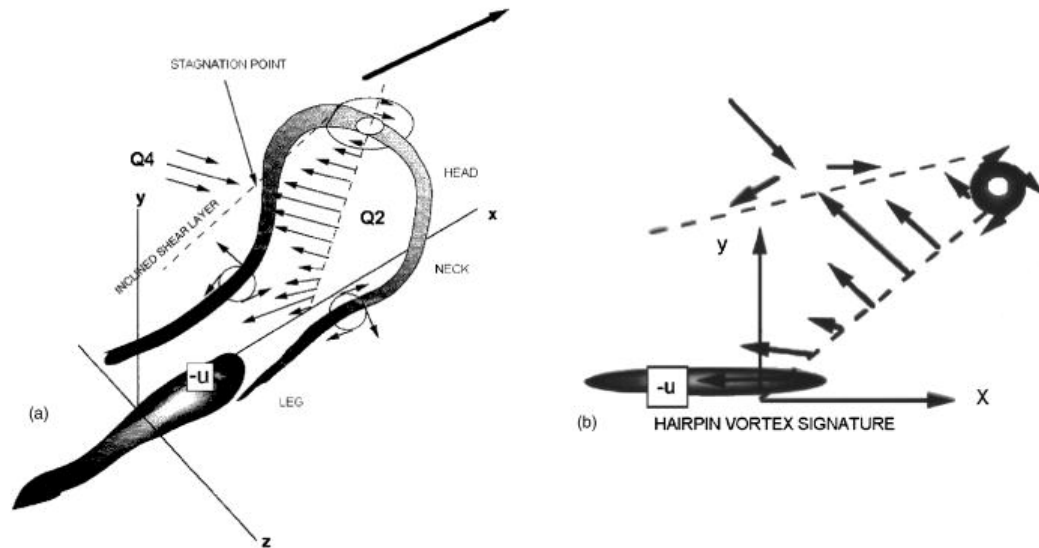


Figure 2.4 (a) Schematic of a hairpin eddy attached to the wall; (b) signature of the hairpin eddy in the streamwise-wall-normal plane (Adrian et al., 2000).

#### 4. Vortical structures of several proposed forms. In the vicinity of the wall

( $y^+ < 100$ ), pairs of counter-rotating stream-wise vortices also known as rolls have predominance over other vortical structures. The fluid between the pair of rolls has reduced axial velocity and contribute to the velocity profiles. Away from the wall the dominant vortical structure is known as horseshoe or hairpins vortices. Hairpins are characterized by a head as shown in Figure 2.4, which is a region of compact vorticity, followed by a small neck structure and two legs. The head and the neck are located in plane where  $Q_2$  orientation is almost perpendicular to it. The legs are in located in the low-speed streak near the wall (Adrian, 2007). Hairpins are suggested as a fundamental structure to describe the transport mechanisms in wall turbulence, hence it has been used by several researchers to model turbulence near

the wall (Davidson et al., 2012). Larger structures have been suggested to be formed by an ensemble of hairpin vortices (Pope, 2001). Quasi-streamwise vortices, hairpin vortices, and packets of hairpins are commonly found coherent structures in wall-bounded turbulence and they are identified by their long persistence

5. *Strong internal shear layers in the wall zone ( $y^+ > 180$ )*. Shear layers occur when two parallel streams of fluids meet at an interface with a velocity difference or between the moving flow and a motionless surface. Instabilities like Kelvin-Helmholtz instabilities (KHI) are resultant of shear layer on the flow.
6. *Near-wall pockets*, observed as areas clear of marked fluid in certain types of flow visualizations.
7. *Backs*: surfaces (of scale  $\delta$ ) across which the streamwise velocity changes abruptly.
8. *Large-scale motions in the outer layers (including, for boundary layers, bulges, superlayers, and deep valleys of free-stream fluid)*. Valleys are non-turbulent fluid that travels deeply into the boundary layer structure. They are commonly found between two bulges, which are large inclined eddies. The inclination is normally between 20 to 25 degrees. They slowly evolve as they travel downstream of the domain and they can be scaled with conventional outer scaling.

To visualize these turbulent structures, the curl of the velocity or vorticity is being used to identify vortices, specially at the inlet of the jet. One of the disadvantages of this method is that swirling motions and shearing motions cannot be separated, therefore another method is used to visualize more complex structures. The Q-criterion method is based on the velocity gradient tensor,  $D_{ij} = \frac{\partial u_i}{\partial x_j}$ . The second order tensor can be

decomposed into symmetric and a skew-symmetric part such that  $D_{ij} = S_{ij} + \Omega_{ij}$ , where  $S_{ij} = \frac{1}{2} \left( \frac{\partial u_i}{\partial x_j} + \frac{\partial u_j}{\partial x_i} \right)$  is the rate-of-strain tensor and  $\Omega_{ij} = \frac{1}{2} \left( \frac{\partial u_i}{\partial x_j} - \frac{\partial u_j}{\partial x_i} \right)$  is the vorticity tensor. In Q-criterion, a vortex is considered to be a connected fluid region with a positive second invariant of the velocity gradient tensor. Q represents the vortical areas where the vorticity magnitude is greater than the magnitude of the rate-of strain.

The iso-surfaces obtained by this method are good indicators of turbulent flow structures (Holmén, 2012). For instance, Figure 2.5 illustrates the iso-surfaces obtained for the outer layer of a wall-jet, where one can observe the billows or vortical structures generated by the Kelvin-Helmholtz instability that grow as they are convected downstream. In the downstream domain, various large scale vortical structures are pictures in the outer layer of the wall-jet. Other techniques to visualize turbulent structures include  $\Delta$ -criterion,  $\lambda_a$ -criterion, swirling strength criterion and triple decomposition, Q-criterion is chosen for this study since there exist results for comparison.

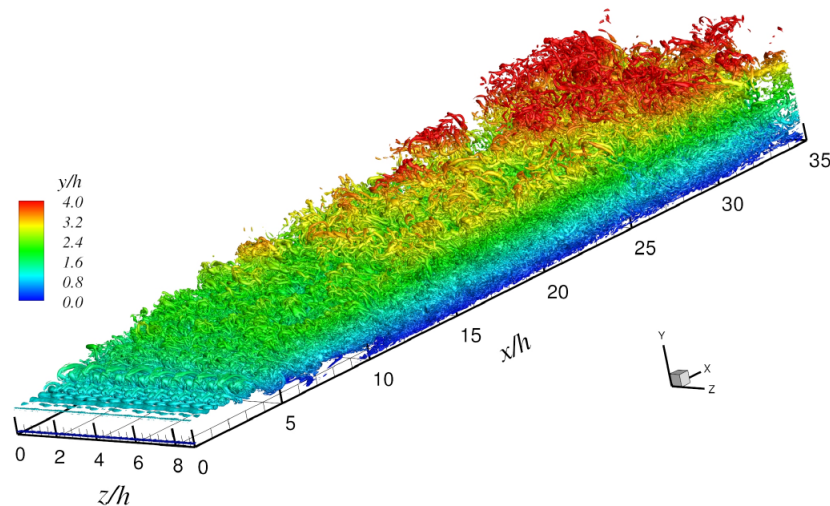


*Figure 2.5* Iso-surfaces of the second invariant of the velocity gradient tensor in the wall jet (Naqavi et al., 2017).



### 2.3 Kelvin-Helmholtz Instability

As mentioned before the outer layer resembles a free shear flow which is subjected to Kelvin Helmholtz instability (KHI). KHI happens in a single continuous fluid when one region of fluid has a higher velocity than the other, the interaction between the different velocities forms a shear layer, which can break down into a wavy pattern formed by eddies. KHI is characterized by the frequency of formation of individual eddies and the growth of wavelike disturbances to induce turbulence and mixing. The process of transition from laminar to turbulent flow involves the breaking of internal waves which allows a turbulent diapycnal mixing. In variable density flows, Kelvin-Helmholtz Instabilities is a shear driven instability caused by the juxtaposition of two layers at different velocities, different densities or both conditions. At the contact surface, the two layers will create shear that will develop roll structures known as billows. Affecting the billow production will modify the turbulent structures at the downstream domain.

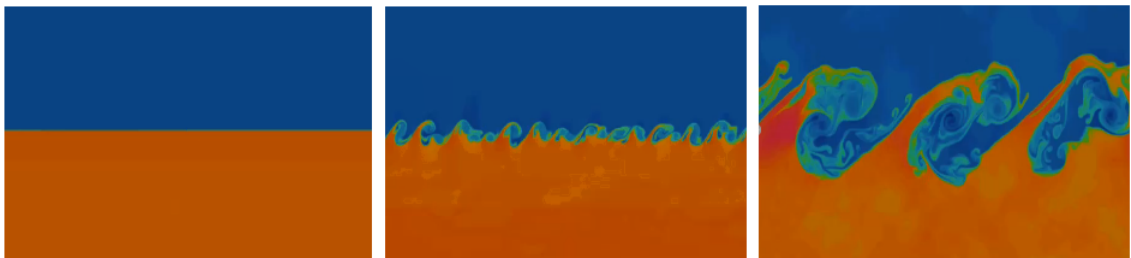


*Figure 2.6 Kelvin-Helmholtz Instability Evolution.*

The perturbed turbulent structures will affect the skin friction and mixing of an unforced wall-jet. In this thesis we observe KHI in a single continuous fluid at different velocities.

## 2.4 DNS Approach

Direct Numerical Simulation approach consists of numerically solving Navier-Stokes equations without a turbulence model. This approach solves all the scales of motion of turbulence by using initial and boundary conditions to predict the desired flow, providing a high-fidelity solution of turbulent flows. Due to the accuracy of the method and the constant improvement in high-performance computing techniques, this method is gaining importance in the turbulence field according to Moin and Mahesh (1998). A planar wall-jet is a complex flow configuration which displays a wide range of turbulence scales from transition close to the nozzle entry to high Reynolds number turbulence in the fully developed regime; therefore, the flow demands a highly accurate (in space and time) computational method like Direct Numerical Simulation (DNS). The equations governing this approach are Navier-Stokes equations of continuity, momentum and energy presented in Equation 2.22, 2.23 and 2.24. For the different descriptions of flows, such as dimensionality or compressibility, appropriate assumptions are taken to simplify this set of equations.

Continuity equation:

$$\frac{\partial \rho}{\partial t} + \frac{\partial \rho u_i}{\partial x_j} = 0 \quad (2.22)$$

Momentum equation:

$$\frac{\partial \rho u_i}{\partial t} + \frac{\partial \rho u_i u_j}{\partial x_j} = -\frac{\partial p}{\partial x_i} + \frac{\partial \tau_{ij}}{\partial x_j} \quad (2.23)$$

Energy equation:

$$\frac{\partial \rho E}{\partial t} + \frac{\partial \rho E u_j}{\partial x_j} = -\frac{\partial q_j}{\partial x_j} + \frac{[u_i(\tau_{ij} - P\delta_{ij})]}{\partial x_j} \quad (2.24)$$

where,

$$\tau_{ij} = \mu \left( \frac{\partial u_i}{\partial x_j} + \frac{\partial u_j}{\partial x_i} \right) - \frac{2}{3} \mu \frac{\partial u_k}{\partial x_k} \delta_{ij} \quad (2.25)$$

When using DNS, numerical methods are required to accurately compute the flow quantities its evolution over a wide range of length and time scales. For this study two numerical methods are described, Discontinuous Galerkin methods (DG) and Spectral Element Method (SEM), for the compressible and the incompressible case respectively. For this study, the emphasis is placed on the specification of inflow and outflow boundaries for each case studied. The following sections will provide a detailed description of each numerical method used, as well as, the computational set-up for each case.

### 3. Numerical Method

When numerically solving the Navier-Stokes equations, it is customary to discretize space and time independently. A variety of spatial discretizations exist, among the most common are finite difference (FD) method, finite volume (FV) method and finite element (FE) which have been widely used in academia and industry to successfully solve fluid flow problems. An important consideration when choosing the appropriate discretization is accuracy. The methods, previously mentioned, provide first or second order of accuracy in space, causing a large degree of numerical dissipation. Numerical dissipation is not suitable to simulate fundamentally unsteady phenomena.

In the need of better simulation tools, attention has recently shifted towards high-order methods. Theoretical studies and numerical experiments suggest that high-order methods for unstructured grids can solve hitherto intractable fluid flow problems in the vicinity of complex geometrical configurations. These methods tend to increase accuracy order while reducing computational cost (Witherden et al., 2016). In the present work, two examples of high order methods are utilized. The first one is the flux reconstruction (FR) approach implemented by the PyFR framework. The second one is spectral element methods (SEM) implemented by the Nek5000 framework. The following sections provide a detail description of each framework which includes spatial and time discretization, as well as, additional functions implemented in each framework to perform this study.

#### 3.1 PyFR

An open source Python based computational fluid dynamics framework designed for advection diffusion problems, using the flux reconstruction approach by Huynh (2007). PyFR is designed to solve a range of governing systems (from Euler to Navier-Stokes

equations) in mixed unstructured grids with different element types (Witherden et al., 2014). In addition, it is designed to target a range of hardware platforms via use of an in-built domain specific language based on the Mako templating engine. In the present study, this framework is used to perform simulations of a two-dimensional compressible wall-jet in a single GPU Workstation. Table 3.1 summarize the capabilities of the framework (Witherden et al., 2014).

*Table 3.1*

*PyFR Capabilities*

Dimensions	2D,3D
Elements	Triangles, Quatrilaterals, Hexahedra
Spatial orders	User defined
Time steppers	RK methods, DOPRI5
Precisions	Single, Double
Platforms	CPUs via C/OpenMP, Nvidia GPUs via CUDA
Parrallel Computing	MPI
Governing Equations	Euler, Navier-Stokes

### 3.1.1 Spatial Discretization

The flux reconstruction approach is a high order method that brings together under integrated collocation-based nodal Discontinuous Galerkin (DG) schemes and spectral difference (SD) scheme. An overview of FR approach applied to solving advection-diffusion problems. Inside an arbitrary domain  $\Omega$  in  $N_D$  dimension, consider the following advection diffusion problem:

$$\frac{\partial u_\alpha}{\partial t} + \nabla \cdot \mathbf{f}_\alpha = 0 \quad (3.1)$$

where  $u_\alpha = u_\alpha(\mathbf{x}, t)$  is a conserved quantity,  $\alpha$  is the field variable index ranging from 0 to  $N_V$ ,  $\mathbf{f}_\alpha = \mathbf{f}_\alpha(u, \nabla u)$  is the flux of the conserved quantity, and  $\mathbf{x} = x_i \in \mathbb{R}^{N_D}$ . Notice  $u$  is in its unscripted form to represent all  $N_V$  field variables and  $\nabla u$  consists on the gradient of each field variable. To start the spatial discretization, the desired equation (equation 3.1) is expressed as a first order system.

$$\frac{\partial u_\alpha}{\partial t} + \nabla \cdot \mathbf{f}_\alpha(u, \mathbf{q}) = 0 \quad (3.2a)$$

$$\mathbf{q}_\alpha - \nabla u_\alpha = 0 \quad (3.2b)$$

Where  $\mathbf{q}$  is an auxiliary variable, which represents the gradients of all field variables. Proceed by dividing the domain up into elements,  $e$ , of any length.  $\mathcal{E}$  represents the set of available element types in  $\mathbb{R}^{N_D}$ , in NEK5000 triangles, quadrilaterals, hexahedral, prisms, pyramids, and tetrahedral elements are used depending on the dimensionality. These elements are then used to construct a conformal mesh as shown below:

$$\Omega = \bigcup_{e \in \mathcal{E}} \Omega_e \quad \text{and} \quad \Omega_e = \bigcup_{n=0}^{|\Omega_e|-1} \Omega_{en} \quad \text{and} \quad \bigcap_{e \in \mathcal{E}} \bigcap_{n=0}^{|\Omega_e|-1} \Omega_{en} = \emptyset$$

where  $\Omega_e$  refers to the element type,  $e$ , inside the domain,  $|\Omega_e|$  is the number of elements of each type in the decomposition, and  $n$  is the index running over these elements. Inside each element,  $\Omega_e$ , the following should comply

$$\frac{\partial u_{en\alpha}}{\partial t} + \nabla \cdot \mathbf{f}_{en\alpha} = 0 \quad (3.3a)$$

$$\mathbf{q}_{en\alpha} - \nabla u_{en\alpha} = 0 \quad (3.3b)$$

To facilitate implementation a transformed space is defined. For each element, a mapping function is assumed such that  $\tilde{\mathbf{x}} = \tilde{x}_i$ , where for each element type a standard

element  $\hat{\Omega}_e$  is defined. The following expressions represent the mapping function for each element

$$\begin{aligned} x_i &= \mathcal{M}_{eni}(\tilde{x}) & x_i &= \mathcal{M}_{en}(\tilde{x}) \\ \tilde{x}_i &= \mathcal{M}_{eni}^{-1}(x) & \tilde{x}_i &= \mathcal{M}_{en}^{-1}(x) \end{aligned}$$

along with the correspondent Jacobian matrices,

$$\begin{aligned} \mathbf{J}_{en} &= J_{eni_j} = \frac{\partial \mathcal{M}_{eni}}{\partial \tilde{x}_j} & J_{en} &= \det \mathbf{J}_{en} \\ \mathbf{J}_{en}^{-1} &= J_{eni_j}^{-1} = \frac{\partial \mathcal{M}_{eni}^{-1}}{\partial \tilde{x}_j} & J_{en}^{-1} &= \det \mathbf{J}_{en}^{-1} = \frac{1}{J_{en}} \end{aligned}$$

Using these expressions, the governing equations can be transformed from the physical domain to the computational domain. Notice that,

$$\frac{\partial u_{en\alpha}}{\partial t} + J_{en}^{-1} \tilde{\nabla} \cdot \tilde{\mathbf{f}}_{en\alpha} = 0 \quad (3.4a)$$

$$\tilde{\mathbf{q}}_{en\alpha} - \tilde{\nabla} u_{en\alpha} = 0 \quad (3.4b)$$

where  $\tilde{\nabla} = \frac{\partial}{\partial \tilde{x}_i}$  and  $\tilde{u}_{en\alpha}$ ,  $\tilde{\mathbf{f}}_{en\alpha}$ , and  $\tilde{\mathbf{q}}_{en\alpha}$  are the transformed solution, flux, and gradients respectively, inside each element  $\Omega_e$ .

$$\tilde{u}_{en\alpha} = u_{en\alpha}(\tilde{x}, t) = J_{en}(\tilde{\mathbf{x}}) u_{en\alpha}(\mathcal{M}_{en}(\tilde{\mathbf{x}}), t) \quad (3.5a)$$

$$\tilde{\mathbf{f}}_{en\alpha} = \mathbf{f}_{en\alpha}(\tilde{x}, t) = J_{en}(\tilde{\mathbf{x}}) J_{en}^{-1}(\mathcal{M}_{en}(\tilde{\mathbf{x}})) \mathbf{f}_{en\alpha}(\mathcal{M}_{en}(\tilde{\mathbf{x}}), t) \quad (3.5b)$$

$$\tilde{\mathbf{q}}_{en\alpha} = \mathbf{q}_{en\alpha}(\tilde{x}, t) = J_{en}^T(\tilde{\mathbf{x}}) \mathbf{q}_{en\alpha}(\mathcal{M}_{en}(\tilde{\mathbf{x}}), t) \quad (3.5c)$$

The approximate solution,  $u_{e\sigma n\alpha}$ , is defined within each  $e$  element type by a multidimensional polynomial of degree  $\wp$ . The set of points from the polynomial,  $\tilde{\mathbf{x}}_{e\rho}^{(u)}$  (where  $0 \leq \rho < N_e^{(u)}(\wp)$ ), are used to build a nodal basis set  $\ell_{e\rho}^{(u)}(\tilde{\mathbf{x}})$  with the property that  $\ell_{e\rho}^{(u)}(\tilde{\mathbf{x}}) = \delta_{\rho\sigma}$ . In Figure 3.3, the solution points are represented as blue dots. Along

with the solution points, a set of flux points,  $\tilde{\mathbf{x}}_{ep}^{(f)}$ , are defined on each  $\partial\Omega_e$ . In Figure 3.1, the flux points are represented as orange squares. Notice the use of the superscript ( $u$ ) for solution points and ( $f$ ) for flux points. Figure 3.1 also visually represents a set of normal flux vectors,  $\tilde{\mathbf{n}}_{ep}^{(f)}$  that are used to calculate the common normal flux.

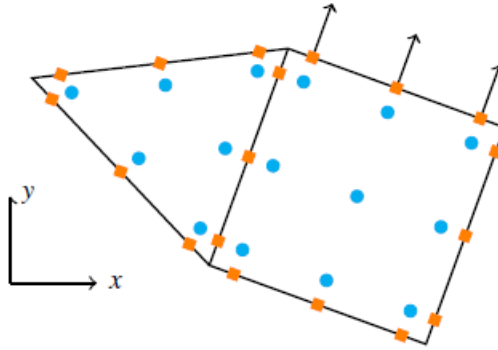


*Figure 3.1* Solution points (blue) and flux points (orange) in a triangular and quadrilateral element in physical space. The normal vectors for the quadrilateral element are represented in black (Witherden et al., 2014).

Having set the domain space for the spatial discretization method, the FR approach starts by transforming the discontinuous solution at the solution points to the discontinuous solution at the flux points.

$$u_{e\sigma n\alpha}^{(f)} = u_{epn\alpha}^{(u)} \ell_{ep}^{(u)} \tilde{\mathbf{x}}_{e\sigma}^{(f)} \quad (3.6)$$

where  $u_{e\sigma n\alpha}^{(f)}$  is an approximate solution of the field variable  $\alpha$  inside of each element at solution point  $\tilde{\mathbf{x}}_{ep}^{(u)}$ . The common solution can be computed as

$$\mathbb{C}_\alpha u_{epn\alpha}^{(f)} = \mathbb{C}_\alpha u_{epn\alpha}^{(f)} = \mathbb{C}_\alpha \left( u_{e\beta n\alpha}^{(f)}, u_{e\beta n\alpha}^{(f)} \right) \quad (3.7)$$



where  $\mathbb{C}_\alpha(u_R, u_L)$  is a scalar function that given two points returns a common value. The common solution is allowed to perform upwinding or downwinding solution, therefore it is important that each element interface yields the same common flux. Further, a vector correction function is defined as  $g_{ep}^{(f)}$ . This function is associated to with each flux point such that,

$$\hat{\mathbf{n}}_{e\sigma}^{(f)} \cdot \mathbf{g}_{ep}^{(f)}(\tilde{\mathbf{x}}_{e\sigma}^{(f)}) = \delta_{\rho\sigma} \quad (3.8)$$

The solution for the auxiliary Equation 3.4b is defined using the common solution and the vector correction

$$\tilde{\mathbf{q}}_{e\sigma n\alpha}^{(u)} = \left[ \hat{\mathbf{n}}_{ep}^{(f)} \cdot \tilde{\nabla} \cdot \mathbf{g}_{ep}^{(f)}(\tilde{\mathbf{x}}) \left\{ \mathbb{C}_\alpha u_{epn\alpha}^{(f)} - u_{epn\alpha}^{(f)} \right\} + u_{evn\alpha}^{(u)} \tilde{\nabla} \ell_{ev}^{(u)}(\tilde{\mathbf{x}}) \right]_{\tilde{\mathbf{x}}=\tilde{\mathbf{x}}_{e\sigma}^{(u)}} \quad (3.9)$$

where  $\left\{ \mathbb{C}_\alpha u_{epn\alpha}^{(f)} - u_{epn\alpha}^{(f)} \right\}$  represents the jump at the element interface and the final term is an order  $\wp - 1$  approximation of the gradient resultant from differentiating the discontinuous solution polynomial. The physical gradients can be calculated using the approaches of Kopriva (1998) and Sun et al. (2007) as shown in equations 3.10 and 3.11.

$$\mathbf{q}_{e\sigma n\alpha}^{(u)} = \mathbf{J}_{e\sigma n\alpha}^T \tilde{\mathbf{q}}_{e\sigma n\alpha}^{(u)} \quad (3.10)$$

$$\mathbf{q}_{e\sigma n\alpha}^{(f)} = \ell_{\rho}^{(u)}(\tilde{\mathbf{x}}_{e\sigma}^{(f)}) \mathbf{q}_{e\sigma n\alpha}^{(u)} \quad (3.11)$$

where  $\mathbf{J}_{e\sigma n\alpha}^{T(u)} = \mathbf{J}_{en}^{-T}(\tilde{\mathbf{x}}_{e\sigma}^{(u)})$ . Having the solution for the auxiliary equation allows us to evaluate the transformed flux

$$\tilde{\mathbf{f}}_{e\sigma n\alpha}^{(u)} = J_{epn}^{-1} \mathbf{J}_{epn}^{-1(u)} \mathbf{f}_\alpha(u_{e\sigma n}, \mathbf{q}_{e\sigma n}^{(u)}) \quad (3.12)$$

where  $\mathbf{J}_{e\sigma n}^{(u)} = \det \mathbf{J}_{en}(\tilde{\mathbf{x}}_{e\sigma}^{(u)})$ . Using Equation 3.12, the normal transformed flux is calculated at each flux points

$$\tilde{f}_{e\sigma n\alpha}^{(f_{\perp})} = \ell_{ep}^{(u)}(\tilde{\mathbf{x}}_{e\sigma}^{(f)}) \hat{\mathbf{n}}_{e\sigma}^{(f)} \cdot \tilde{\mathbf{f}}_{epn\sigma}^{(u)} \quad (3.13)$$

Considering the physical normals (represented in Figure 3.3 as arrows in the surface interface) at the flux points

$$\mathbf{n}_{e\sigma n}^{(f)} = n_{e\sigma n}^{(f)} \hat{\mathbf{n}}_{e\sigma n}^{(f)} = \mathbf{J}_{e\sigma n}^{-T(f)} \hat{\mathbf{n}}_{e\sigma}^{(f)} \quad (3.14)$$

Notice that between two elements the boundary is common, hence the normal flux has the property of  $\hat{\mathbf{n}}_{e\sigma n}^{(f)} = -\hat{\mathbf{n}}_{e\sigma n}^{(f)}$ . Then, at a flux pair a common normal flux can be specified such that

$$\tilde{\mathfrak{F}}_{\alpha} f_{e\sigma n\alpha}^{(f_{\perp})} = \tilde{\mathfrak{F}}_{\alpha} \tilde{f}_{e\sigma n\alpha}^{(f_{\perp})} = \tilde{\mathfrak{F}}_{\alpha} \left( u_{e\sigma n}^{(f)}, u_{e\sigma n}^{(f)}, \mathbf{q}_{e\sigma n}^{(f)}, \mathbf{q}_{e\sigma n}^{(f)}, \hat{\mathbf{n}}_{e\sigma n}^{(f)} \right) \quad (3.15)$$

The relationship  $\tilde{\mathfrak{F}}_{\alpha} f_{e\sigma n\alpha}^{(f_{\perp})} = \tilde{\mathfrak{F}}_{\alpha} \tilde{f}_{e\sigma n\alpha}^{(f_{\perp})}$  arises from the desire for the resulting numerical scheme to be conservative; a net outward flux from one element must be balanced by a corresponding inward flux on the adjoining element. The common normal fluxes can be transformed such that

$$\tilde{\mathfrak{F}}_{\alpha} \tilde{f}_{e\sigma n\alpha}^{(f_{\perp})} = J_{e\sigma n}^{(f)} n_{e\sigma n}^{(f)} \tilde{\mathfrak{F}}_{\alpha} f_{e\sigma n\alpha}^{(f_{\perp})} \quad (3.16)$$

$$\tilde{\mathfrak{F}}_{\alpha} f_{e\sigma n\alpha}^{(f_{\perp})} = J_{e\sigma n}^{(f)} n_{e\sigma n}^{(f)} \tilde{\mathfrak{F}}_{\alpha} \tilde{f}_{e\sigma n\alpha}^{(f_{\perp})} \quad (3.17)$$

where  $J_{epn}^f = \det \mathbf{J}_{en}^{-1}(\tilde{\mathbf{x}}_{e\sigma}^{(f)})$ . Using the definition of common normal flux in the transformed space, an approximation for the divergence of the continuous flux can be defined (see equation 3.18)

$$\left( \tilde{\nabla} \mathbf{f} \right)_{epn\alpha}^{(u)} = \left[ \tilde{\nabla} \cdot \mathbf{g}_{e\sigma}^{(u)}(\tilde{\mathbf{x}}) \left\{ \tilde{\mathfrak{F}}_{\alpha} \tilde{f}_{e\sigma n\alpha}^{(f_{\perp})} - \tilde{f}_{e\sigma n\alpha}^{(f_{\perp})} + f_{e\sigma n\alpha}^{(f_{\perp})} \right\} + \tilde{\mathbf{f}}_{e\sigma n\alpha}^{(f_{\perp})} \cdot \tilde{\nabla} \ell_{ev}^{(u)}(\tilde{\mathbf{x}}) \right]_{\tilde{\mathbf{x}}=\tilde{\mathbf{x}}_{ep}^{(u)'}} \quad (3.18)$$

resulting into a semi-discretised form of the governing system,

$$\frac{\partial u_{epn\sigma}^{(u)}}{\partial x} = -J_{epn}^{-1(u)} (\tilde{\nabla} \cdot \tilde{\mathbf{f}})_{epn\alpha}^{(u)} \quad (3.19)$$

where  $J_{epn}^{(f)} = \det \mathbf{J}_{en}^{-1} (\tilde{\mathbf{x}}_{ep}) = \frac{1}{J_{epn}^{(u)}}$ .

The semi-discrete form of Navier Stokes is a simplified set of ordinary differential equations in time. Finally, this system can be solved by using any time discretization scheme (Witherden et al., 2014).

### 3.1.2 Time Discretization

For this study, the discretized compressible Navier-Stokes are solved using the Runge-Kutta Fehlberg method (RK45). This method combined the Runge-Kutta fourth order method (RK4), with an additional function evaluation for error estimation which allows to determine the proper step size for the solution. To apply RK45, first an approximation to the solution of the initial value problem is made using RK4 (Mathews and Fink, 2003).

$$y_{k+1} = y_k + \frac{25}{216}k_1 + \frac{1408}{2565}k_3 + \frac{2197}{4101}k_4 - \frac{1}{5}k_5 \quad (3.20)$$

Followed by a better approximation of the solution using six function evaluations.

$$z_{k+1} = y_k + \frac{16}{135}k_1 + \frac{6656}{12825}k_3 + \frac{28561}{56430}k_4 - \frac{9}{50}k_5 + \frac{2}{55}k_6 \quad (3.21)$$

For equations 3.20 and 3.21, each step requires the use of the following six values where,

$$k_1 = hf(f_k, y_k) \quad (3.22a)$$

$$k_2 = hf\left(t_k + \frac{1}{4}h, y_k + \frac{1}{4}k_1\right) \quad (3.22b)$$

$$k_3 = hf\left(t_k + \frac{3}{8}h, y_k + \frac{3}{32}k_1 + \frac{9}{32}k_2\right) \quad (3.22c)$$

$$k_4 = hf\left(t_k + \frac{12}{13}h, y_k + \frac{1932}{2197}k_1 - \frac{7200}{2197}k_2 + \frac{7296}{2197}k_3\right) \quad (3.22d)$$

$$k_5 = hf\left(t_k + h, y_k + \frac{439}{216}k_1 - 8k_2 + \frac{3680}{513}k_3 - \frac{845}{4104}k_4\right) \quad (3.22e)$$

$$k_6 = hf\left(t_k + \frac{1}{2}h, y_k - \frac{8}{27}k_1 + 2k_2 - \frac{3544}{2565}k_3 + \frac{1859}{4104}k_4\right) - \frac{11}{40}k_5 \quad (3.22f)$$

At each iteration two solution values are calculated and compared with the following conditions: If the two solutions are in close agreement, the approximation is accepted. If the two answers differ to a certain accuracy defined by the user, the step size is reduced. If the answers agree to more significant digits than required, the step size is increased. According to Mathews and Fink (2003), the proper step size  $h$  can be determined by multiplying the scalar  $s$  times the current step size  $h$  as shown in equation 3.23.

$$s = \left( \frac{tolh}{2|z_{k+1} - y_{k+1}|} \right)^{1/4} \approx 0.84 \left( \frac{tolh}{2|z_{k+1} - y_{k+1}|} \right) \quad (3.23)$$

### 3.2 Nek5000

The fast and scalable fluid/thermal simulation code Nek5000 developed by Argonne National Laboratory (2017) is designed to simulate laminar, transitional and turbulent flows at Low Mach numbers. Applications for this code are diverse ranging from fluid flow and heat transfer to combustion and magnetohydrodynamics. This high order solver is based on the spectral element method (SEM), which combines spectral methods with

finite element method for high-level discretization (Patera, 1984). This approach divides the computational domain in a finite number of elements and the basis on each element corresponds to polynomials up to order  $N$ . The combination of these approaches provides a high-order weighted residual technique that combines the geometric flexibility of finite elements with the rapid convergence and tensor-product efficiencies of global spectral methods. This high order approach has an exponential decay of error proportional to the increment of the polynomial order. Besides, the SEM approach is highly suitable for unsteady phenomena since it offers minimal dissipation and dispersion, high accuracy and exponential solution convergence. Tailored for structured and certain unstructured grids (no hanging nodes), the framework is written in Fortran77 and C and uses MPI for message passing. It provides a highly scalable platform from personal workstations to large supercomputers of diverse architectures (Offermans, 2017).

*Table 3.2*

*NEK5000 Capabilities*

Dimensions	2D,3D
Elements	Quadrilaterals, Hexahedra
Spatial orders	User defined $N$ th order polynomial
Time steppers	Backward difference, Extrapolation
Precisions	Single, Double
Platforms	CPUs via MPI
Governing Equations	Euler, Incompressible Navier-Stokes

Table 3.2 summarizes the capabilities of the open-source framework. In the present study, this framework is used to perform simulations of a three-dimensional incompressible wall-jet in a CRAY CPU cluster.

### 3.2.1 Spatial Discretization

To explain the spatial discretization lets consider the non-dimension incompressible Navier-Stokes equations presented in eqns. 3.24 and 3.25

$$\nabla \cdot \mathbf{u} = 0 \quad (3.24)$$

$$\frac{\partial \mathbf{u}}{\partial t} + (\mathbf{u} \cdot \nabla) \mathbf{u} = -\nabla p + \frac{1}{Re} \nabla^2 \mathbf{u} + \mathbf{f} \quad (3.25)$$

where  $\mathbf{u}(\mathbf{x}, t)$  is the velocity,  $p(\mathbf{x}, t)$  is the pressure and  $\mathbf{f}(\mathbf{x}, t)$  is the forcing term. The Reynolds number  $Re$  is defined as  $Re = \frac{ul}{\nu}$ , where  $u$  is the velocity scale,  $l$  the length scale, and  $\nu$  the kinematic viscosity of the fluid. The incompressible Navier-stokes are consider in an  $\Omega$  arbitrary domain with associated initial and boundary conditions. Consider  $d$  dimensions, where eqns. 3.24 and 3.25 can be reconstruct as a weak form

$$\left( \frac{\partial \mathbf{u}}{\partial t}, \mathbf{v} \right) + ((\mathbf{u} \cdot \nabla) \mathbf{u}, \mathbf{v}) = (-\nabla p, \mathbf{v}) + \left( \frac{1}{Re} \nabla^2 \mathbf{u}, \mathbf{v} \right) + (\mathbf{f}, \mathbf{v}) \quad \forall \mathbf{v} \in X_0 \quad (3.26)$$

$$(\nabla \cdot \mathbf{u}, q) = 0, \quad \forall q \in Z \quad (3.27)$$

where

$$(\mathbf{a}, \mathbf{b}) = \int_{\Omega} \mathbf{a}(\mathbf{x}) \cdot \mathbf{b}(\mathbf{x}) d\mathbf{x} \quad \forall \mathbf{a}, \mathbf{b} \in L^2(\Omega) \quad (3.28)$$

$$X = \{ \mathbf{v} : \{ \mathbf{v}_i \in H^1(\Omega), i = 1, \dots, d, \mathbf{v} = \mathbf{g}_D \text{ on } \Gamma_D \} \} \quad (3.29)$$

$$X_0 = \{ \mathbf{v} : \{ \mathbf{v}_i \in H^1(\Omega), i = 1, \dots, d, \mathbf{v} = 0 \text{ on } \Gamma_D \} \} \quad (3.30)$$

$$Z = L^2(\Omega) \quad (3.31)$$

$L^2$  is the Lebesgue space with  $L_2$ -norm and  $H^1$  is the Sobolev space of functions belonging to  $L^2$ .  $\Gamma_D$  represents the limit of the domain where Dirichlet boundary

conditions are applied. The inner products observed in equations 3.26 and 3.27 are computed using Gauss quadrature.

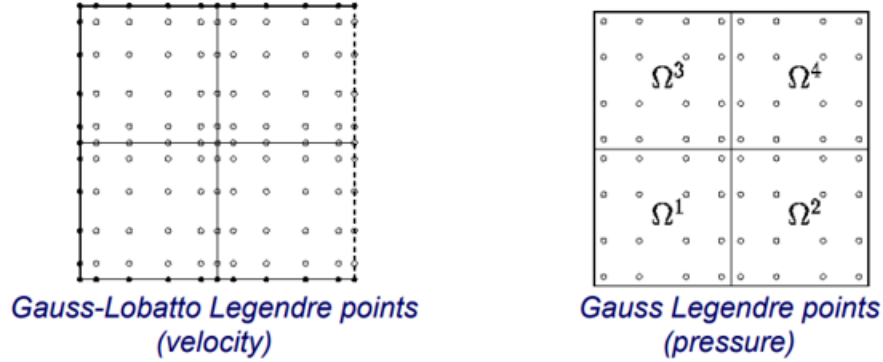


Figure 3.2 Point distributions for velocity and pressure using  $P_N - P_{N-2}$  method by Paul F. Fischer and Kerkemeier (2008).

For the Nek5000 framework, the polynomial associated to the Gauss quadrature are Legendre polynomials ( $L_N$  of order  $N$ ) and the correspondent points are the Gauss-Lobatto-Legendre (GLL) points for velocity (Offermans, 2017). The order of the polynomial is defined by the user and ranges typically between 7 and 15. In the case of pressure, the user can choose between GLL points and Gauss-Lobatto points (GL) as shown in Figure 3.2 described by Paul F. Fischer and Kerkemeier (2008). The GLL points, designated as  $\xi_i, i = 0, \dots, N$ , satisfy Equation 3.32

$$(1 - \xi^2)L'_N(\xi) = 0, \quad \xi \in [-1, 1] \quad (3.32)$$

The associated Gaussian quadrature for a one-dimensional domain is defined as

$$\int_{-1}^1 u(r) dr \approx \sum_{k=0}^N \rho_k u(\xi_k) \quad (3.33)$$

The global domain  $\Omega$  is partitioned into  $E$  number of non-overlapping elements, which are high-order quadrilateral (or hexahedral) elements. Inside each element,  $\Omega^e$ , the basis functions are given by  $\mathbb{P}_N(\Omega^e)$ , which represents the set of polynomials of order  $N$ . Hence the space  $X$  from the weak formulation is limited to a finite dimensional subspace such that

$$X^N = X \cap \mathbb{P}_{N,E}^d \quad (3.34)$$

where  $\mathbb{P}_{N,E}^d$  represents the distribution of polynomials on each of the  $E$  elements. To choose the subspace  $Z^N$  there are two options:  $Z^N \equiv X^N$  or  $Z^N \equiv \mathbb{P}_{N-2,E}^d$ . The first option is known as  $\mathbb{P}_N - \mathbb{P}_N$ , where the pressure and velocity points are collocated and spurious modes are bypass using a method developed by Tomboulides et al. (1997). The second is referred as  $\mathbb{P}_N - \mathbb{P}_{N-2}$ , for this method the spurious modes are retained by considering a  $N - 2$  Lagrange interpolants for the pressure calculation. On each element, the basis functions for  $X^N$  are defined using Lagrangian interpolants of order  $N$  on the correspondent GLL quadrature points. Notice that according to Galerkin methods, the test functions are identical to the basis functions. When working in multi-dimensions, the solutions are presented via tensor products of the basis polynomials, for instance for a two dimensional case the associated Lagrange interpolants are written such that

$$\pi_{i,j}^N(r,s) = \pi_i^N(r)\pi_j^N(s), \quad (r,s) \in [-1,1] \times [-1,1] \quad (3.35)$$

where the Lagrangian interpolants are defined as  $\pi_i(\xi_j)$ . A visualization of the resultant grid by combining the user defined grid given by the finite element (FE) and the inner GLL points given by the spectral is presented in Figure 3.3 (Offermans, 2017).



Considering the global domain is partitioned into E number of elements, which are high-order quadrilateral (or hexahedral) elements. The solution for the governing equations can be mapped within each element as an expansion of the local Lagrangian Nth-order polynomials cast in tensor-product form as presented in Equation 3.36.

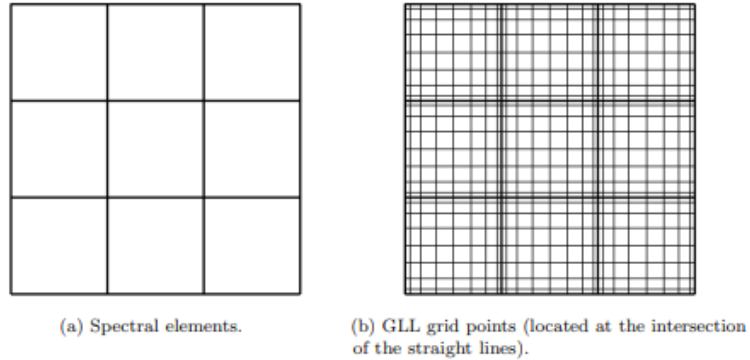


Figure 3.3 Spectral element methods (SEM) grid (Offermans, 2017).

$$u(x) = \sum_{i=0}^N \hat{u}_i L_i(r) \quad (3.36)$$

Where  $\hat{u}_i$  is the spectral coefficient of  $u(x)$  based on the order  $i$  of the Legendre polynomial,  $L_i(r)$ . The trial and test functions represented as Nth-order tensor-product polynomials within each element in combination with the E number of elements will represent the number of grid points as  $EN^3$  for a three-dimensional mesh (Offermans, 2017). For the spectral element method an assembly of local operator referred as local spectral matrices are defined to define the semi-discrete system. On each element the local mass matrix and the local stiffness are defined as equations 3.37 and 3.38.

$$\mathbf{M}_{ij}^e = \frac{L^e}{2} \int_{\hat{\Omega}} \pi_i(r) \pi_j(r) \approx \frac{L^e}{2} \sum_{k=0}^N \rho_k \pi_i(\xi_k) \pi_j(\xi_k) = \frac{L^e}{2} \rho_i \delta_{ij} \quad (3.37)$$

$$\mathbf{K}_{ij}^e = \frac{2}{L^e} \int_{\hat{\Omega}} \frac{d\pi_i(r)}{dr} \frac{d\pi_j(r)}{dr} dr = \frac{2}{L^e} \sum_{k=0}^N \rho_k \frac{d\pi_i(\xi_k)}{dr} \frac{d\pi_j(\xi_k)}{dr} \quad (3.38)$$

Since each operator acts locally and independently on each element a continuity enforcement is required, therefore; these local operators are unasssembled forming diagonal matrices denoted as  $\mathbf{M}_L$ ,  $\mathbf{K}_L$ , and  $\mathbf{D}_L$  which are mass, stiffness and derivative matrices respectively. The grid definition between local and global mapping differs as seen in Figure 3.4, hence continuity need to be enforced at the interface Offermans (2017).

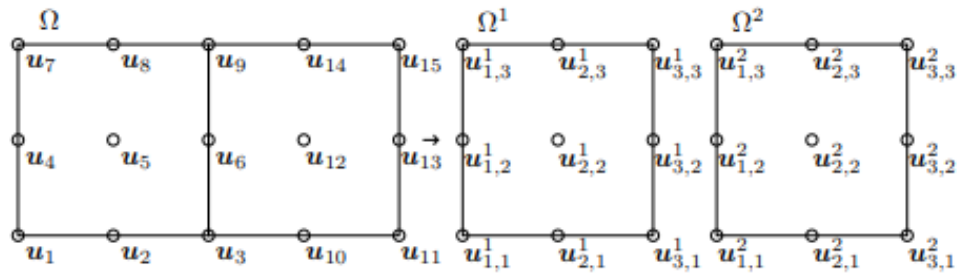


Figure 3.4 Mapping between local (left) and global (right) numbering for a domain of two spectral elements (Offermans, 2017).

Equation 3.39 and 3.40 defined the mapping vectors at local and global domain for the example in Figure 3.4.

$$\underline{\mathbf{u}} = (\mathbf{u}_1, \mathbf{u}_2, \dots, \mathbf{u}_{15})^T \quad (3.39)$$

$$\underline{\mathbf{u}}_L = (\mathbf{u}^1_{1,1}, \mathbf{u}^1_{1,2}, \dots, \mathbf{u}^1_{3,3}, \mathbf{u}^2_{1,1}, \mathbf{u}^2_{1,2}, \dots, \mathbf{u}^2_{3,3})^T \quad (3.40)$$

To introduce continuity between these vectors a connectivity matrix is defined,  $\mathbf{Q}$  to map  $\underline{\mathbf{u}}$  to  $\underline{\mathbf{u}}_L$ . The operation shown in equation 3.41 is defined as scatter from global to local vector, while the reverse operation shown in equation 3.42 is defined as gather (Offermans, 2017).

$$\underline{\mathbf{u}}_L = \mathbf{Q}\underline{\mathbf{u}} \quad (3.41)$$

$$\underline{\mathbf{v}} = \mathbf{Q}^T \underline{\mathbf{u}}_L \quad (3.42)$$

Using the operators described above, the incompressible Navier Stokes can be written as the semi-discrete problem presented on equations 3.43 and 3.44, where  $\underline{p}$  and  $\underline{u}$  are taken to be the discrete form of the pressure and velocity fields

$$\mathbf{M} \frac{d\underline{u}_i}{dt} + \mathbf{C} \underline{u}_i = \mathbf{D}_i^T \underline{p} - \frac{1}{Re} \mathbf{K} \underline{u}_i + \mathbf{M} \underline{f}_i, i = 1, \dots, d \quad (3.43)$$

$$D_i \underline{u}_i = 0 \quad (3.44)$$

where  $\mathbf{M}$  is the global mass matrix,  $\mathbf{C}$  is the convection operator,  $\mathbf{D}_i$  is the global first derivative in the direction  $i$  and  $\mathbf{K}$  is the global stiffness matrix. Note the matrix  $\mathbf{D}_i$  depends on the method used for pressure resolution, if  $\mathbb{P}_N - \mathbb{P}_N$  is used the matrix is squared else if  $\mathbb{P}_N - \mathbb{P}_{N-2}$  the matrix is rectangular  $((N-1) \times (N+1))$ . Given the discretized form of the governing equations, the framework proceeds to discretize the domain in time.

### 3.2.2 Time Discretization

Temporal discretization is accomplished by implicit backward differentiation (BDF) subject to the given initial conditions. Due to the complexity of implicit behavior and to obtain more computational efficiency, some of the terms are solve using  $k$ -th order extrapolation. This method solves the advective term using the convective form of BDF and an extrapolation (EXT) formula. Equation 3.45 defines the times discretization method of order  $k$

$$\sum_{j=0}^k \frac{b_j}{\Delta t} \mathbf{M} \underline{u}_i^{n-j} + \sum_{j=1}^k a_j \mathbf{C} \underline{u}_i^{n-j} = \mathbf{D}_i^T \underline{p}^n - \frac{1}{Re} \mathbf{K} \underline{u}_i^n + \mathbf{M} \underline{f}_i^n \quad (3.45)$$

$$\mathbf{D}_i \underline{u}_i = 0, i = 1, \dots, d \quad (3.46)$$

where  $b_j$  are the coefficients correspondent to BDF and  $a_j$  are the coefficients correspondent to EXT.

To obtain the approximate solution, the fractional step method is used. This enables decoupling of viscous and pressure terms via a time splitting operation on equations 3.45 and 3.46. To explain the Helmholtz operator is defined as

$$\mathbf{H} = \frac{b_o}{\Delta t} \mathbf{M} + \frac{1}{Re} \mathbf{K} \quad (3.47)$$

and we let

$$\underline{\mathbf{r}}_i^n = - \sum_{j=1}^k \frac{b_j}{\Delta t} \mathbf{M} \underline{\mathbf{u}}_i^{n-j} - \sum_{j=1}^k a_j \mathbf{C} \underline{\mathbf{u}}_i^{n-j} + \mathbf{M} \underline{\mathbf{f}}_i^n \quad (3.48)$$

For the simulations performed under this work, the  $\mathbb{P}_N - \mathbb{P}_{N-2}$  method is considered. For this specific method, a block LU-descomposition is performed and the system to be solved is defined as

$$\mathbf{H} \underline{\mathbf{u}}_i^* = \mathbf{D}_i^T \underline{p}^{n-1} + \underline{\mathbf{r}}_i^n \quad (3.49)$$

$$- \frac{b_o}{\Delta t} \mathbf{D}_i \mathbf{M}^{-1} \mathbf{D}_i^T (\underline{p}^n - \underline{p}^{n-1}) = \mathbf{D}_i \underline{\mathbf{u}}_i^* \quad (3.50)$$

$$\underline{\mathbf{u}}_i^n = \underline{\mathbf{u}}_i^* + \frac{\Delta t}{b_o} \mathbf{M}^{-1} \mathbf{D}_i^T (\underline{p}^n - \underline{p}^{n-1}) \quad (3.51)$$

For specifications to solve the system using the  $\mathbb{P}_N - \mathbb{P}_N$  method refer to Offermans (2017).

### 3.2.3 Tripping Force

To speed the transition from laminar to turbulent regime, a random volume force is applied on the normal direction to a certain section of the domain. The section below

explains the physics behind the implemented subroutine. A more detailed description and validation of the module can be found on the study by Schlatter and Örlü (2012) on turbulent boundary layers. The line tripping module follows the structure of the tripping force implemented in the SIMSON code (Chevalier et al., 2007). The intent of the line tripping module is to mimic the behavior of physical sand paper. The forcing is applied in the elliptical region along the user defined line(s) by the smoothing lengths *SMTHX* and *SMTHY* which are rotated counterclockwise by the *ROTA* angle. The rotation angle is also used to rotate the components of the force into a normal position with respect to the wall. The smoothing force is expressed as the set of Equation 3.52

$$f_{smth}(r) = \begin{cases} \exp(-r^2)(1-r^2)^2 & \text{if } r \leq 1.0 \\ 0 & \text{if } r > 1.0 \end{cases} \quad (3.52)$$

where

$$r^2 = \left( \frac{x_{rot}}{SMTHX} \right)^2 + \left( \frac{y_{rot}}{SMTHY} \right)^2 \quad (3.53)$$

and

$$x_{rot} = x_{tr} * \cos(ROTA) + y_{tr} * \sin(ROTA) \quad (3.54)$$

$$y_{rot} = -x_{tr} * \sin(ROTA) + y_{tr} * \cos(ROTA) \quad (3.55)$$

In equations 3.54 and 3.55,  $x_{tr}$  and  $y_{tr}$  correspond to the GLL point coordinates where the tripping line is positioned. The randomness of the function is increased by having both steady and unsteady parts where the amplitudes correspond to *TIAMP* and *TDAMP* respectively. Equations 3.56 and 3.57 define the components of the tripping force.

$$f_x = -f_{smth}(r) * f(z, t) * \sin(ROTA) \quad (3.56)$$

$$f_y = f_{smth}(r) * f(z, t) * \cos(ROTA) \quad (3.57)$$

where,

$$f(z, t) = TIAMP * g(z) + TDAMP * [(1 - b(t))h^i(z) + b(t)h^{i+1}(z)] \quad (3.58)$$

and

$$i = \text{int}\left(\frac{t}{TDT}\right) \quad (3.59)$$

$$b(t) = 3p^2 - 2p^3 \quad (3.60)$$

$$p = \frac{t}{TDT} - i \quad (3.61)$$

In Equation 3.58,  $g(z)$  and  $h(z)$  are Fourier series of unit amplitude with NMODE random coefficients. This volume force generates noise with a uniform distribution over all frequencies lower than the cutoff frequency corresponding to  $2\pi/TDT$ .  $TDT$  is the time step for the change on the time dependent part of the trip as described in Schlatter and Örlü (2012) study.

## 4. Compressible Wall-Jet

### 4.1 Computational Set-up

The computational domain for the two-dimensional compressible wall-jet is in the shape of a rectangle with dimensions are based on the jet inlet height,  $h$ . The physical rectangle dimensions are  $L_x = 46h$  in the stream-wise direction, and  $L_y = 23h$  in the normal direction, the domain is based on a two-dimensional approach for the computational domain from Ahlman et al. (2007). The streamwise direction is chosen to be sufficiently large to achieve self-similar behavior. The simulations are performed in an unstructured grid with 752025 gridpoints.

This grid is refined using a stretching function, which allows bigger cells towards the top of the domain. In addition boundary layer refinement is added near the wall and at the inlet to capture the wide range of velocity and length scales which are characteristic of a wall-jet. Figure 4.1 presents the computational mesh defined for this compressible case. The inlet height is denoted as  $h$  and  $x$ , and  $y$  denote the streamwise and wall-normal directions, respectively. The inlet jet is positioned parallel to the streamwise direction and adjacent to the bottom wall as observed in Figure 4.1. The fluid is injected tangentially along the wall. The simulations as previously mentioned are performed using PyFR with third order polynomial for spatial discretization and RK5 for time discretization.

To promote the transition to turbulent regime, roughness is introduced near the inlet for a distance of  $x = 3h$ , ensuring fully turbulent flow in large part of the domain. The roughness, observed in Figure 4.1, is placed  $2h$  away from the inlet and has a triangular shape with a height of 10% of the inlet height.

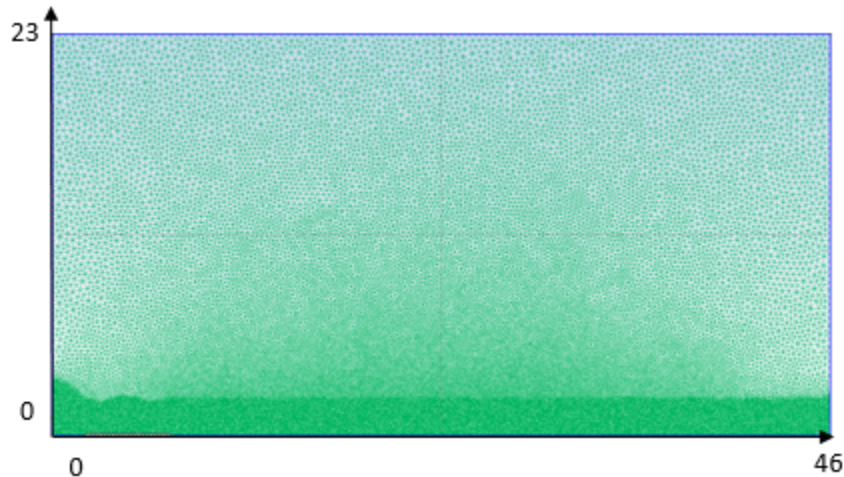


Figure 4.1 Compressible Wall-Jet Mesh.

#### 4.1.1 Inlet and Boundary Conditions

Figure 4.2 illustrates the boundary conditions prescribed for the compressible case. The Mach number used for the simulation is  $M=0.5$  and the inlet Reynolds number is  $Re = 5000$ . The fluid is introduced to the domain at the jet inlet of height,  $h = 1\text{ cm}$ . The baseline inlet profile for the three cases consists of a jet inlet velocity,  $U_i$ , which includes a co-flow that is 10% of the inlet velocity,  $U_c = 0.1U_i$ . This co-flow is applied to ensure that the large-scale eddies propagate downstream and leave the computational domain. Co-flow is added because it increases the parametric flexibility of a wall-jet by allowing us to change the ratio between the freestream velocity outside the boundary layer and the jet velocity near the wall. Thus, the turbulent structure of the wall jet can be manipulated and the importance of the outer vortical layer on the wall region can be evaluated.

The wall boundary is flat and smooth, except at the roughness section, with no slip condition to include viscous effects and shear stresses in the study. At the bottom wall, the no-slip isothermal condition is fulfilled for the velocity such that  $u = v = 0$ . At the top of



the domain, an inflow velocity of 2.6 % of the jet inlet is applied to account for entrainment.

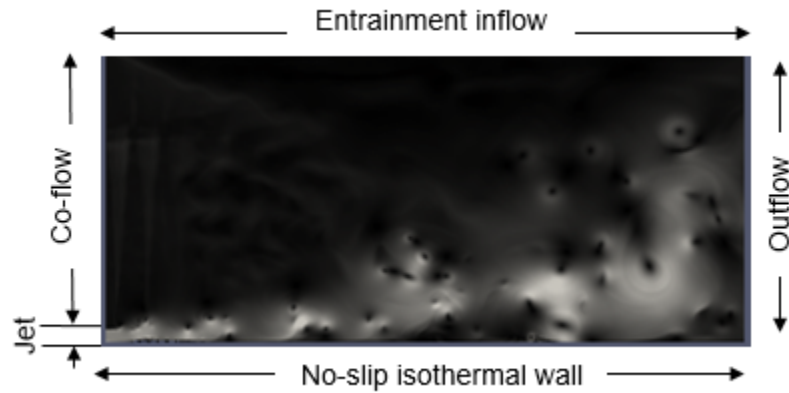


Figure 4.2 Compressible Wall-Jet Boundary Conditions.

At the outlet, a characteristic-Riemann invariant with standard environment conditions ( $P = 101,325Pa$  and  $T = 25C$ ) is applied to prevent the reflection and generation of pressure waves. The outflow ensure all eddies exit the domain and avoid any back pressure. The fluid is assumed to be calorically perfect ( $C_p$  is constant) and it follows the perfect gas law.

Table 4.1

Compressible Case Study Description

	<b>Baseline Case</b>	<b>Case 1</b>	<b>Case 2</b>
Inlet Mach Number	0.5	0.5	0.5
Co-flow Velocity	$0.1 U_{in}$	$0.1 U_{in}$	$0.1 U_{in}$
Entrainment Velocity	$0.026 U_{in}$	$0.026 U_{in}$	$0.026 U_{in}$
Inlet Perturbations	—	$0.1U_{in}(\sin 4440 t)$	$0.1U_{in}(\sin 850 t)$
Strouhal Number	—	0.25	0.05

The study aims to compare two different velocity inlet profiles with the baseline for turbulence modulation. For the two forced cases, the inlet profile includes a sine wave

perturbation based on Strouhal number ( $Sr$ ) variation as presented in Table 4.1. Case 1 refers to the high- $Sr$  case and Case 2 refers to the low- $Sr$  case.

## 4.2 Results

Two-dimensional simulations were performed in order to describe the primary instability process of the baseline and forced compressible planar wall jet. In addition the two-dimensional mesh will help analyze the computational need for a future three-dimensional version.

### 4.2.1 Instantaneous Fields

Visualizations of the instantaneous velocity, density, and pressure fields are presented in Figure 4.3. Using the velocity field, the change from laminar to the turbulent regime is observed. The transition occurs rapidly after the fluid undergoes the imposed roughness near the jet inlet, becoming fully turbulent beyond  $x > 20h$ . Beyond position  $x > 20h$ , there is a higher presence of vortices and velocity fluctuations. The flow is subject to two shear processes causing the formation of vortices in the opposite direction. One is caused by Kelvin Helmholtz instabilities at the initial shear layer between the nozzle and the co-flow and the second is caused by the introduced roughness at the wall. The interacting eddies have different characteristics that reflect on the downstream domain. In Figure 4.3, one can observe that the flow experiences detachment from the wall at an earlier stage than expected. Leading to the conclusion that the vortices produced by the roughness are overtaking the ones from the instability.

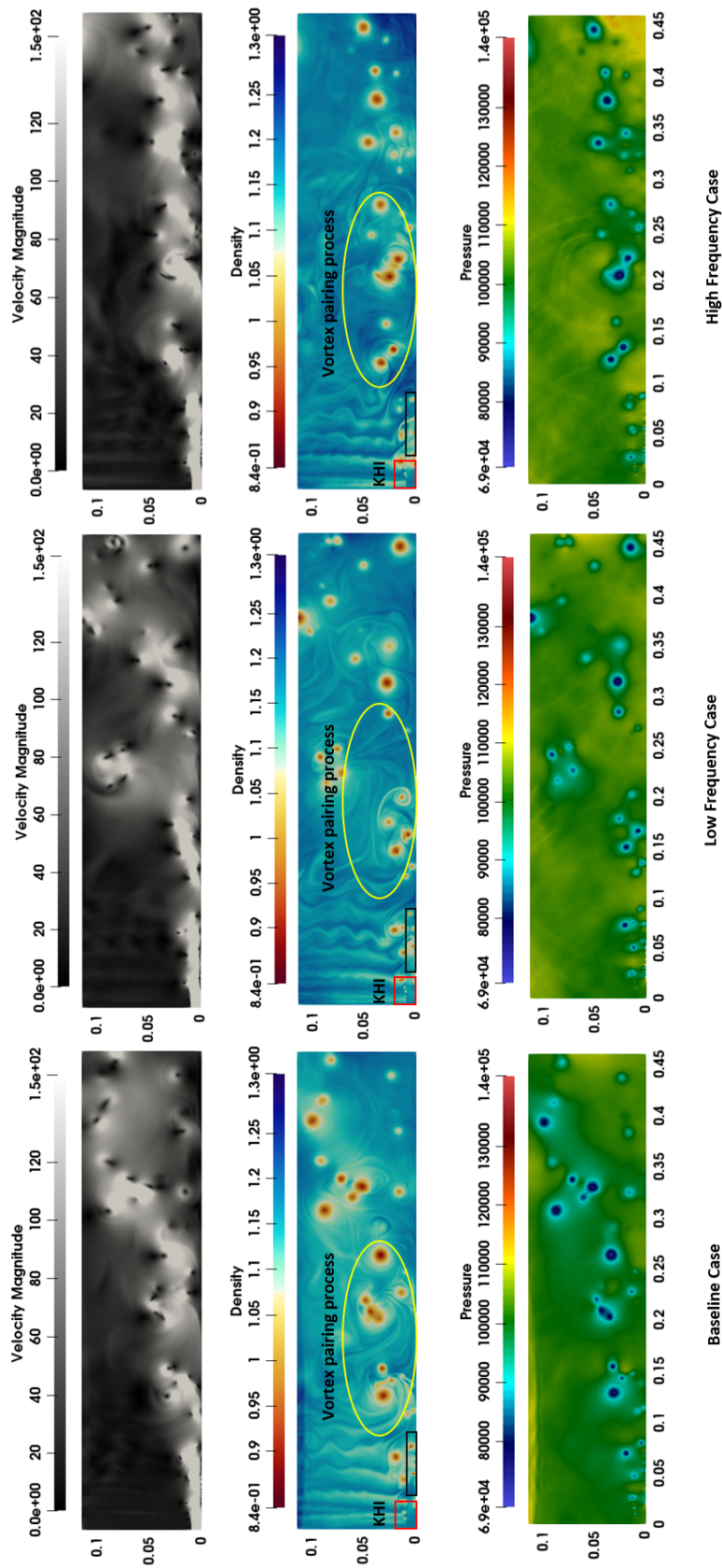


Figure 4.3 Instantaneous velocity, density, and pressure fields for the three compressible case at  $t = 6.75s$ . Red square highlights pure Kelvin-Helmholtz instabilities, black rectangle the vortices produce by the roughness, and the yellow oval focuses on the primary and secondary vortex process undergoing the flow.

Comparing the three cases, one can observe that the low-Sr case shows longer attachment to the wall compared to the other two cases. The baseline presents more chaotic behavior in the downstream domain where the flow tends to re-attach to the wall.

The density and pressure fields in Figure 4.3 highlight the formation of pure Kelvin-Helmholtz instabilities at the inlet. The production of vortices at the roughness is also observed. The eddies formed collapse and propagate downstream over time. The density field shows the direction of the flow wrapping the center of the vortices which enables us to visualize the undergoing vortex process. The pulsed jet controls the amplitude and frequency of eddy production at the inlet which modifies turbulent behavior at downstream positions. The perturbation causes changes in the turbulent kinetic energy and large-scale structures. Large-scales structures frequency modulate the finer scales of turbulence and can be a factor enclosing turbulence modulation. Notice that the vortex pairing process occurs close to the wall for the baseline and low-Sr case, while for the high-Sr case this process occurs further from the wall due to the early separation.

#### 4.2.2 Mean Flow Characteristics

Figure 4.4 presents the decay of the maximum streamwise velocity as function of the local position in the stream wise direction. As characteristic, the maximum velocity decreases as it travels downstream. The decay is quantified by a power law as presented in Equation 4.1.

$$\frac{U_m}{U_{in}} = A_m \left( \frac{x}{h} \right)^{\gamma_m} \quad (4.1)$$

where  $A_m = 2.55$  and  $\gamma_m = -0.4907$ ,  $U_{in}$  is the jet inlet velocity and  $h$  is nozzle height.

The results for this study are compared with Tang et al. (2015) whose power law constants are  $A_m = 3.55$  and  $\gamma_m = -0.4907$  and Barenblatt et al. (2005) with  $A_m = 5.15$  and  $\gamma_m = -0.6$ . The current results follow the same power as Tang et.al with different magnitude. The values for this exponent and for the amplitude are scattered, with an accepted range from  $-0.6 \leq \gamma_m \leq -0.49$  and  $4 \leq A_m \leq 7$  as reported by Narasimha et al.(1973). Streamwise mean velocity decay and wall normal position development are consistent for the three cases studied.

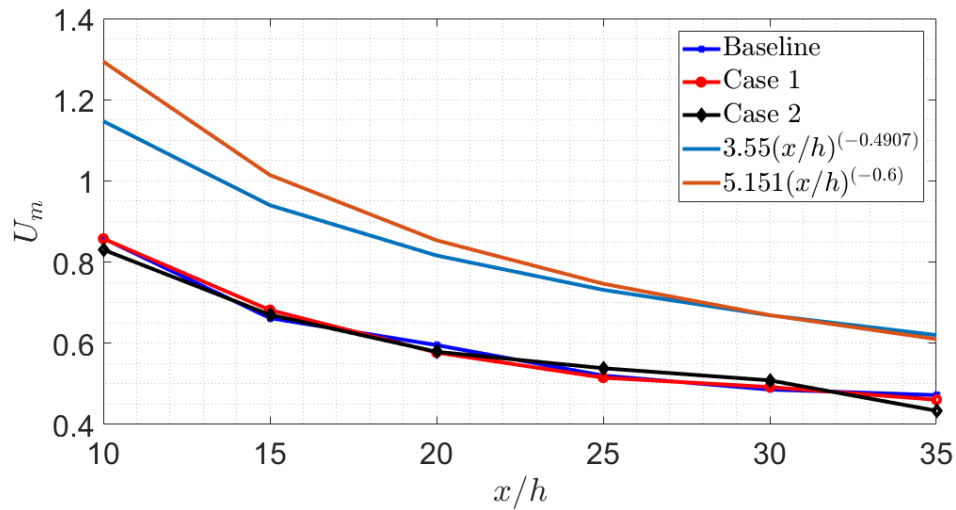


Figure 4.4 Decay of maximum mean stream-wise velocity,  $U_m$  as a function of the streamwise position normalized with the inlet height. Data compared to Tang et al. (2015) blue line and Barenblatt et al. (2005) red line.

Figure 4.5 shows the streamwise evolution of the wall normal location corresponding to  $U_m$ . Following the decay analysis, the wall-normal location can be quantify by a power law given by equation 4.2

$$\frac{y_m}{h} = B_m \left( \frac{x}{h} \right)^m \quad (4.2)$$

where  $B_m = 0.095$  and  $m = 1.05$ . The data is compared with Naqavi et al. (2018) and Tang et al. (2015) which constants are  $B_m = 0.040$  and  $m = 0.717$  and  $B_m = 0.0403$  and  $m = 0.7403$ , respectively.

The comparison cases are incompressible as there was not this literature evaluating this parameter for compressible case. Part of the discrepancies are caused by the different flow conditions in the comparative data. Current data presents higher value constant for the wall-normal position of the maximum velocity, which is likely a consequence of the early flow separation induced by the tripping methodology.

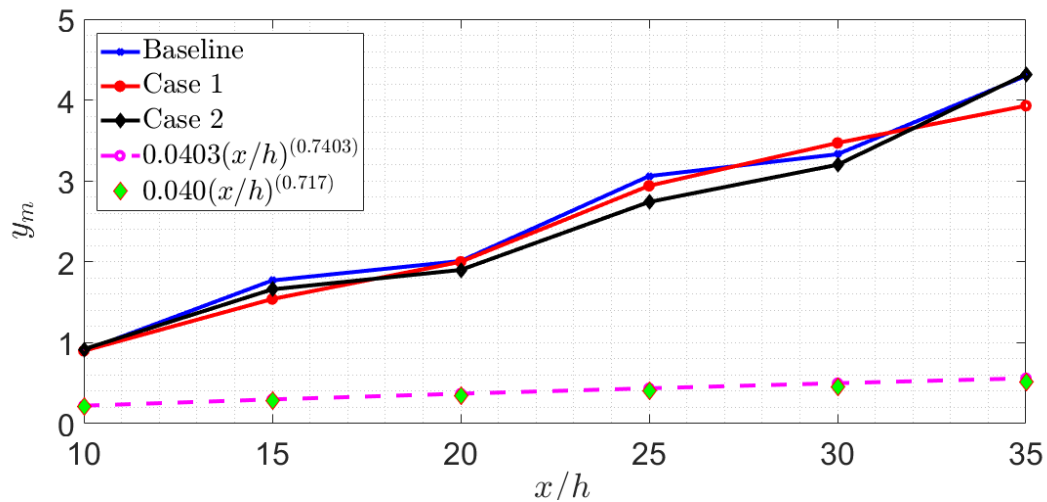


Figure 4.5 Wall-normal position  $y_m$  of the maximum mean stream-wise velocity  $U_m$  as a function of the over stream-wise position  $x$ . Values normalized by the inlet height. Data compared to Tang et al. (2015) magenta dashed line and Naqavi et al. (2018) green  $\diamond$ .

Figure 4.6 presents the skin friction coefficient as a function of the local Reynolds number  $Re_m$ . The  $Re_m$  is taken as  $\frac{U_{max}y_{max}}{\nu}$  and  $C_f = 2(\frac{u\tau}{U_{max}})^2$ . The current study presents lower values of skin-friction; nonetheless, the slope of the decay matches Tachie et al. (2004). The offset could be the product of the early detachment. The variations of skin

friction between cases are fairly small as observed in Figure 4.6; however, the high-Sr case seem to present relatively lower values than the baseline and low-Sr case.

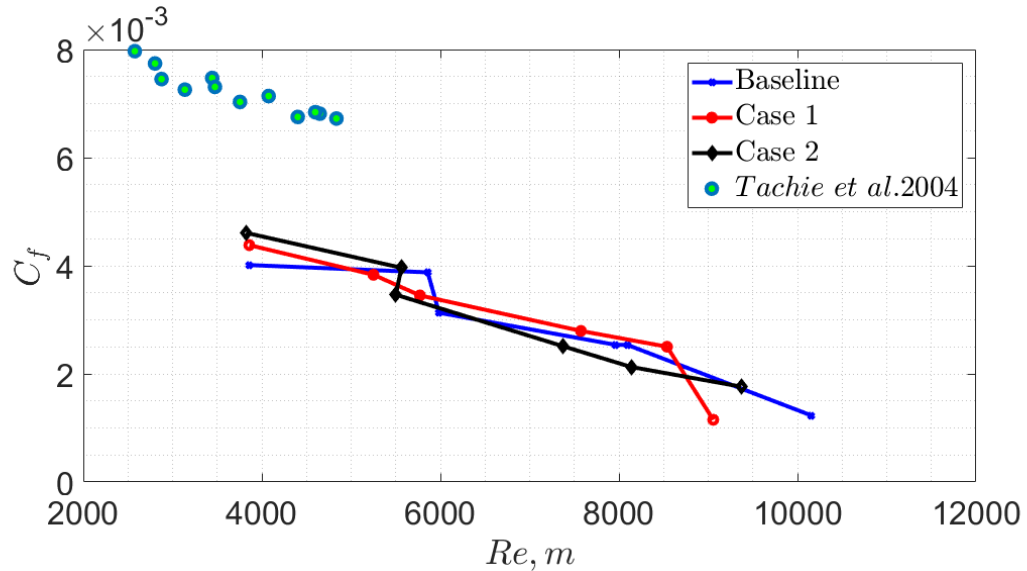


Figure 4.6 Skin friction coefficient as a function of the local Reynolds number. Data compared to Tachie et al. (2004).

To better understand the velocity statistics at upstream and downstream positions of the wall-jet proper inner and outer scaling are applied and presented in the following figures.

For outer scaling, the maximum mean stream-wise velocity and the co-flow velocity ( $U_m - U_c$ ) are used for the velocity scale, and the half-width jet normal position  $y_{1/2}$  is used for the length scale. Figure 4.7 shows the mean stream-wise velocity scaled with outer parameter at  $x/h = 20$  and  $30$ . The mean velocity profile converged in the outer region, some discrepancies are observed in the inner region of the jet. The mean profiles show inconsistency with the conventional incompressible wall-jet profile when compared to Naqavi et al. (2018), but we are 2D compressible, which may contribute to the discrepancy. Notice the early separation from the wall is confirmed by these profiles. As

described in the instantaneous velocity section the high-Sr case presents the earliest separation.

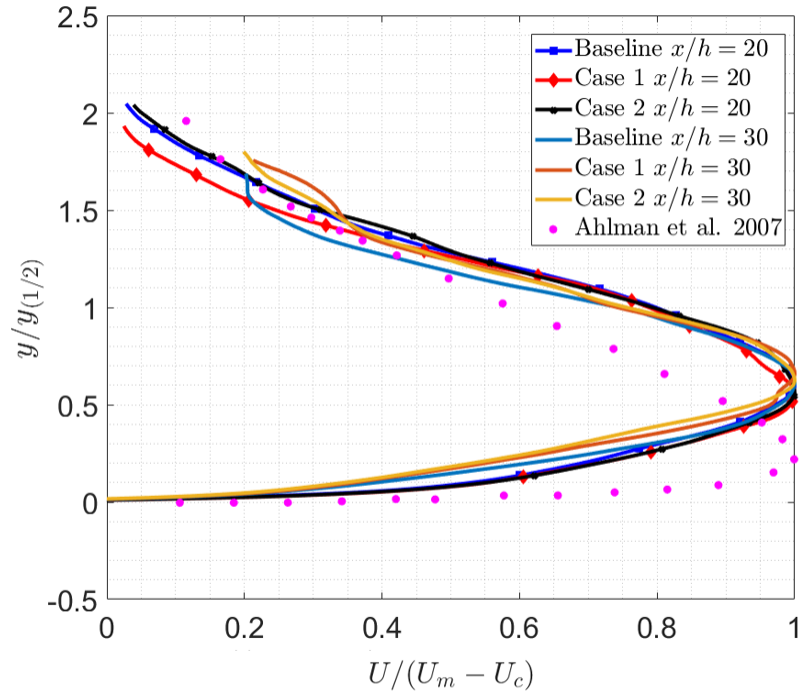


Figure 4.7 Mean stream-wise velocity profiles scaled using outer parameters. Data compared to Naqavi et al. (2018).

For inner scaling, the convention for turbulent boundary layer is followed, where the friction velocity  $u_\tau$  is the velocity scale and  $u_\tau/\nu$  is the length scale. Figure 4.8 presents the mean stream-wise profiles scaled with inner parameters in a semi-logarithmic form. The current results collapsed for any  $y^+ \leq 20$  where the viscous layer and part of the buffer layer are defined. The scaling fails for the outer layer as observed in Figure 4.8. The profiles are also compared with the conventional laws for turbulent boundary layers, where  $\langle u^+ \rangle = y^+$  below  $y^+ = 4$  and  $\langle u^+ \rangle = A \ln(y^+) + B$  for the logarithmic layer. The constant  $A$  and  $B$  are scattered. For different studies for the current results the values of  $A = 2.44$  and  $B = 5.0$  are used. Based on the scaled mean profiles, all the scales near



the wall seem to be captured by the simulation and the discrepancy with the conventional wall-jet profile is not caused by the grid resolution.

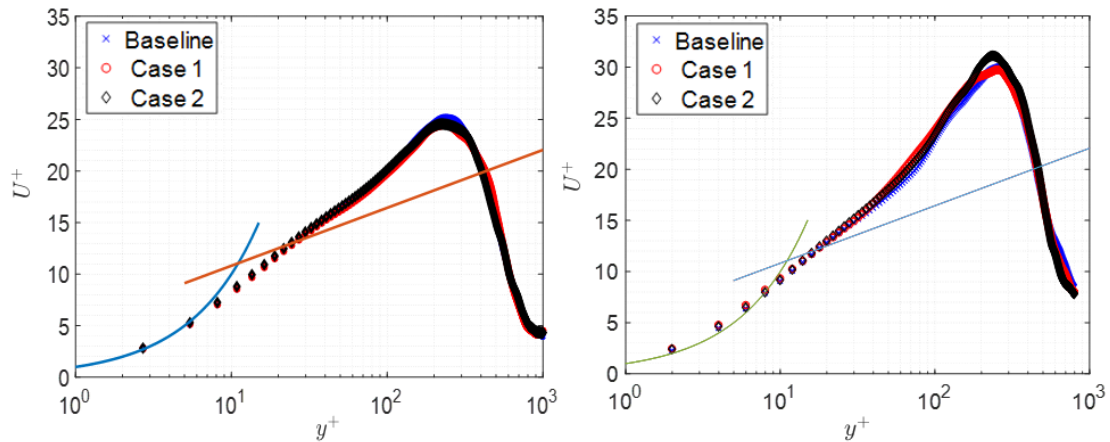


Figure 4.8 Mean stream-wise velocity profiles scaled using inner parameters. Left figure  $x/h = 20$  and right figure  $x/h = 30$ . Blue line  $\langle u^+ \rangle = y^+$  and red line  $\langle u^+ \rangle = A \ln(y^+) + B$ .

### 4.2.3 Turbulent Statistics

The Reynolds stresses are evaluated with inner and outer scaling. For outer scaling, the normal and shear stresses are normalized by  $(U_m - U_c)^2$  and half-width on the length scale. Figure 4.9 shows the normal Reynolds stresses in the stream-wise and the normal direction for two stream-wise positions.

The current results give higher values of turbulent intensity compared to previous experimental and computational studies. Due to the separation from the wall, just a small hint of the characteristic peak of the inner layer is shown at the upstream position. The outer layer weakens the inner layer effects as its intensity is relatively higher. Despite the quantitative discrepancies between the literature and these results, the figure provides relevant information on how the Strouhal number affects the flow development relative to the baseline. In the stream-wise Reynolds stresses, the notable jump at the downstream

position represents a more complex-chaotic flow in the fully developed region. The wall-normal stresses appeared to have an opposite effect as they remain constant in value but they are confined closer to the wall in the downstream domain.

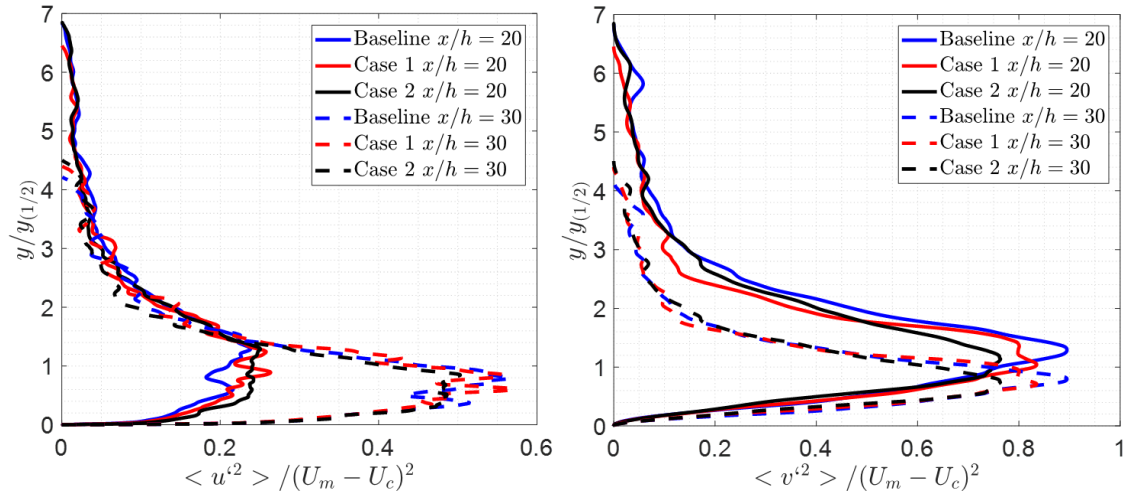


Figure 4.9 Reynolds stresses profiles at two stream-wise positions scaled with outer parameters. Left figure stream-wise  $\langle u'u' \rangle$  - right figure  $\langle v'v' \rangle$ .

The high-Sr case presents the lowest values of turbulent intensity on average. The low-Sr case is close in stream-wise turbulence intensity and slightly lower in wall-normal intensity compared to the baseline case. For inner scaling, the normal and shear stresses are normalized by  $(u_\tau)^2$  on the velocity scale and  $u_\tau/\nu$  on the length scale. The inner scaling allows us to investigate more closely what is happening in the inner region of the jet. Figure 4.10 presents the Reynolds stresses scaled with inner parameter. The inner peak characteristic of the near-wall region is slightly present, and it is more noticeable in the downstream domain. The evident increase of turbulent intensity on the inner and outer regions is observed. The high-Sr case shows a slightly higher stream-wise intensity in the position closer to the jet, but at the downstream position, it is comparable with the other

cases. The low-Sr case shows an appreciable increase in the wall-normal turbulent intensity at the downstream domain.

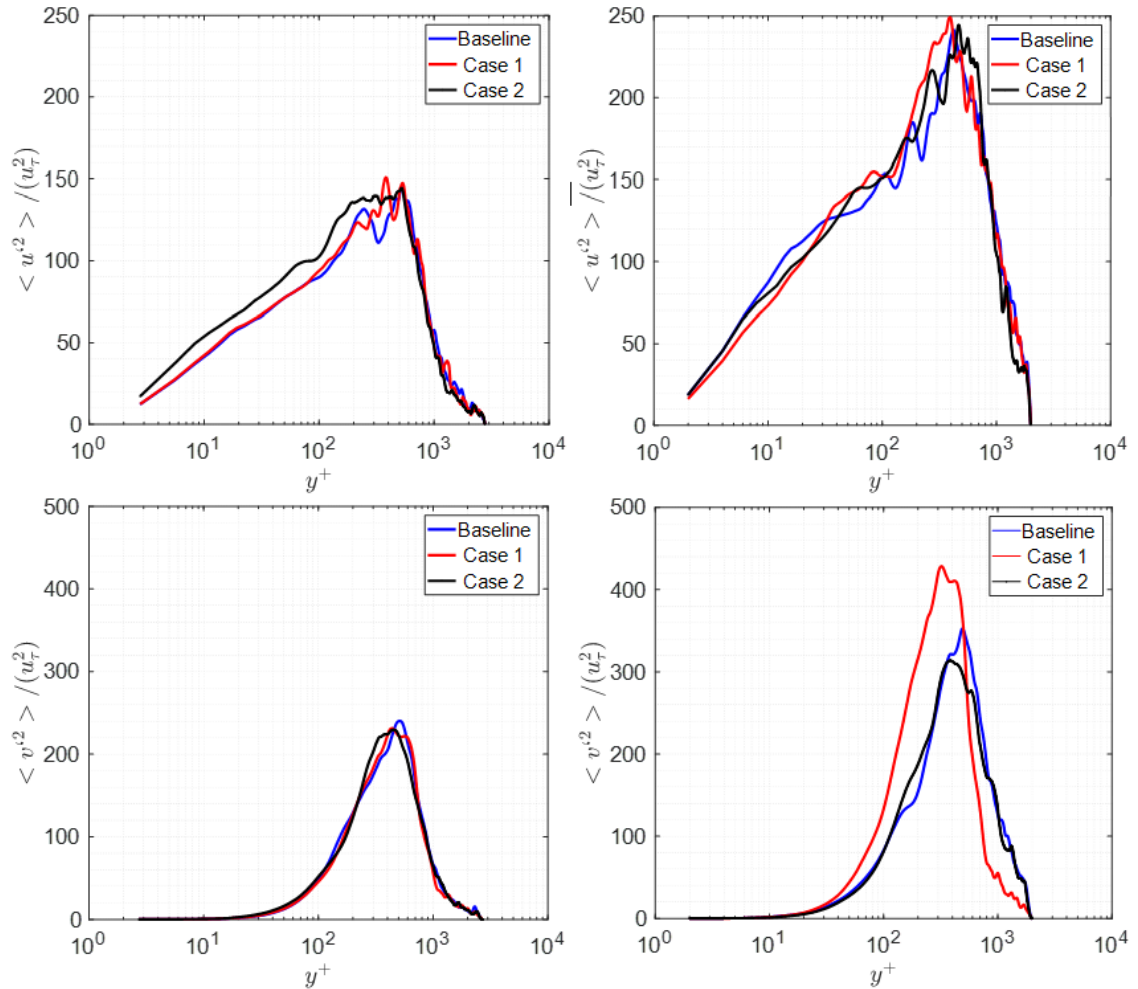


Figure 4.10 Reynolds stresses profiles at two stream-wise positions scaled with inner parameters. Top figures stream-wise  $\langle u'u' \rangle$  - bottom figures  $\langle v'v' \rangle$ .

### 4.3 Conclusions

Direct Numerical Simulations of an unforced and two forced weakly compressible turbulent wall-jets were performed to study turbulence modulation in the flow. The physical domain extends for  $46h$  ( $h$  is the inlet height) and measurements are taken at two

streamwise positions  $x/h = 20$  and  $x/h = 30$  to have a comparison point with previous studies. A summary of the findings is presented below.

1. The mean flow characteristics and turbulence intensities show the flow separates earlier than expected from the wall. From the statistical analysis and the flow visualization the lifting appears to be an effect of the imposed tripping device near the inlet.
2. Tripping roughness needs to be reduced in height to get better comparison with previous studies. However, reducing the tripping device height may require further refinement of the computational grid near the wall.
3. The results indicate that, the sine wave perturbation changes the frequency of billow production by KHI (Kelvin-Helmholtz Instabilities) which contribute to changes in turbulent intensity in the downstream domain.
4. We observe there is a significant increase in the wall-normal intensity near the surface for the lower Strouhal number case ( $Sr = 0.05$ ) when traveling further downstream. The coefficient of friction sustains the results with a increase of magnitude in the sampling area.
5. Far away from the surface, the turbulence intensity in the streamwise and normal direction is slightly reduced for the high Strouhal number ( $Sr = 0.25$ ) case compared to the baseline.
6. The two-dimensional study for compressible wall-jet shows that higher resolution is needed for higher Reynolds number. The computational cost for the compressible case is more demanding than for the incompressible case. The limited availability of

Graphical Processing Units (GPU) computing power did not allow us to proceed with a three-dimensional study.

7. Lessons learned from this compressible case are used as guidelines in the development of the incompressible three-dimensional case study for which the required computational resources were available.

## 5. Incompressible Wall-Jet

### 5.1 Computational Set-up

The computational domain for the three-dimensional incompressible wall-jet is in the shape of a rectangular cuboid, whose dimensions are based on the jet inlet height,  $h$ . The domain dimensions are  $L_x = 50h$ ,  $L_y = 18h$ ,  $L_z = 5.5h$  in the streamwise, normal and spanwise directions, respectively. The domain is based on a two-dimensional approach for the computational domain from Pouransari et al. (2014). The streamwise direction is chosen to be sufficiently large to achieve self-similar behavior. The normal direction enables enough space to avoid boundary treatment issues and the span-wise direction is chosen to be the minimum possible to limit the computational power requirements.

This grid is developed using the embedded Nek5000 subroutine genbox Argonne National Laboratory (2017), in which the streamwise and spanwise directions have elements uniformly distributed along each direction, while the normal direction is refined towards the wall using a stretching function such that

$$N_{y,e} = 1 + [\tanh(\beta * (2 * y - 1)) / \tanh(\beta)] \quad (5.1)$$

where  $\beta$  is a factor that determines how close is the stretching in the vicinity of the wall.

Notice the higher the value the smallest the cells towards the wall, but the coarser the cells away from the wall, hence one should find a balance to capture all the scale of motion.

Figure 5.1 presents the computational mesh defined for the incompressible case. The inlet height is denoted as  $h$  and  $x$ ,  $y$ , and  $z$  denote the streamwise, wall-normal, and spanwise directions, respectively. The jet inlet is positioned parallel to the streamwise direction and adjacent to the bottom wall as observed in Figure 5.1. The simulation as previously

mentioned are performed using Nek5000 with ninth order polynomial for spatial discretization and BD/EXT for time discretization. The Courant-Friedrichs Lewy (CFL) number used for the simulations is 0.5, which provides enough stability to the flow.

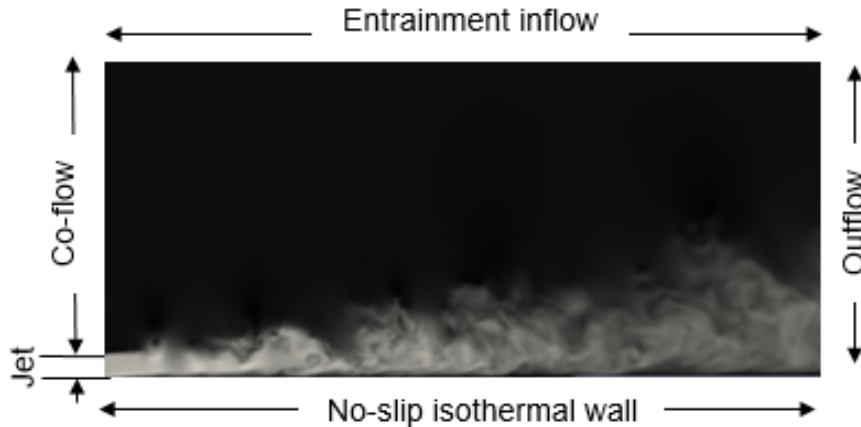


*Figure 5.1* Incompressible Wall-Jet Boundary Conditions.

Transition to turbulence is achieved by the tripping force previously defined in the numerical methods section. This volume force mimics sandpaper in four locations for our case. This four tripping lines are placed between  $2h$  and  $5h$  from the jet inlet, allowing enough sampling space after the flow becomes turbulent. Each tripping line is chosen to be different from each other to increase randomness. The first and third line have a low Fourier mode while the second and fourth have a high Fourier mode which introduces white noise to the previous lines.

### 5.1.1 Inlet and Boundary Conditions

The boundary conditions prescribed for the incompressible wall-jet are presented in Figure. For this case, the inlet Reynolds number is  $Re = 6000$  and the density is  $\rho = 1.225 \text{ kg/m}^3$ . The inlet height,  $h$ , is considered to be  $8 \text{ mm}$ . Above the jet inlet, a

co-flow of 7.5% of the inlet velocity is prescribed to endure the exit of large vortical structures. The top boundary is taken as an entrainment inflow, which means it points downwards at a velocity equal to 2% or 5% of the inlet velocity depending on the section of the study. The sides of the cuboid are taken as periodic boundaries. The outflow is treated as open to the environment, however to warrant the exit of large eddies to the environment the outflow needs boundary treatment. Nek5000 has a subroutine dedicated to avoid back pressure at the outlet, this subroutine treats the boundary as a suction line that avoids instability in the flow. Taking into account the repercussions of this treatment, the sampling for this case is taken at least  $10h$  away from the outlet. The bottom is considered as a no-slip wall where  $u = v = w = 0$ .

The wall boundary is flat and smooth, except at the roughness section, with no-slip condition to include viscous effects and shear stresses in the study. At the bottom wall, the no-slip isothermal condition is fulfilled for the velocity such that  $u = v = 0$ . At the top of the domain, an inflow velocity of 2.6% of the jet inlet is applied to account for entrainment. Table 5.1 gives a comprehensive summary of the boundary conditions and cases used for this study. The study aims to compare the effects of two different frequencies as well as different wave amplitudes with the baseline to observe effects over turbulence phenomena. From this point on, Case 1 is defined as low-Sr case while Case 2 is defined as high-Sr case. In Case 1 and Case 2, a sine wave is added to the inlet velocity as a controlled perturbation, the form of the sine wave is described in Equation 5.2.

$$U_{pert} = 1 + A(\sin(2\pi ft)) \quad (5.2)$$



where  $A$  is the amplitude of the wave,  $y$  is the normal position,  $f$  is frequency, and  $t$  represent the time.

Table 5.1

*Incompressible Case Study Description*

	Baseline			Case 1 (Low Sr)				Case 2 (High Sr)			
<b>Strouhal Number (Sr)</b>	0	0	0	0.0048	0.0048	0.0048	0.0048	0.02	0.02	0.02	0.02
<b>Frequency [Hz]</b>	0	0	0	12	12	12	12	50	50	50	50
<b>Velocity Range m/s</b>	20	20	20	18-22	16-24	12-28	12-28	18-22	16-24	12-28	12-28
<b>Resolution</b>	Low	Low	High	Low	Low	Low	High	Low	Low	Low	High
<b>Top- velocity (% of <math>U_{in}</math>)</b>	2 %	5%	5%	2%	5%	5%	5%	2%	5%	5%	5%
<b>Co-flow (% of <math>U_{in}</math>)</b>						7.5%					

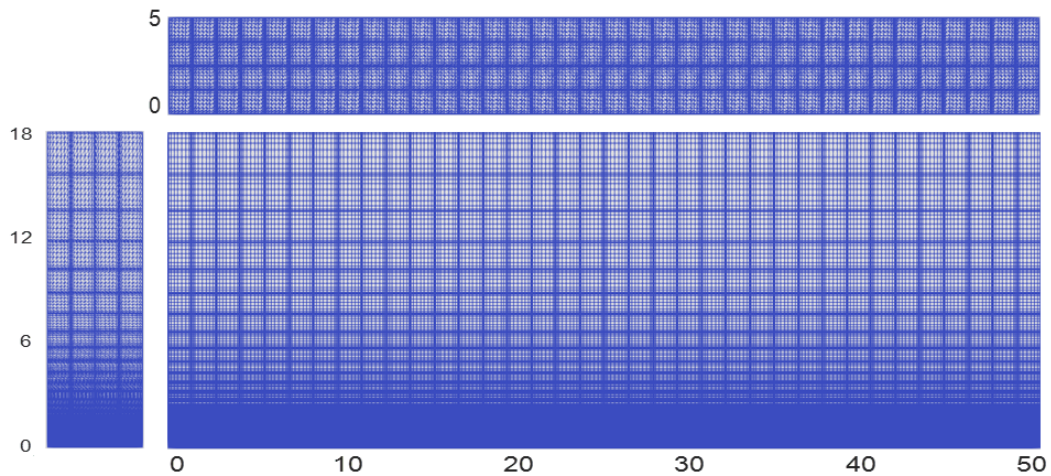


Figure 5.2 High resolution mesh with  $E_x = 30 \times E_y = 30 \times E_z = 4$ .

The first section is a refinement study is performed utilizing low resolution mesh with  $30 \times 24 \times 4$  resulting in a total count of  $\sim 2.09M$ . This resolution compared the baseline and low Strouhal number case with 2% of entertainment velocity. For statistical analysis, the refinement study showed lack of wall-normal elements; hence, a new low resolution

case is defined as well a high resolution case to capture all scales of turbulence. The remaining cases that used the second low resolution mesh were performed with  $24 \times 26 \times 5$  resulting in a total count of  $\sim 2.27M$  degrees of freedom. The high resolution mesh seen in Figure 5.2 was performed with  $30 \times 30 \times 4$  resulting in a total count of  $\sim 2.67M$  degrees of freedom. Notice that between the low and high resolution grids the emphasis on element count changes, after analysis the low resolution shows less number of elements were needed on the spanwise direction and more in the streamwise and normal direction in order to capture the small scale motion.

*Table 5.2*

*Incompressible Case - Mesh Description*

	<b>Low</b>	<b>Low</b>	<b>High</b>
$N_x \times N_y \times N_z$	$30 \times 24 \times 4$	$24 \times 26 \times 5$	$30 \times 30 \times 4$
<b>Polynomial order</b>	9	9	9
<b>Gridpoints</b>	$\sim 2.09M$	$\sim 2.27M$	$\sim 2.6M$

This section is divided into three parts. The first one entails an analysis of the low-resolution mesh that is used as a reference to make modifications for the following low and high-resolution grids used in this study. The second part initially compares the updated low-resolution mesh with the high-resolution mesh to characteristic any information that is lost with resolution. Then, mean and turbulent characteristics are analyzed with the high resolution simulations to compare the baseline and the force jet. Finally, the third section presents a qualitative analysis of how the Strouhal number (Sr) and amplitude of the perturbation added at the inlet affect the development of the flow as a whole.

## 5.2 Refinement Study

This section entails the comparison of low-resolution simulations between baseline case and Low-Sr number case. Conclusions are drawn regarding mesh resolution and perturbation parameters which are applied for the next section of the study.

### 5.2.1 Mean Flow Characteristics

The analysis that follows uses the low-resolution mesh with  $\sim 2.09\text{M}$  degrees of freedom. Similarly to the compressible case, this case uses inner and outer scales to analyze the flow characteristics.

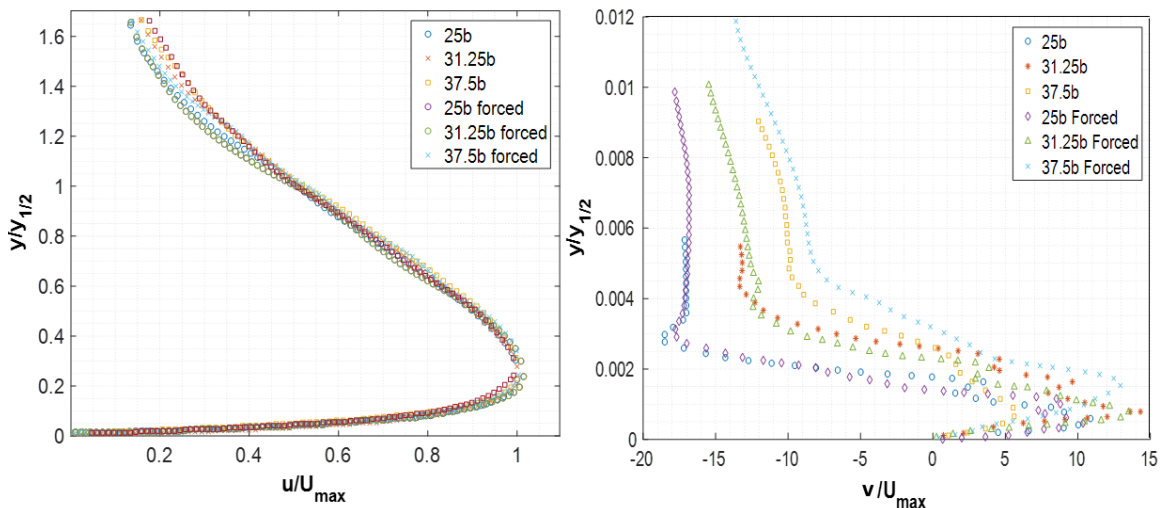
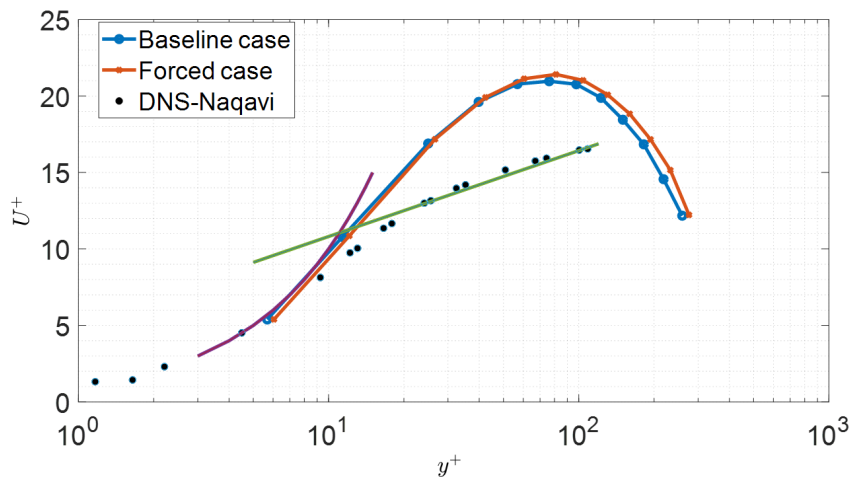


Figure 5.3 Mean streamwise and normal velocity at various streamwise positions ( $x/h = 25, 31.25, 37.5$ ) for the baseline and the forced case ( $Sr = 0.0048$  with  $A = 0.1U_{in}$ ).

Figure 5.3 shows the streamwise and normal mean velocity normalized using conventional outer scaling ( $U_m, y_{1/2}$ ). Measurements are presented for three streamwise positions ( $x/h = 25, 31.25, 37.5$ ) for the baseline case and the low-Sr case ( $f = 12\text{Hz}$  with  $\text{Amplitude} = 0.1U_{in}$ ) referred to as case 1 or forced case for this analysis. The data was compared to Bhatt (2019). The current results for the streamwise mean velocity presents

detachment from the wall at an earlier stage than the experimental data. The normal-mean velocity values do not converge and are not in agreement with previous experimental or computational studies. To improve results in the normal direction resolution needs to increase.



*Figure 5.4* Mean streamwise velocity for the baseline and the force case at  $x/h = 25$ . Data compared with Naqavi et al. (2018).

Figure 5.4 presents the mean streamwise velocity profiles scaled by the friction velocity as a function of wall units. The data is compared with Naqavi et al. (2018). This figure provides information on the grid resolution deficiencies as it magnifies the view of the mean streamwise velocity in the near-wall region. In the vicinity of the wall few points are entering the viscous layer. Notice the points presented in the graph represent the elements defined by the user, but there exist ghost points in between the cells. The outer layer does not converge within the logarithmic region, which presents a problem in the normal resolution.

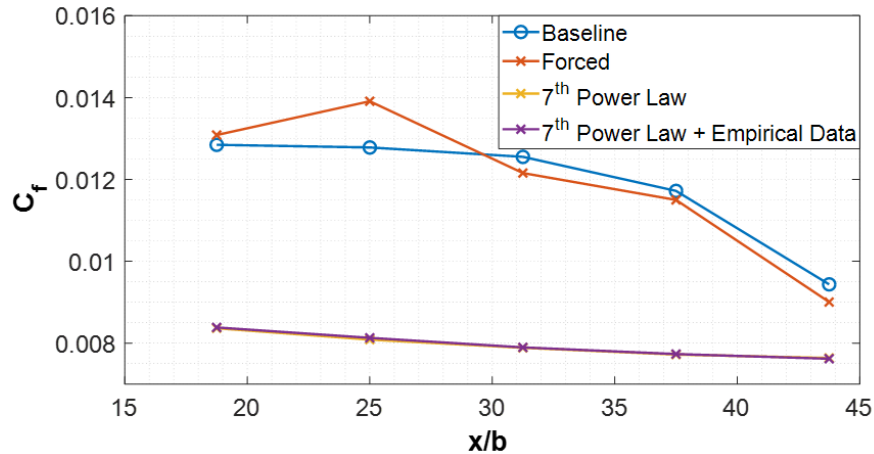


Figure 5.5 Skin friction coefficient as a function of the local streamwise position. Data is compared to the conventional 7<sup>th</sup> power law and the 7<sup>th</sup> power law with empirical data.

Figure 5.5 shows the skin friction coefficient as the local streamwise position. The coefficient is calculated such that  $C_f = 2\left(\frac{u_\tau}{U_{max}}\right)^2$ . The skin friction coefficient confirms again that the normal direction requires higher resolution. The figure shows there is an offset between the current results and the 7<sup>th</sup> power law which the coefficient of friction should follow.

The decay of the mean streamwise velocity is presented in Figure 5.6. Compared to Tang et al. (2015), George et al. (2000) and Barenblatt et al. (2005), the current results find good agreement with the power-law exponent given by Tang et al. (2015). The power law equation is given by Equation 4.4. The amplitude  $A_m$  does not match with the power-law provided, but it remains between the range of 3.55 and 5.15. These results from the baseline and the forced case show that the streamwise resolution is appropriate to obtain convergence in the results.

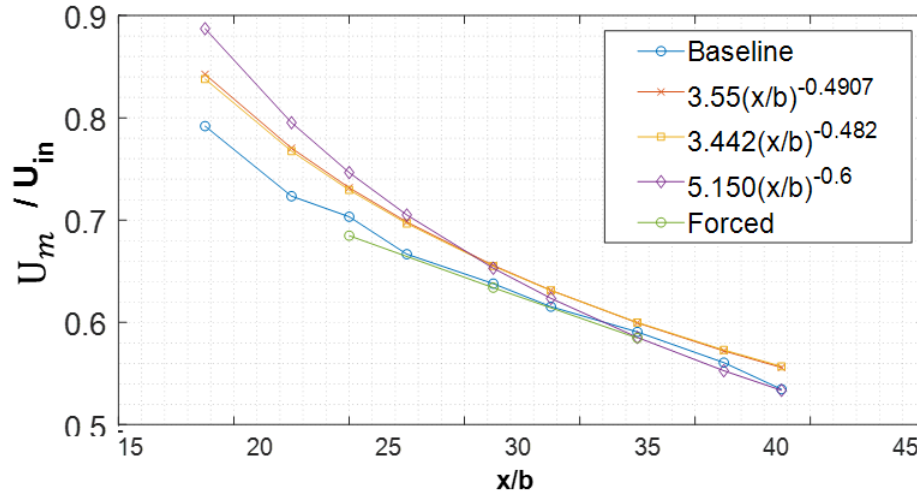


Figure 5.6 Decay of maximum mean streamwise velocity as a function of the streamwise position normalized by the inlet height. Data compared to Tang et al. (2015) orange line, George et al. (2000) purple line, and Barenblatt et al. (2005) yellow line.

## 5.2.2 Turbulent Statistics

Figure 5.7 shows the root mean squared (RMS) of the normal velocity fluctuations and the turbulent kinetic energy scaled by the inlet velocity and by the slot height. The profiles are analyzed at  $x/h = 25$ . The streamwise fluctuations present the characteristic peaks for the inner and the outer layer, notice the inner peak tends to be smaller than the outer peak. The profiles agree on shape with results presented at Bhatt (2019), but the range for the current results is shortened. The turbulent intensity is used as a benchmark to identify if the amplitude of the perturbation is causing a significant effect on the flow development. When comparing the baseline case with the forced case, slight changes are noticed. First the streamwise and wall-normal fluctuations appear to be damped by the perturbation, while in the spanwise direction the fluctuations have slightly higher values than the baseline.

The total turbulent kinetic energy compiles the effects of all the normal fluctuations and shows that the forced case fluctuations are damped in the inner region and the outer region the peak is slightly higher but after the peak, the values are comparable to the baseline. These results for an amplitude of 10 % of the inlet velocity does not show a significant change in the flow development which leads us to increase the amplitude of the perturbation for the following simulations to clearly observe the effect of pulsing the inlet jet.

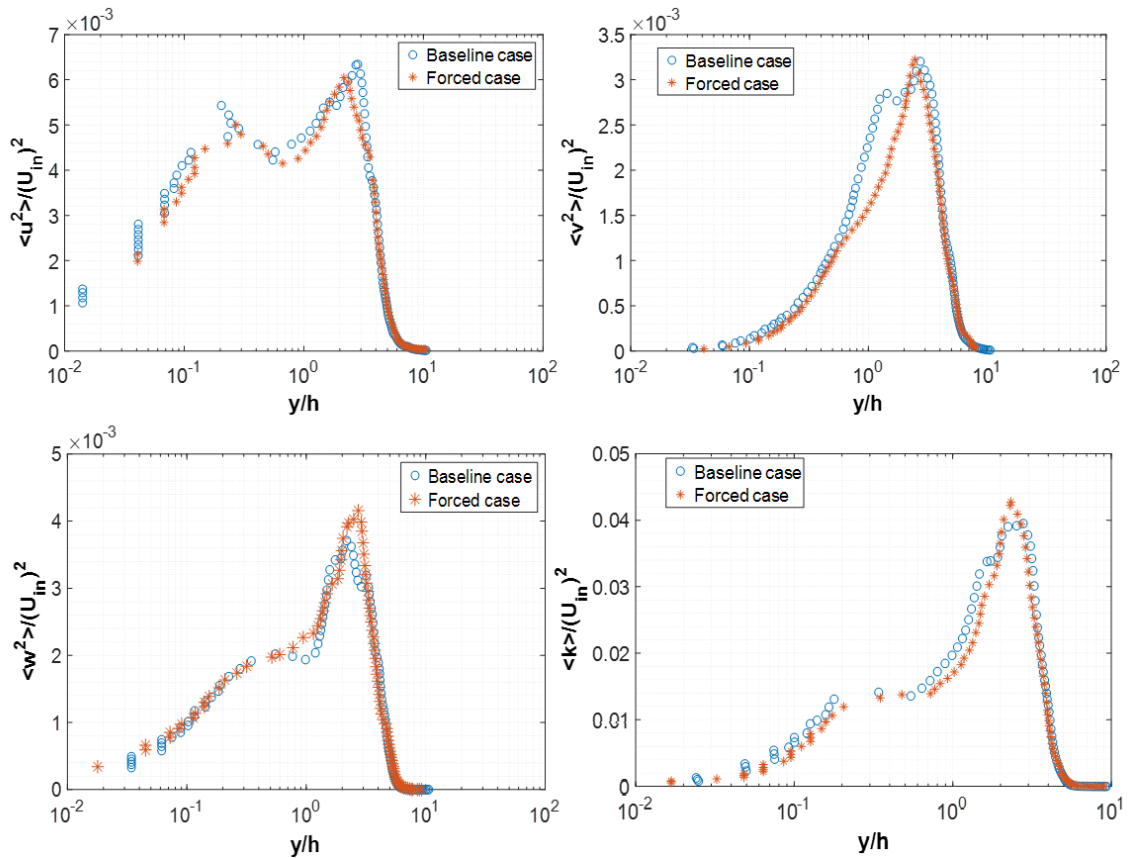


Figure 5.7 Reynolds stresses and turbulent kinetic energy profiles scaled with outer parameters. a. streamwise  $\langle u'u' \rangle$  - b. wall-normal  $\langle v'v' \rangle$  - c. spanwise  $\langle w'w' \rangle$  and d. turbulent kinetic energy  $\langle k' \rangle$ .

According to Schober and Fernholz (2000) effects on skin friction and mixing are obtain at amplitudes larger than 20% of the jet inlet velocity. The low-resolution analysis leads to changes in the mesh resolution and boundary conditions. For the next section, the top boundary condition increases from 2%  $U_{in}$  to 5%  $U_{in}$  for all the grids. The updated low resolution decreases on steamwise element count but increases on normal and spanwise element count.

### 5.3 Detailed Statistical Analysis

The goal in this section is to capture all the scales on the normal direction and to visualize turbulent structures like hairpins in the spanwise direction. The high-resolution mesh keeps the steamwise and spanwise element count but increases grid-points in the normal direction. The following section compared the new computational domains to endorse the possibility of using a low-resolution grid solved with a high order numerical method to study wall-jet. To reduce computational cost, the following grids are interpolated from the low resolution case enabling stability on the flow.

#### 5.3.1 Instantaneous Velocity Characteristics

Figure 5.8 shows a snapshot of the instantaneous streamwise velocity in an XY plane for the baseline and case 1 ( $Sr = 0.0048$  with  $A = 0.4U_{in}$ ). Snapshots are taken at  $t = 0.0504s$ . The low resolution and high-resolution results are compared to visually determine the effects of resolution in flow development. The results from the low-resolution grid appear flatter than for the high -resolution grid. The high-resolution grid shows more in detail the evolution of the Kelvin-Helmholtz instabilities, where the shear layer structure is formed and initially detach from the wall and then reattach as



traveling downstream. The fully developed region of the jet shows a higher amount of large structures in the high-resolution grid as more scales are interacting with each other and causing chaotic behavior. The forced case for both low and high resolution shows less thickness in the overall flow development. This is associated with the changing energy supply caused by the variation of the velocity at the inlet. For all cases, the flow transition regime is observed between 0.05 and 0.1. However, in the following snapshots, the higher resolution cases tend to become fully developed at a further downstream position.

Figure 5.9 shows a snapshot of the instantaneous velocity in an XZ plane for the baseline and case 1. Figures are taken at  $y^+ \sim 7$ . In this region, elongated streamwise streaks, characteristic of boundary layers, are present. These snapshots allow us to observe the behavior of the inner region. At the inlet, the flow transitions from laminar to the transitional regime. The development of KHI is visualized as long strips in the span-wise direction. As the instabilities interact with each other and with the vortices produced by the friction with the wall, turbulent spots are observed between 0.1 and 0.15 for the low resolution. The flow becomes fully turbulent at early state for the low-resolution grid. As the grid increases on resolution, the flow becomes more stable and the flow fully developed region is observed further downstream for the high-resolution cases.

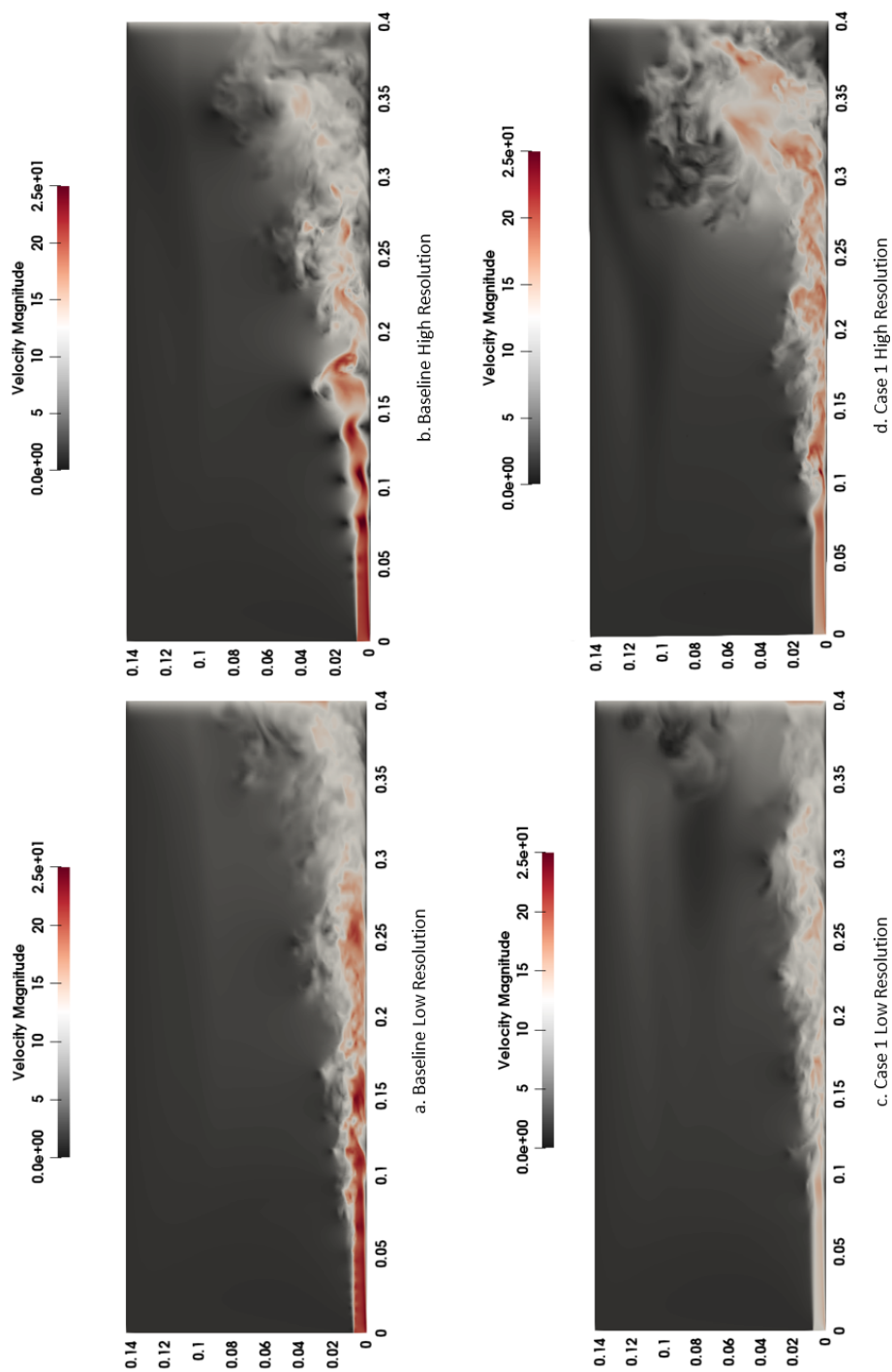


Figure 5.8 Instantaneous velocity in an xy plane at  $t = 0.0504s$ . Figures at the left present results for low resolution grid, and figures at the right presents results for high resolution grid.

Figure 5.10 shows a snapshot of the instantaneous velocity in an ZY plane for the baseline and case 1. Snapshots are taken at two stream-wise locations  $x/h = 30$  and  $x/h = 40$ . The captures at different stream-wise positions provide information on the development of the flow thickness and the decay of the velocity. Comparing both positions shows that the scale of the flow structures grows significantly downstream, in particular in the outer part of the jet. For low-resolution cases, the change is less significant than for the high-resolution case; therefore, the resolution is capturing better the interaction between scales.

To summarize, a low-resolution grid enables an early transition to the turbulent regime where the turbulent statistical analysis is performed and large scale interaction is observed. Despite, the flatness observed in the low-resolution cases, they are a good reference to initially analyze different parameters for wall-jet turbulence manipulation.

A higher resolution grid captures in more detail small scales in the vicinity of the wall; however, the flow becomes fully turbulent further downstream which points to the need of a longer computational domain in the streamwise direction if self-similarity is not achieved.

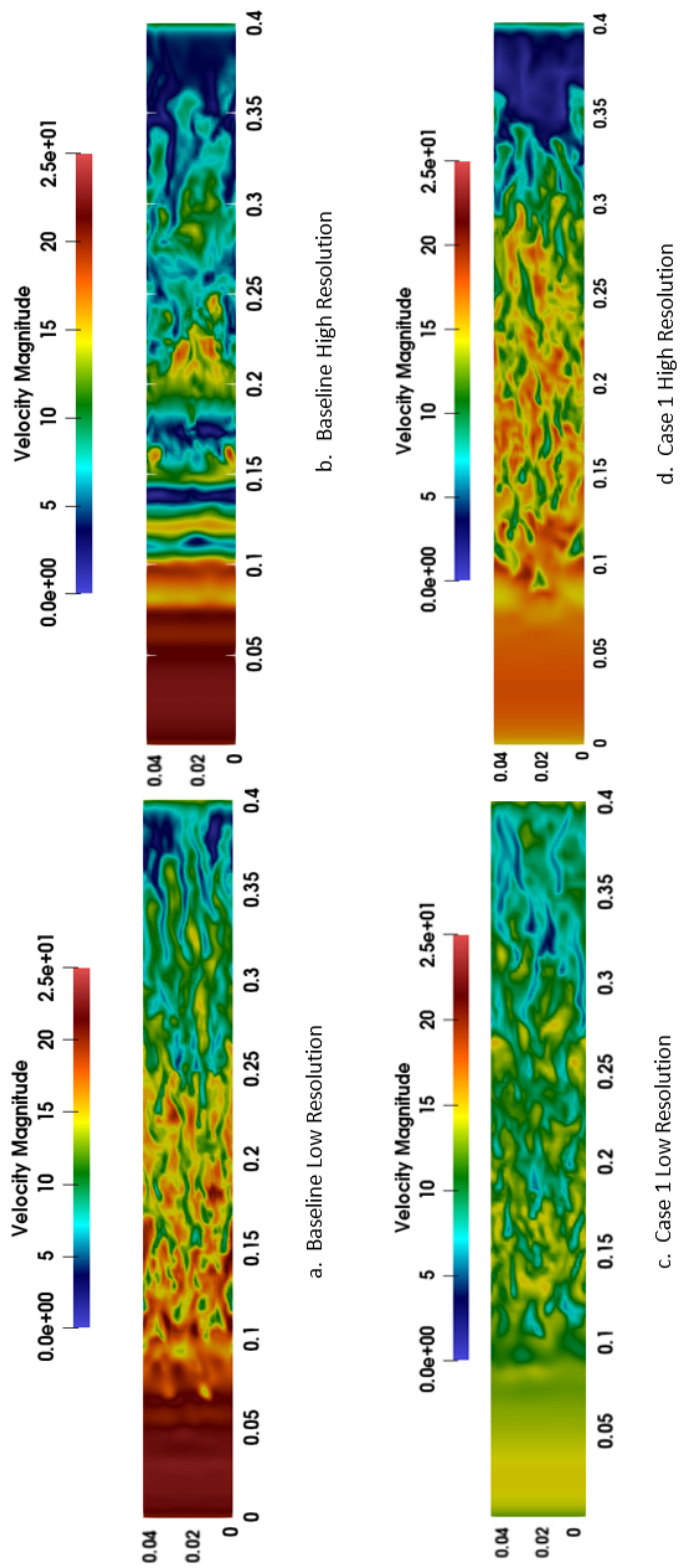


Figure 5.9 Instantaneous velocity in an  $xz$  plane at  $t = 0.0504s$ . Figures are taken at  $y^+ \sim 7$ . Left figures present results for low resolution grid, and right figures presents results for high resolution grid.

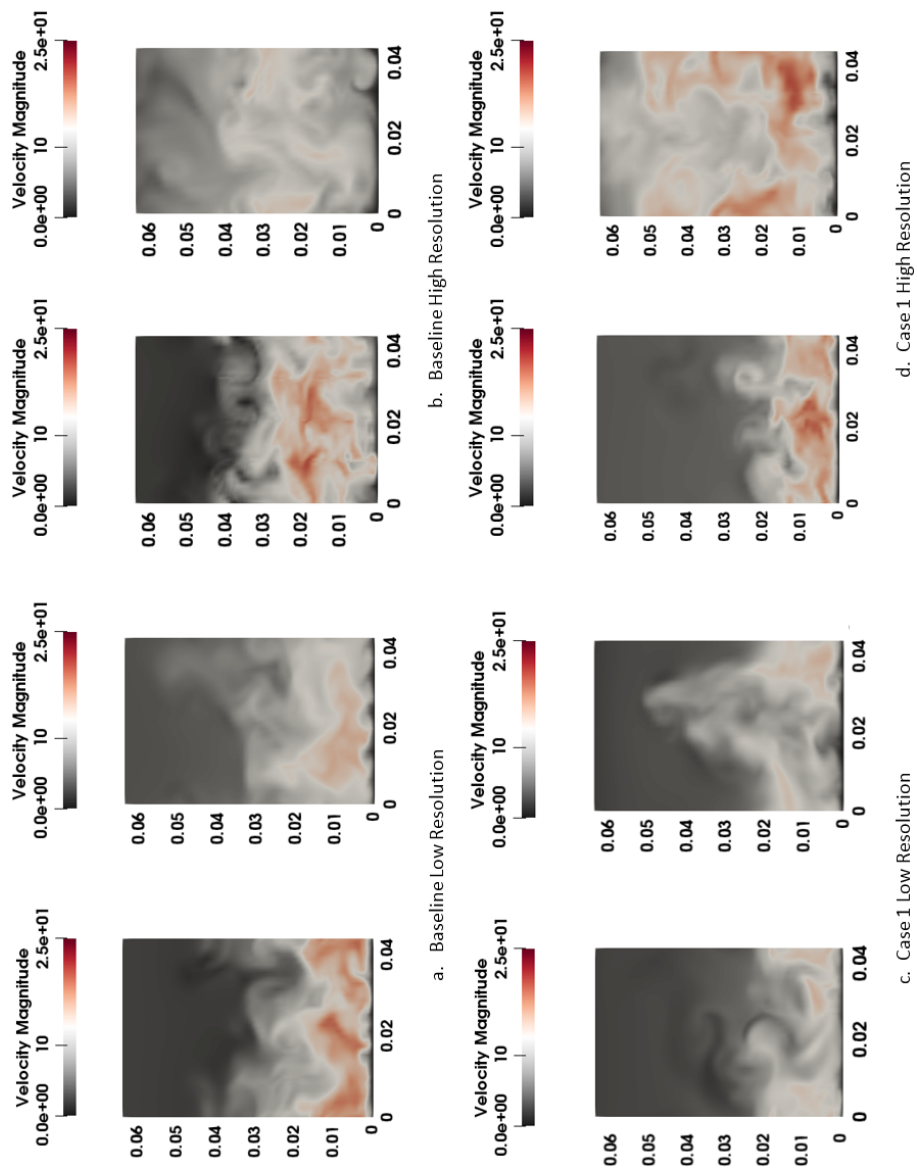


Figure 5.10 Instantaneous velocity in an  $xz$  plane at  $t = 0.0504s$  at two positions  $x/h = 30$  and  $x/h = 40$ . Left figures show results for low resolution grid, and right figures show results for high resolution grid.

### 5.3.2 Mean Flow Characteristics

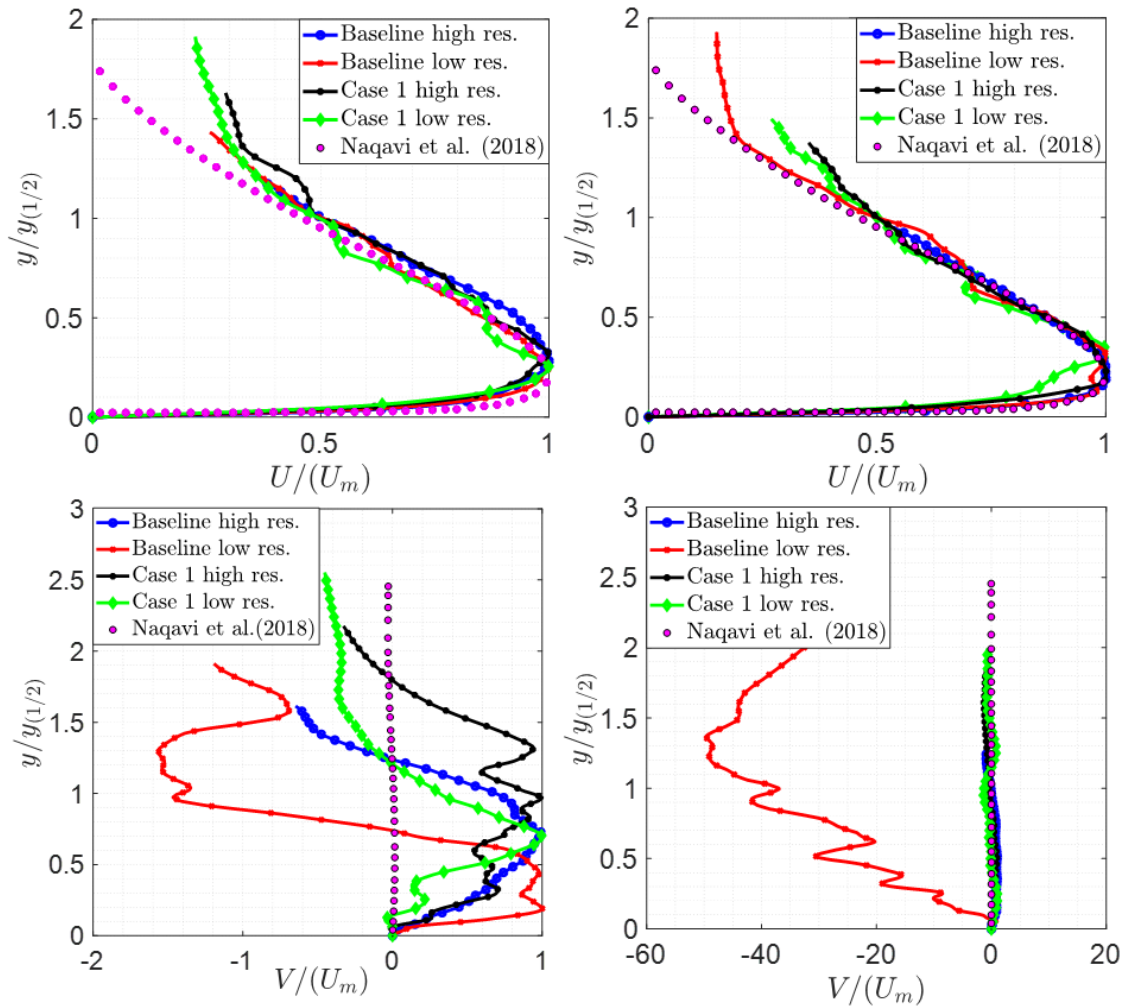
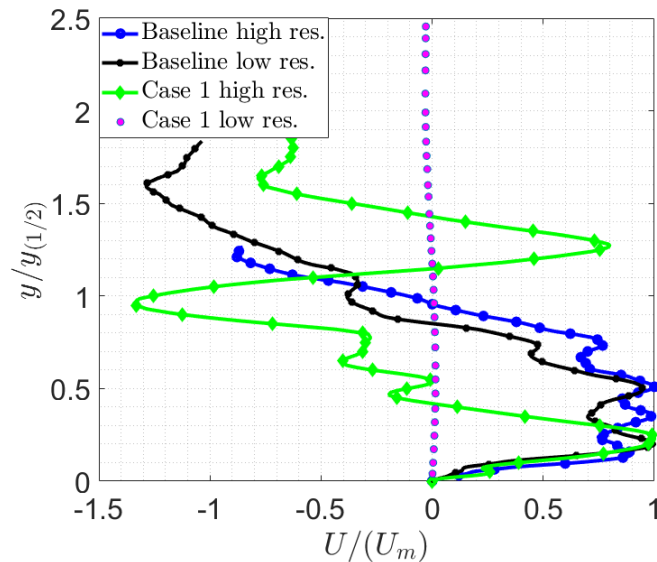


Figure 5.11 Mean stream-wise and normal velocity at positions  $x/h = 30$  and  $35$ , left and right figures respectively. For the baseline and the forced case ( $f = 12Hz$  with  $Amplitude = 0.4U_{in}$ ) the low resolution and high resolution grids are compared with Naqavi et al. (2018).

Figure 5.11 shows the mean stream-wise velocity scaled with outer parameter at  $x/h = 30$  and  $35$ . Recall that the outer parameters are the local maximum streamwise velocity  $U_m$  and the jet half-width  $y_{1/2}$ . The high-resolution results of the mean velocity profiles converged at  $x/h = 30$ , some discrepancies are observed at  $x/h = 30$  and  $35$  for the low-resolution case. The mean profiles show inconsistency with the conventional wall-jet

profile when compared to Naqavi et al. (2018). The normal mean velocity profiles are not converged at  $x/h = 30$  for any of the cases, higher resolution reaches convergence at  $x/h = 35$ . The baseline low-resolution case does not reach convergence. After analyzing the discrepancies between the high and low-resolution grids, the following statistical analysis is conducted using the high-resolution grid for the baseline and the forced case.



*Figure 5.12* Normal velocity at positions  $x/h = 35$ . For the baseline and the forced case ( $f = 12\text{Hz}$  with  $\text{Amplitude} = 0.4U_{in}$ ) the low resolution and high-resolution grids. Excludes low-resolution baseline for close-up. Data compared with Naqavi et al. (2018).

Figure 5.13 presents the mean stream-wise velocity profiles in a semi-logarithmic form scaled by the friction velocity as a function of wall units. The data is compared with Naqavi et al. (2018), finding good agreement in the inner region. When magnifying in the near-wall region, one observes that the high-resolution grid is capturing all the turbulent scales. The profiles in the viscous region are in agreement with the conventional turbulent boundary layer wall laws. The outer layer does not converge within the logarithmic region. the stretching function emphasizes the inner region close to the wall and the flow

shows small scales are not captured in the outer flow. As the flow travels downstream, the agreement with inner scaling improves.

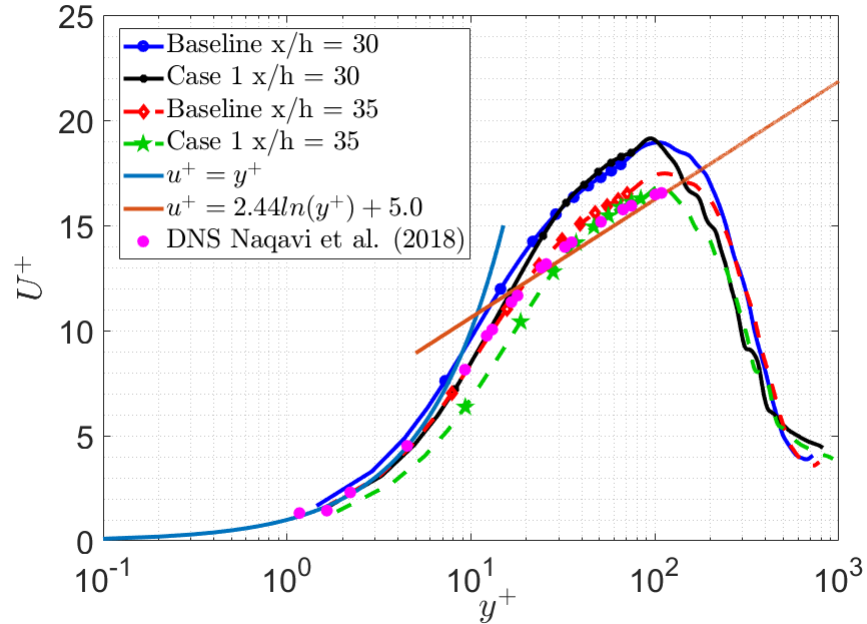


*Figure 5.13* Mean streamwise velocity for the baseline and the force case at  $x/h = 30$  (solid line) and  $x/h = 35$  (dashed line). Data compared with Naqavi et al. (2018) and with conventional scaling functions for turbulent boundary layers.

Figure 5.14 presents the decay of the maximum streamwise velocity as a function of the local position in the streamwise direction. As shown in the YZ snapshots in Figure 5.10 velocity decreases with the streamwise position. The decay is quantified by a power law as presented in Equation 4.1. The constants vary between the baseline and the forced case. The forced case appears to follow the power-law from Banyassady and Piomelli (2014) study, while the baseline case follows the exponential constant for experimental study of Tang et al. (2015) with a slightly lower magnitude for our study,  $A_m = 3.11$ . Notice the forced case differs from the baseline as the decay occurs less rapidly.



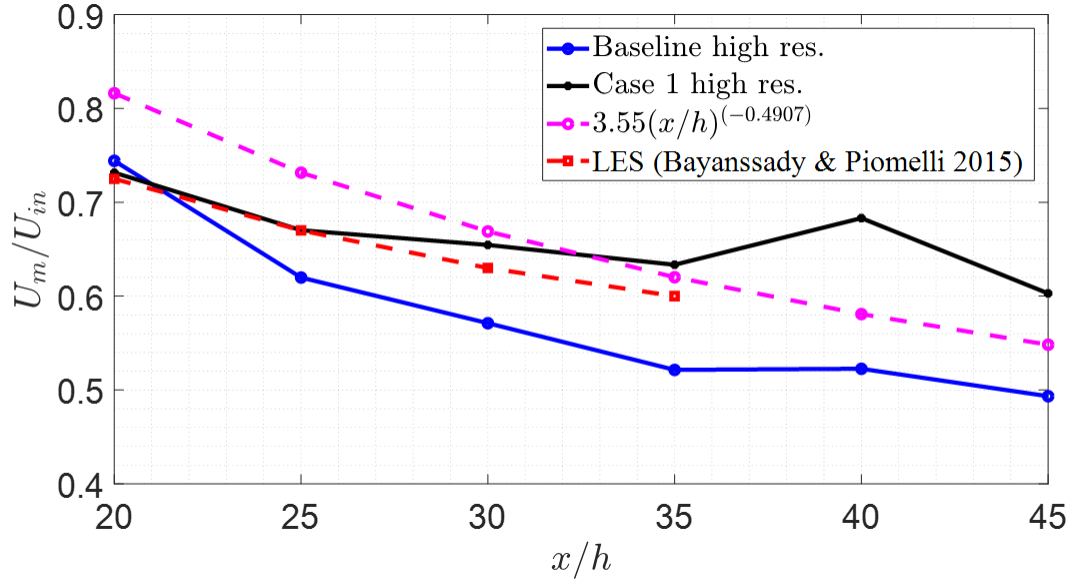


Figure 5.14 Decay of maximum mean streamwise velocity,  $U_m$  as a function of the streamwise position normalized with the inlet height. Data compared to Tang et al. (2015) dashed magenta line and Banyassady and Piomelli (2014) red dashed line.

Figure 5.15 shows the streamwise evolution of the wall-normal location corresponding to the maximum mean streamwise velocity of  $U_m$ . The wall-normal location is quantified by a power law given by equation 4.2. Comparison with Tang et al. (2015) and Naqavi et al. (2018) shows the growth of the wall-normal position is faster for the current results. The baseline case follows the power laws of previous studies with a different virtual origin. The forced shows slower growth of the wall-normal position compared to the baseline, but faster than the presented studies. The exponent that follows the results from the forced case is  $m = 0.88$ . The magnitude is comparable to Naqavi et al. (2018) results  $B_m = 0.040$ .

The jet spreading rate for the inner and the outer regions can be quantified by using a scaling power-law in the function of the inlet height. Equations 5.3 and 5.4 present the power-laws for the outer and the inner region, respectively.

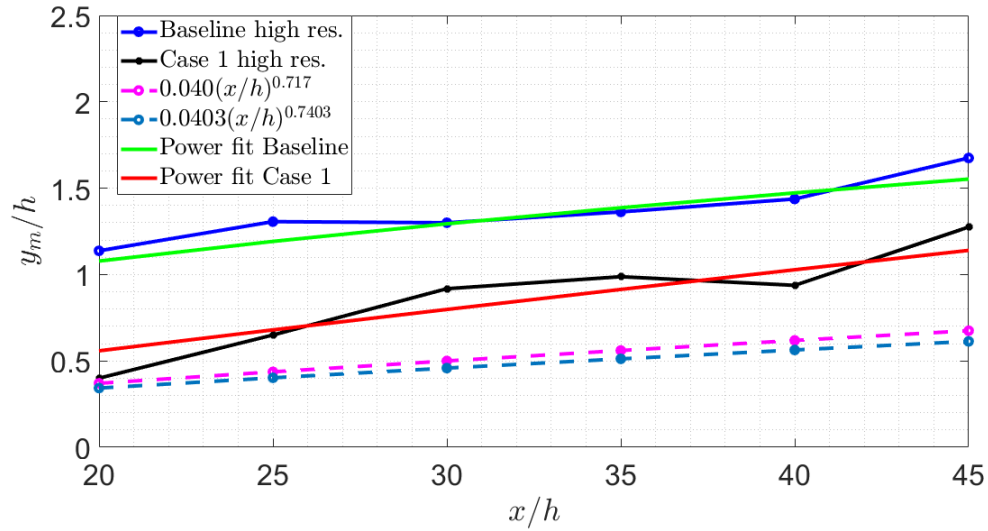


Figure 5.15 Wall-normal position  $y_m$  of the maximum mean streamwise velocity  $U_m$  as a function of the local streamwise position  $x/h$ . Data compared to Tang et al. (2015) green dashed line and Naqavi et al. (2018) red dashed line.

$$\frac{y_{1/2}}{h} = A_o \left(\frac{x}{h}\right)^{\gamma_o} \quad (5.3)$$

$$\frac{y_{1/2(in)}}{h} = A_i \left(\frac{x}{h}\right)^{\gamma_i} \quad (5.4)$$

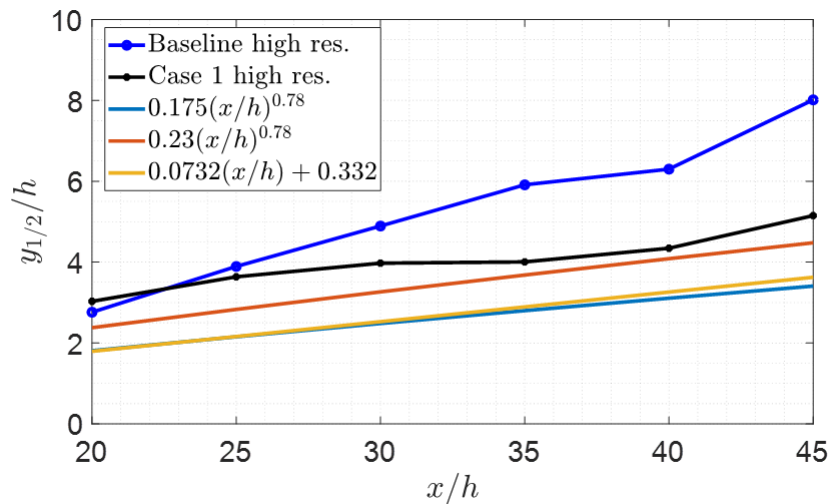


Figure 5.16 Wall jet spreading rate in the outer region. Data compared to Naqavi et al. (2018) blue line, Tang et al. (2015) red line, and Launder and Rodi (1983) yellow line.

Figure 5.16 shows the streamwise evolution of the outer layer half-width. The current results are compared with Naqavi et al. (2018), Tang et al. (2015), and Launder and Rodi (1983). The forced case appears to closely resemble the power-law by Tang et al. (2015) with a small increase in amplitude. The exponent  $\gamma_o$  and the amplitude  $A_o$  for the baseline case are higher than the values presented by previous studies. The amplitude increases by 8% while the exponent takes a value of 0.83. The half-width for the baseline case appears to grow faster than for the forced case.

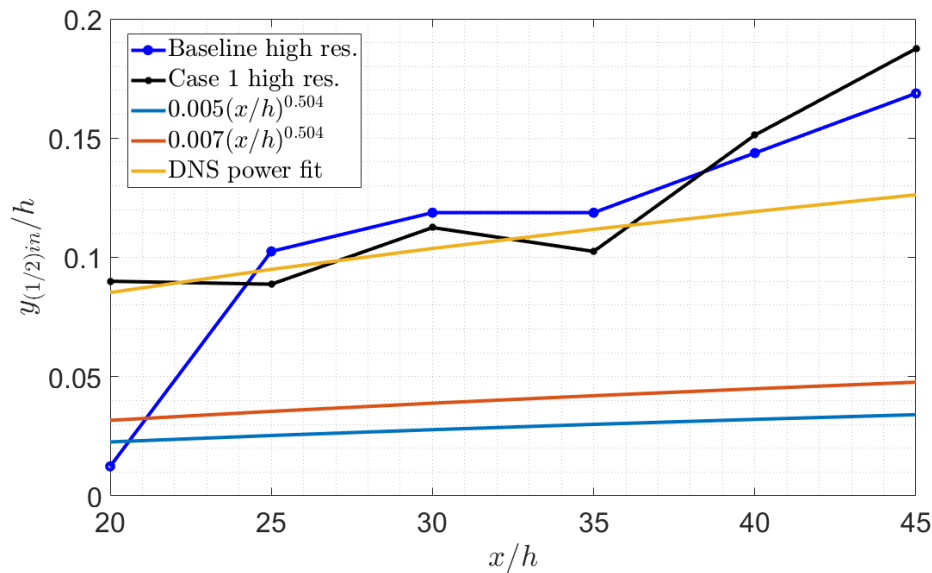


Figure 5.17 Wall jet spreading rate in the inner region. Data compared to Naqavi et al. (2018) blue line, and Tang et al. (2015) red line.

Figure 5.17 shows the streamwise evolution of the inner layer half-width. The current results are compared with Naqavi et al. (2018), and Tang et al. (2015). The power-law amplitude for the baseline and the forced case is higher than the values presented. The values of the power-law fit for the presented results are  $A_i = 0.02$  and  $\gamma_i = 0.504$ . Notice the exponent value is the same as previous studies, but the amplitude changes. The

scattered results do not enable to make a clear comparison between the baseline and the forced case.

Figure 5.18 shows the skin friction coefficient as the local streamwise position normalized by the inlet height. The coefficient is calculated such that  $C_f = 2(\frac{u_\tau}{U_{max}})^2$ . The scattered data show the need for more simulation time to generate more converged results.

The figure shows there is an offset between the current results and the 7<sup>th</sup> power law. Comparing the baseline with the forced case, the perturbation appears to reduce slightly skin friction at positions higher than  $x/h = 30$ .

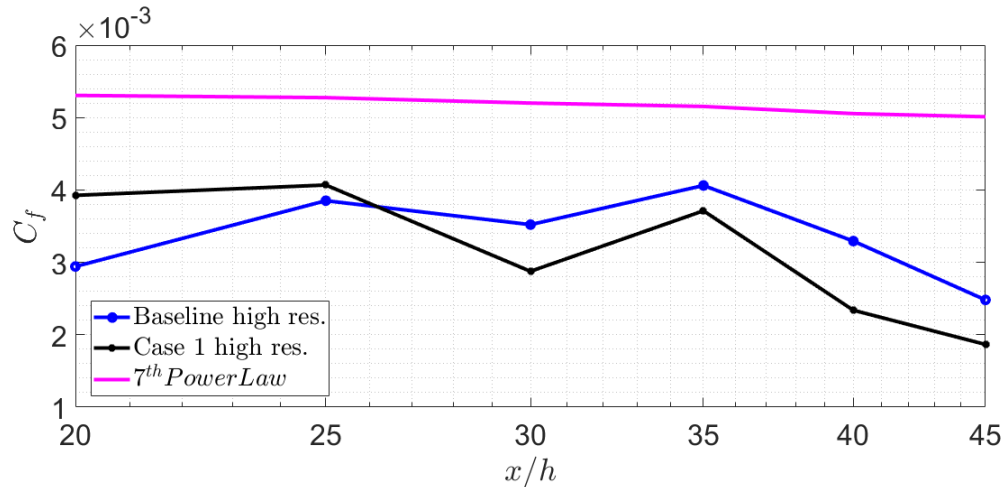


Figure 5.18 Skin friction coefficient as a function of the local streamwise position. Data is compared to the conventional 7<sup>th</sup> power law.

### 5.3.3 Turbulent Statistics

Figure 5.19 shows the root mean squared (RMS) of the normal velocity fluctuations and the turbulent kinetic energy scaled by the maximum local velocity and co-flow velocity  $(U_m - U_c)^2$  and by the half-width  $y_{1/2}$  in the length scale. The profiles are taken at  $x/h = 30$  and  $x/h = 35$ . When comparing the baseline results to previous studies by Naqavi et al. (2018) and Banyassady and Piomelli (2014), the values are smaller in the

streamwise and spanwise direction. The normal direction fluctuations are lower for position  $x/h = 30$  and higher for  $x/h = 35$ . Notice that the inner characteristic peak has a larger range than for previous studies and the magnitude of the outer peak is lower than the inner peak. This could be caused by the entrainment velocity added at the top as a boundary condition. Initially, the velocity was increased to avoid early separation from the wall and following the standard established by Ahlman et al. (2007). The top velocity appears to confine the turbulence fluctuations to the inner region. The fluctuations on the spanwise direction are half the magnitude as the results presented by Naqavi et al. (2018). It is possible that the reduced length on the spanwise direction is changing the turbulence characteristics as the fluctuations might be correlated. The turbulent kinetic energy profiles converge for each case.

Comparing the baseline to the forced case, turbulent fluctuations are weakened in all directions. The turbulent kinetic energy illustrates this point, where one can observe that the total magnitude of the turbulent kinetic energy for the baseline case is approximately 4 times bigger. Hence, the periodic forcing at the inlet is damping turbulence effects. Observing the flow over time shows that the low Strouhal number and high amplitude perturbation delay the transition point to fully developed turbulence. At a high peak of the sine perturbation, a strong supply of energy is introduced in the domain and takes time to travel downstream. At a low peak of the sine, the flow appears to momentarily relaminarize. The combined effect of the high and low peak creates an offset between the pulse and the downstream effect on turbulence. The combination of both effects limits the

development turbulence at downstream positions which will explain the reduction in velocity fluctuations and turbulent kinetic energy.

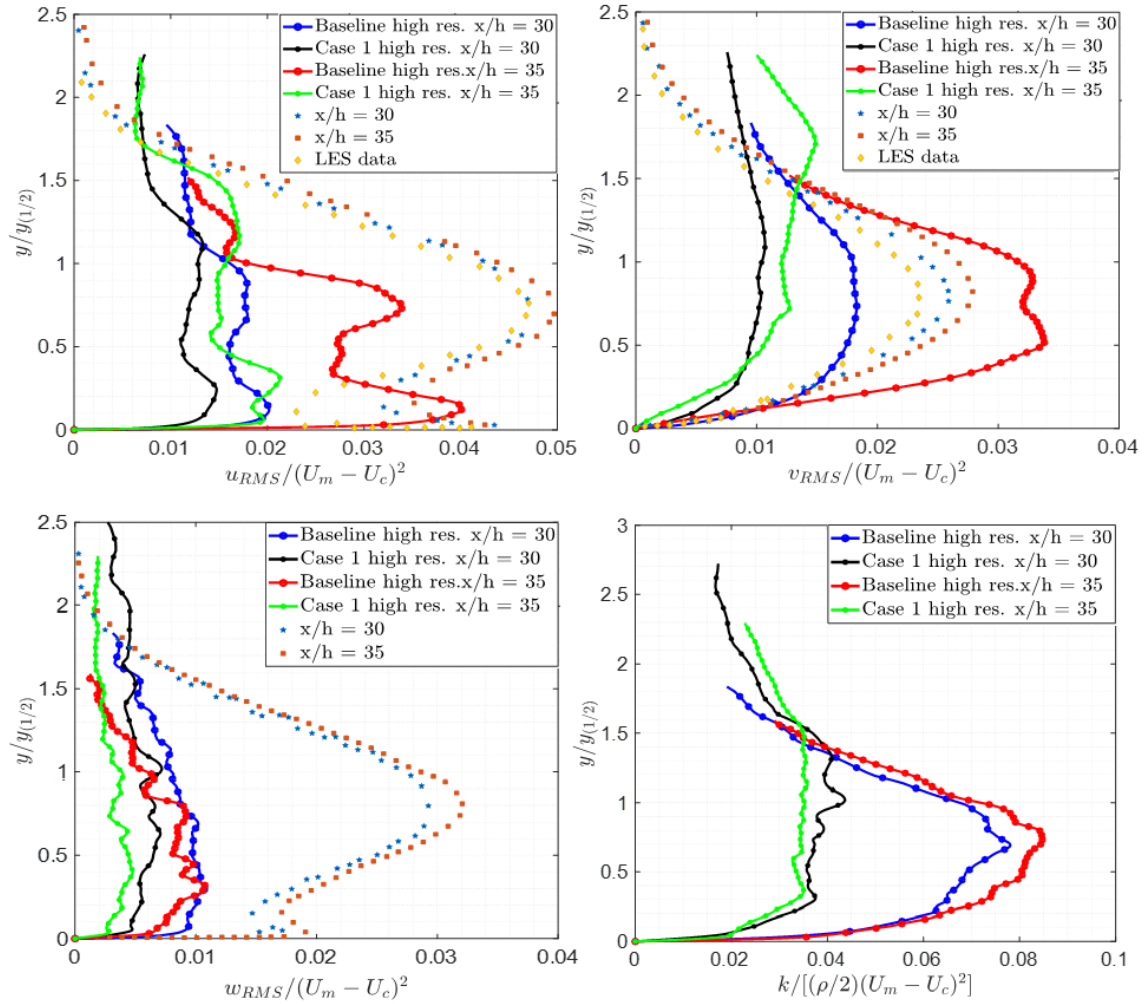


Figure 5.19 Reynolds stresses and turbulent kinetic energy profiles scaled with outer parameters. a. streamwise  $\langle u'u' \rangle$  - b. wall-normal  $\langle v'v' \rangle$  - c. spanwise  $\langle w'w' \rangle$  and d. turbulent kinetic energy  $\langle k' \rangle$ . Data compared to Naqavi et al. (2018) at  $x/h = 30$  (blue  $\star$ ) and  $x/h = 35$  (orange  $\blacksquare$ ) and LES data by Banyassady and Piomelli (2014) (yellow  $\blacklozenge$ ).

Figure 5.20 shows the root mean squared (RMS) of the normal velocity fluctuations and the turbulent kinetic energy scaled by the friction velocity  $u_\tau$  in the velocity scale and by the friction velocity and kinematic viscosity  $u_\tau/\nu$  in the length scale. The profiles are taken at  $x/h = 30$  and  $x/h = 35$ . Data is compared to DNS data by Naqavi et al. (2018)

and LES data by Banyassady and Piomelli (2014). Profiles for the baseline and the forced case converge in the streamwise and wall-normal direction the spanwise direction is not well converged.

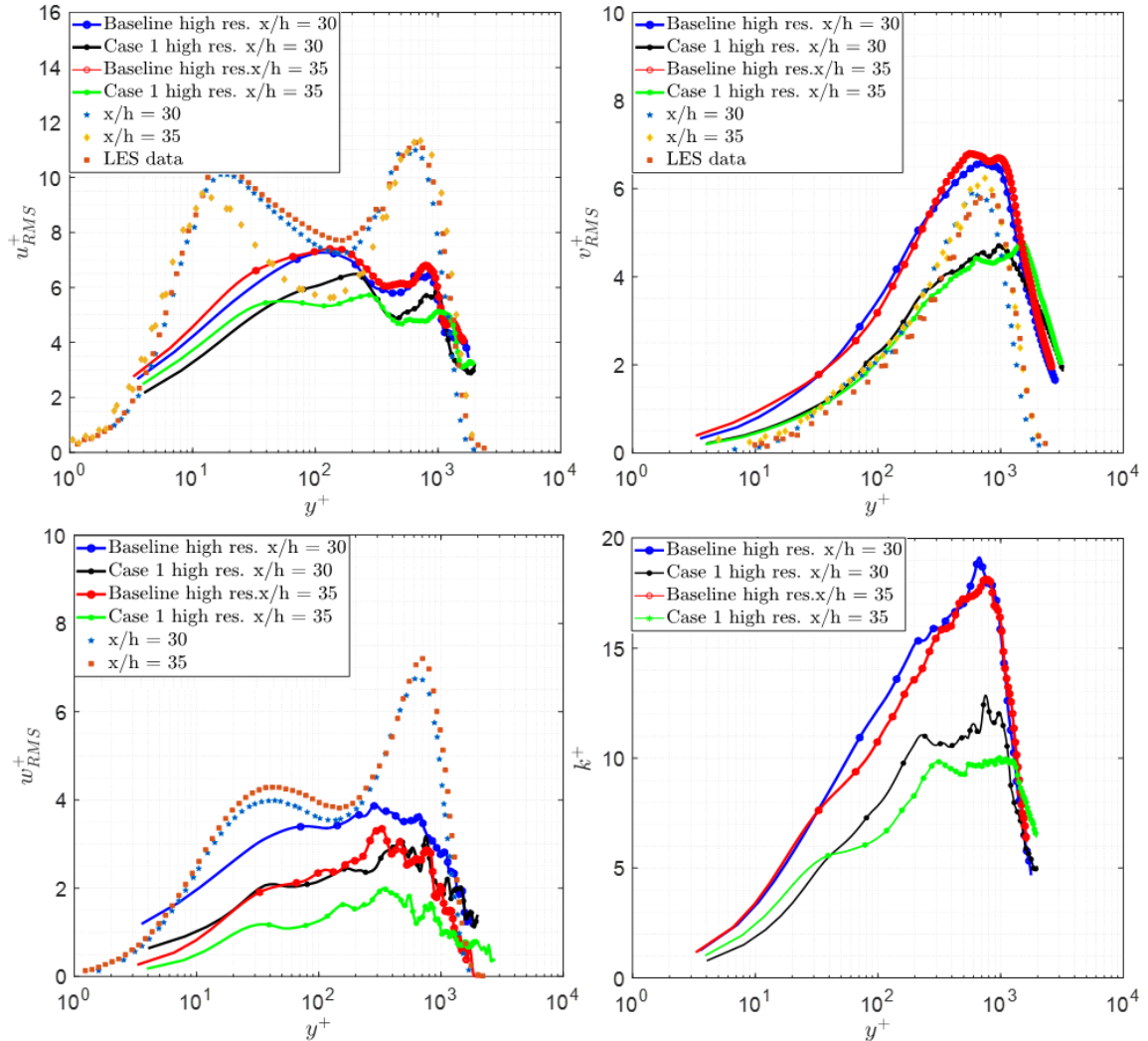


Figure 5.20 Reynolds stresses and turbulent kinetic energy profiles scaled with inner parameters. a. streamwise  $\langle u'u' \rangle$  - b. wall-normal  $\langle v'v' \rangle$  - c. spanwise  $\langle w'w' \rangle$  and d. turbulent kinetic energy  $\langle k' \rangle$ . Data compared to Naqavi et al. (2018) at  $x/h = 30$  (blue  $\star$ ) and  $x/h = 30$  (orange  $\blacksquare$ ) and LES data by Banyassady and Piomelli (2014) (yellow  $\blacklozenge$ ).

The inner scaling shows the baseline presents a wider inner peak between  $y^+ = 100$  and  $y^+ = 300$ . The outer peak range is reduced, as well as its magnitude. The higher

changes are observed at the streamwise and spanwise directions. The normal direction profiles are consistent in shape, but not in magnitude compare to Naqavi et al. (2018) and Bayanssady et al. (2014). The values on the baseline present higher fluctuations in the wall-normal direction. The outer peak in the spanwise direction is not present as values are of comparable magnitude with the inner region. The turbulent kinetic energy profiles appear to converge for the baseline case, but the forced case present discrepancies. Comparing the results between the baseline and forced case, the same reduction of turbulent fluctuation as observed with outer scaling is observed with inner scaling. The inner scaling shows that more significant changes, between the baseline and forced case, are present in the wall-normal direction. This is observable in the turbulent kinetic energy profile as the outer peak of the flow experience a significant reduction in total turbulent energy. The influence of manipulation of the inlet velocity is noticeable in the total kinetic energy profiles.

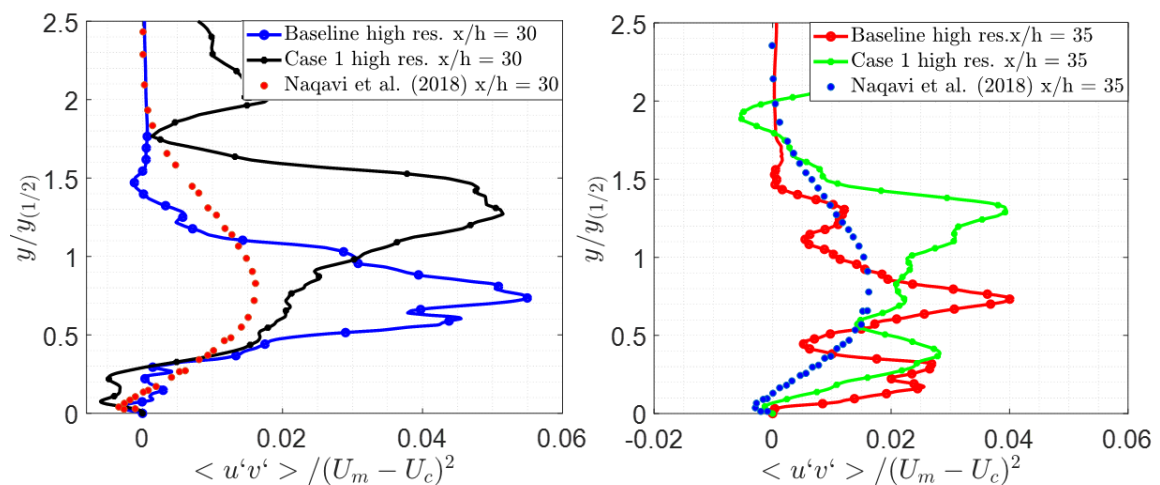


Figure 5.21 Outer scaled Reynolds shear stress profiles at  $x/h = 30$  and  $x/h = 35$ . Data is compared with Naqavi et al. (2018).



Figure 5.21 shows the Reynolds shear stresses scaled by the maximum velocity and co-flow velocity  $(U_m - U_c)^2$  in the velocity scale and by the half-width  $y_{1/2(in)}$  in the length scale. The current data does not have good agreement with Naqavi et al. (2018); however, the shape of the curve is initially attained at  $x/h = 30$ . For the baseline, the peak of the shear stress matches the peak at Naqavi et al. (2018). For the forced case, this peak is shifted to the outer layer. The values at  $x/h = 30$  show an increment of about 50% in magnitude, while at position  $x/h = 35$  the shape is in less accordance but the values are more in numerical range. Reynolds shear stresses do not reach convergence at the further streamwise position; hence, the simulation requires more iterations.

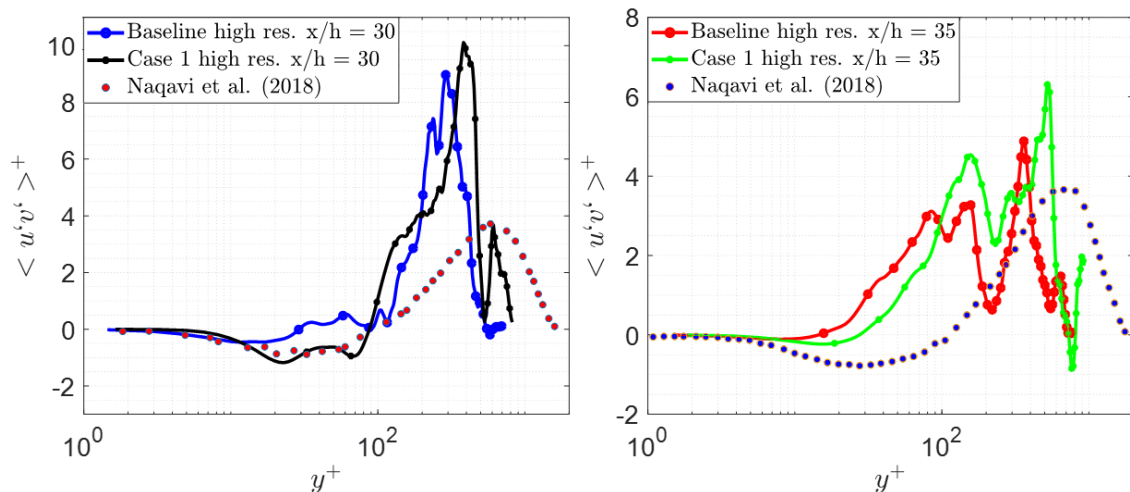


Figure 5.22 Inner scaled Reynolds shear stress profiles at  $x/h = 30$  and  $x/h = 35$ . Data is compared with Naqavi et al. (2018).

Figure 5.22 shows the Reynolds shear stresses scaled by inner parameters, where the convergence of the current data seems to have better agreement with Naqavi et al. (2018). The figure shows disagreements on stress magnitude and peak position. As the flow travels further, the magnitude reaches a better agreement, but the position of the peaks is

still inconsistent with previous data. Notice that the dislocation, where values change sign, observed in the graphs demonstrate the shear-stress transport in the mixing layer region. The main contribution to the shear-stress transport arises from the gradients of triple velocity correlations.

Figure 5.23 presents profiles of triple velocity correlations scale with inner variables. The average of triple velocity relations  $\langle u'u'u' \rangle$ ,  $\langle v'v'v' \rangle$ ,  $\langle u'v'v' \rangle$ , and  $\langle v'u'u' \rangle$  provides limited but significant assessment of the turbulence behavior. The triple correlations are compared with experimental data by Eriksson (2003) and DNS data by Naqavi et al. (2018).

$\langle u'u'u' \rangle$  shows agreement with the compared data mainly in the inner section of the jet for the baseline. The forced case shows a different behavior than the conventional planar wall-jet in shape and value magnitude. A high value is observed at  $\langle u'u'v' \rangle$ , which indicates that fluctuations in the normal direction for the baseline are higher than for previous cases. For the baseline, this relationship shows large stress gain in the inner section, while the forced case presents larger stress transport above  $y^+ = 80$ .

$\langle u'u'u' \rangle$  and  $\langle u'u'v' \rangle$  are related to the turbulent diffusion of the jet.  $\langle u'u'u' \rangle$  has a weak influence on the balance as its gradient takes place on the budget.  $\langle u'u'v' \rangle$  change of sign indicates turbulence exchange between lower and high production region. This characteristic behavior is not present for the current results since the correlation does not change in sign.

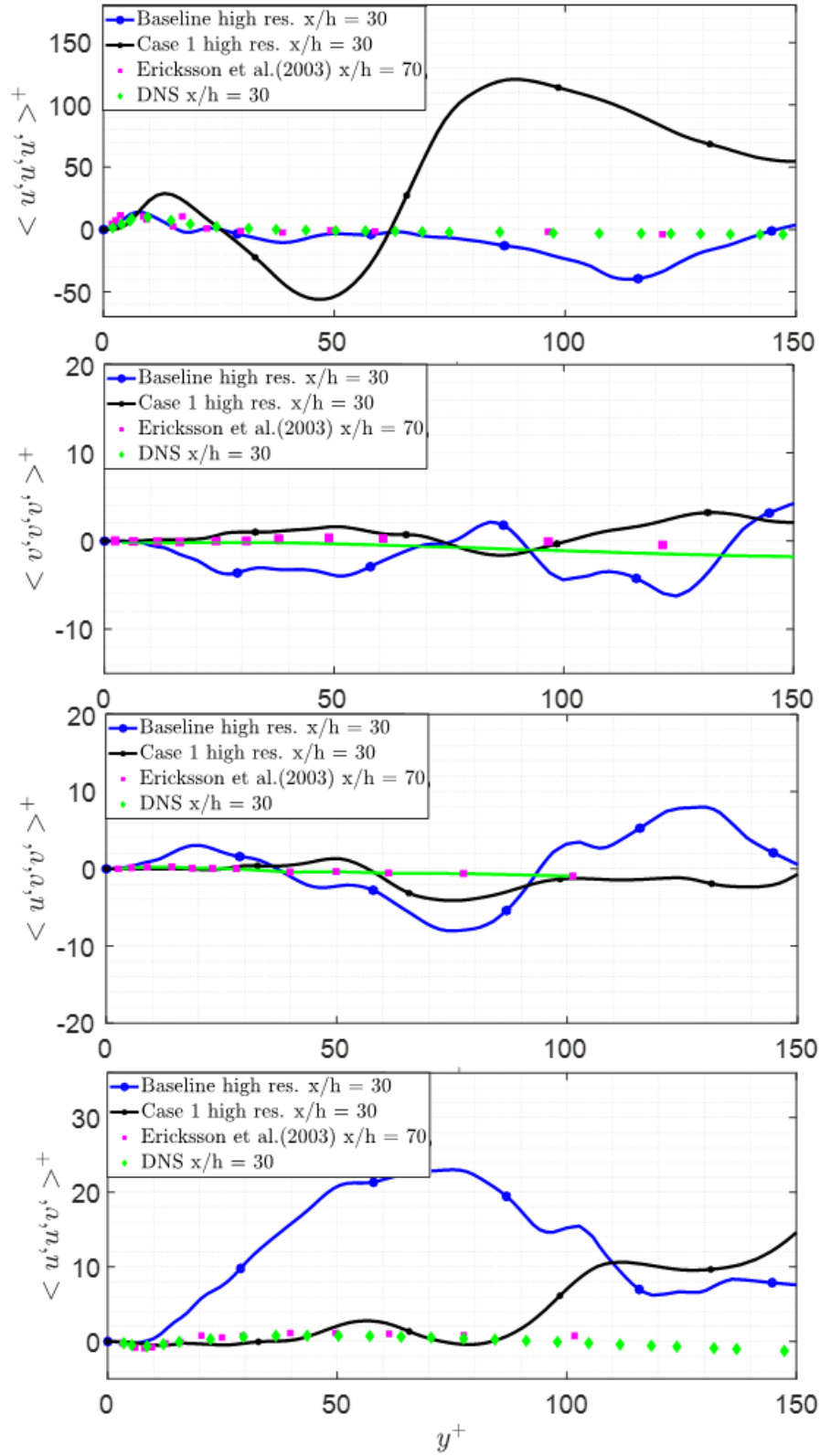


Figure 5.23 Profiles of triple velocity correlations scale with inner variables. Data compared with Ericksson (2003) (magenta), and Naqavi et al. (2018)(green).

The relation in the wall-normal direction  $\langle v'v'v' \rangle$  has lower values for the baseline case than for Naqavi et al. (2018) and Eriksson (2003). The forced case has good agreement with a planar wall-jet compared to the baseline with a rising peak as it further from the wall. For the baseline,  $\langle u'v'v' \rangle$  shows lower values at the inner region and higher values in the outer region when compared to Naqavi et al. (2018).

$\langle v'v'v' \rangle$  and  $\langle u'v'v' \rangle$  are associated with the turbulent transport of the jet.  $\langle v'v'v' \rangle$  indicates the turbulent transport between layers by the change from positive to negative values. The results for this study, present transport between the region closer to the wall for the baseline case and also non-existent for the forced case sustaining the laminarization of the flow.  $\langle u'v'v' \rangle$  represents the transfer of positive shear stress from the outer region to the inner region. For the baseline, this effect seems to appear stronger than for a conventional wall-jet while the forced case follows closely the conventional wall-jet behavior.

#### 5.3.4 Turbulent Structures

Figure 5.24 presents the instantaneous snapshots for the high resolution baseline and the forced case. Visualization is used to qualitatively analyze the flow and to observe turbulent structures being formed. For both cases, vorticity at the outer region is presented. In the baseline case, the shear layer vortices known as pure KHI are seen around  $x/h = 11.5$ . Around the same region, vortices generated by the boundary layer are observed. The interaction and breakdown of these instabilities travel downstream creating large scale turbulent structures in the fully developed region. For the forced case, the transition and laminar region are longer. The first pure KHI is visualized around  $x/h = 15$ .

The interaction of the vortices is confined to the inner region. The wall-jet turbulence is reduced for the forced case.

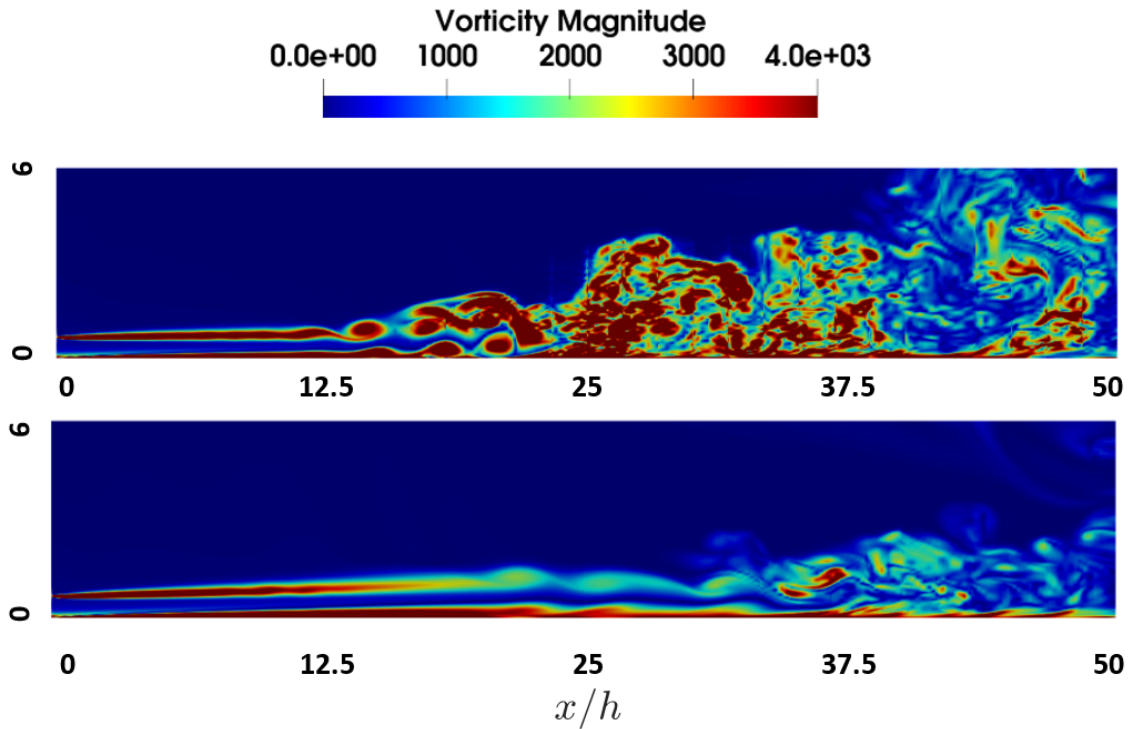
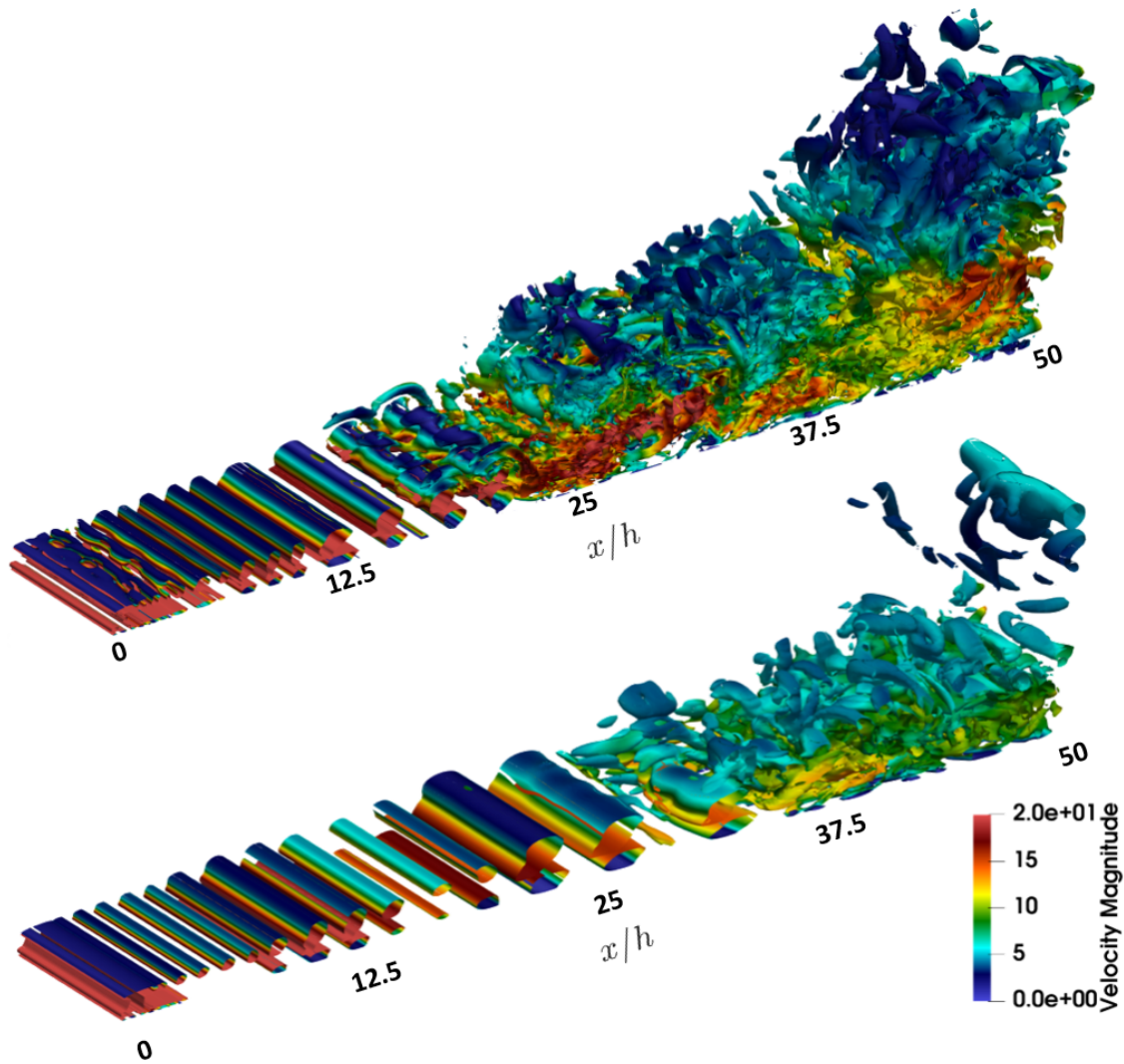


Figure 5.24 Instantaneous vorticity field at  $t = 0.08\text{s}$  of the high resolution baseline (top) and the forced case (bottom).

The Q-criterion is used to visualize turbulent structures on the outer and inner regions of the jet. Figure 5.25 shows the iso-surfaces associated to the Q-criterion for the outer layer of the high-resolution baseline and the forced case. The criterion corresponds to the second invariant of the velocity gradient tensor of the velocity. Near the jet inlet, the shear layer region is observed at  $x/h < 14$  for the baseline and at  $x/h < 25$  for the forced case. This is the billow production region for Kelvin-Helmholtz instabilities (KHI). Around  $x/h = 16$  for the baseline and  $x/h = 25$ , the eddies produced by the shear layer interacted with the billows produced by the boundary layer.



*Figure 5.25* Iso-surfaces associated to the Q-criterion for the outer layer of the baseline (top) and the forced case (bottom). The iso-surfaces are coloured with local velocity magnitude.

These roll structures grew in size as they travel downstream interacting with each other and transforming into a more chaotic and complex flow. When comparing the baseline case with the forced case, one can observe the flow stability increases for the forced case and less large structures are observed in the outer region.

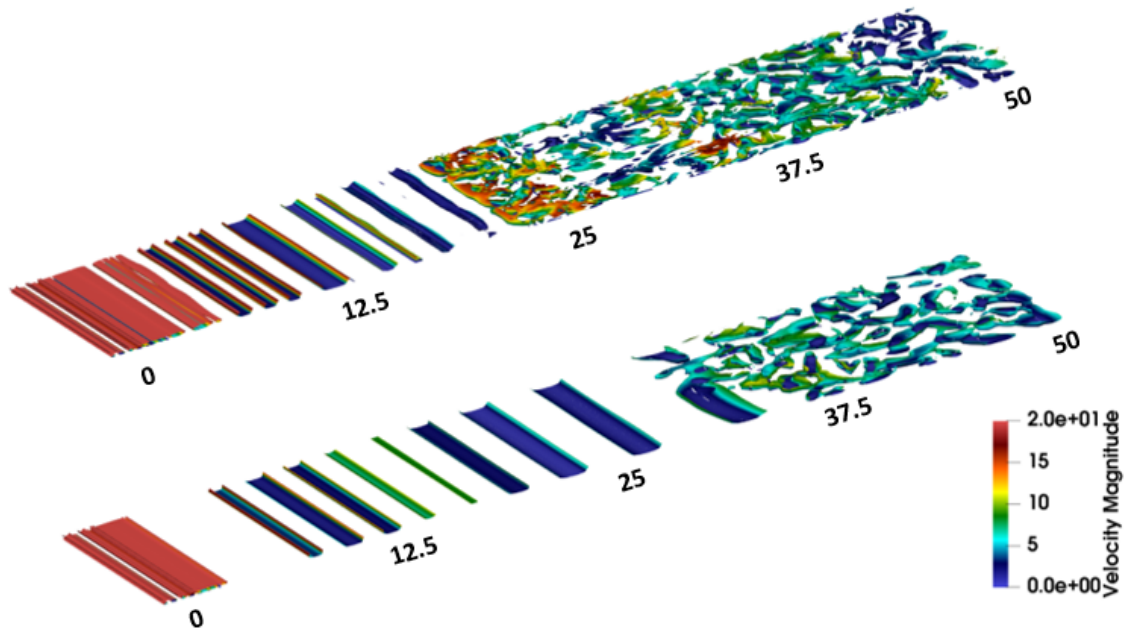


*Figure 5.26* Iso-surfaces associated to the Q-criterion for the inner layer of the baseline (top) and the forced case (bottom). The iso-surfaces are coloured with local velocity magnitude.

Figure 5.26 shows the iso-surfaces associated to the Q-criterion for the inner layer of the high-resolution baseline and the forced case. The slide to observe inner structures is taken at  $y/h = 0.25$ . The inner layer isosurfaces enable the visualization of the transition region. This region expands over the range  $0 < x/h < 20$  for the baseline and  $0 < x/h < 20$  for the forced case. The transition shows discontinuous spaces of turbulence. The observation of a longer transition region made in the previous analysis is visualized using the iso-surfaces. After the transition region, the flow is fully developed. In this region turbulent structures are visualized as align tube structures, which in a two dimensional view will look like long stripes. The forced case shows the later separation from the wall compared to the baseline and less turbulent structures are pictured after the perturbation is introduced in the domain.

#### 5.4 Perturbation Parametric Analysis

The following section presents snapshots of different forced cases where the amplitude and the Strouhal number varied. For figures 5.29, 5.30, 5.27 and 5.28, two  $Sr$  and two magnitudes are used to qualitative analyze the influence in these parameter on the flow development. The Strouhal numbers used are  $Sr = 0.0048$  and  $Sr = 0.02$ , for each Strouhal number ( $Sr$ ) two amplitudes are tested,  $0.2U_{in}$  and  $0.4U_{in}$ . The XY plane is used to analyze the outer region flow development, while the XZ plane is used to analyze the inner region. The following section presents snapshots of different forced cases where the amplitude and the magnitude varied. The simulations presented in this section are performed using the updated low resolution mesh with  $\sim 2.27$  M gridpoints.

Figure 5.27 presents the snapshots at the high peak velocity of each perturbation on the XY plane. At the high peak, the energy supply at the inlet is higher. For the low- $Sr$  case, shows strong vortical structures traveling downstream. The low amplitude case has a less turbulent behavior than the high amplitude case. The high amplitude cases at both frequencies present complex flow at the downstream domain. The high- $Sr$  case at low amplitude looks flatter compared to the low- $Sr$  case, there is not a strong presence of turbulence structures for this case. In the first instance, the low amplitude case appears to develop faster and more turbulent structures are visualized.

Figure 5.28 presents the snapshots at the high peak velocity of each perturbation on the XZ plane. The low- $Sr$  cases at both amplitudes present transition closer to the jet inlet. The roll structures produced by the KHI breakdown at a faster pace compared to the high- $Sr$  case. These cases start with strong velocity magnitude that become lower when



reaching the end of the domain. Note that the cases have not reached a complete fully developed turbulence region for any of the cases. The formation and development of KHI is observed for the high  $Sr$  cases. The low amplitude high- $Sr$  case develops faster than the other cases and turbulence appear to be confined to the inner region. As mentioned previously, this is the strongest turbulent flow present for the low- $Sr$  case. These large turbulent structures entered the domain but due to the low frequency cannot be maintained over time.

As the following figures will illustrated, less turbulent structures at the low peak and strong velocity structures at high peak for the case at  $Sr = 0.02$ . Faster transition and bigger turbulent structures at the low peak and less strong turbulence at the high peak for the case at  $Sr = 0.0048$ . It seems that the high- $Sr$  develops turbulence when the supply energy is low at the inlet while the low- $Sr$  case does the opposite. To illustrate this point, snapshots at a low peak in the perturbation are presented in Figures 5.29 and 5.30.

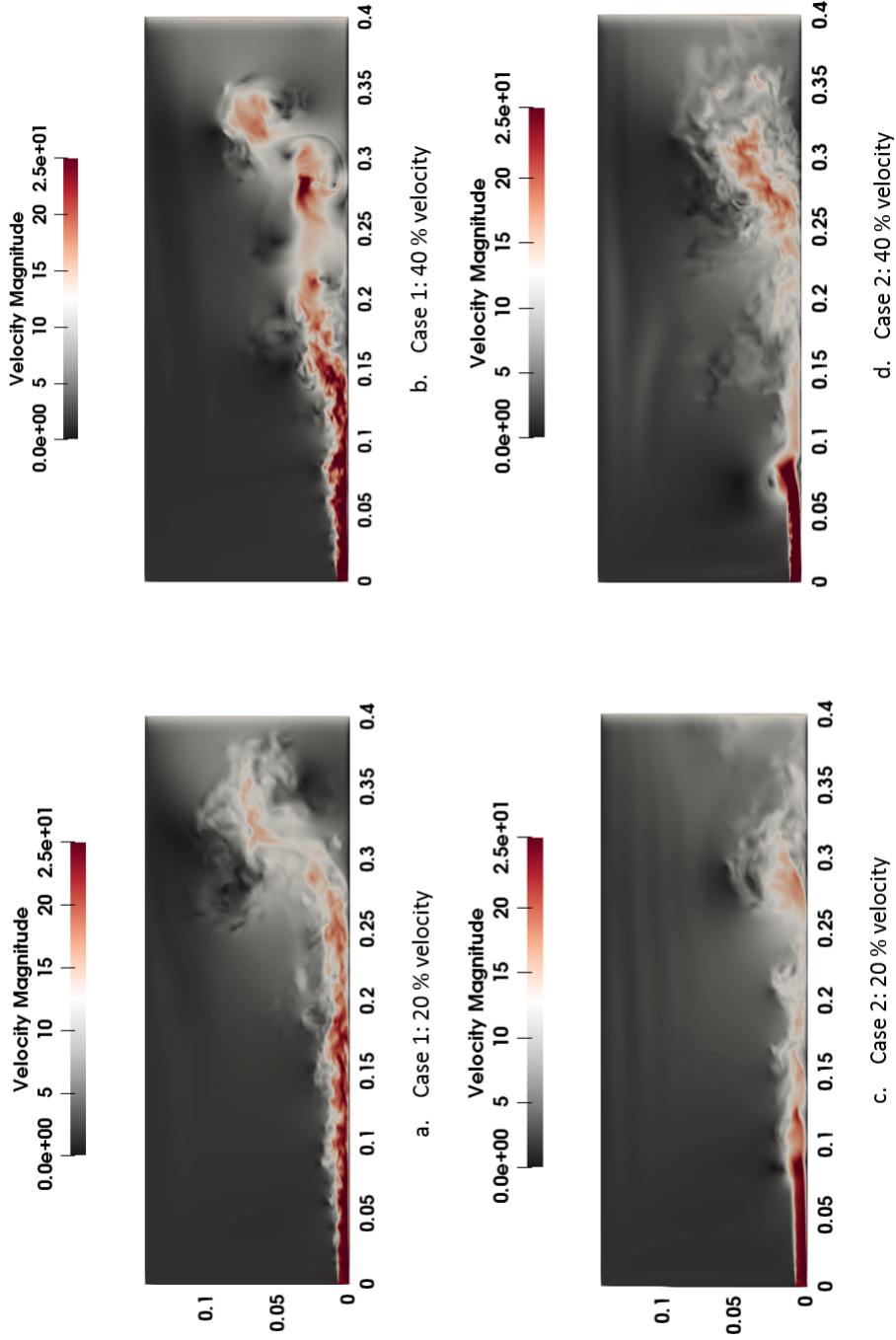


Figure 5.27 Instantaneous velocity in an xy plane at the high peak velocity. Figures at the top present results for  $f = 12\text{Hz}$  at  $20\%U_{in}$  (left) and  $40\%U_{in}$  (right), and figures at the bottom presents results for  $f = 50\text{Hz}$  at  $20\%U_{in}$  (left) and  $40\%U_{in}$  (right).

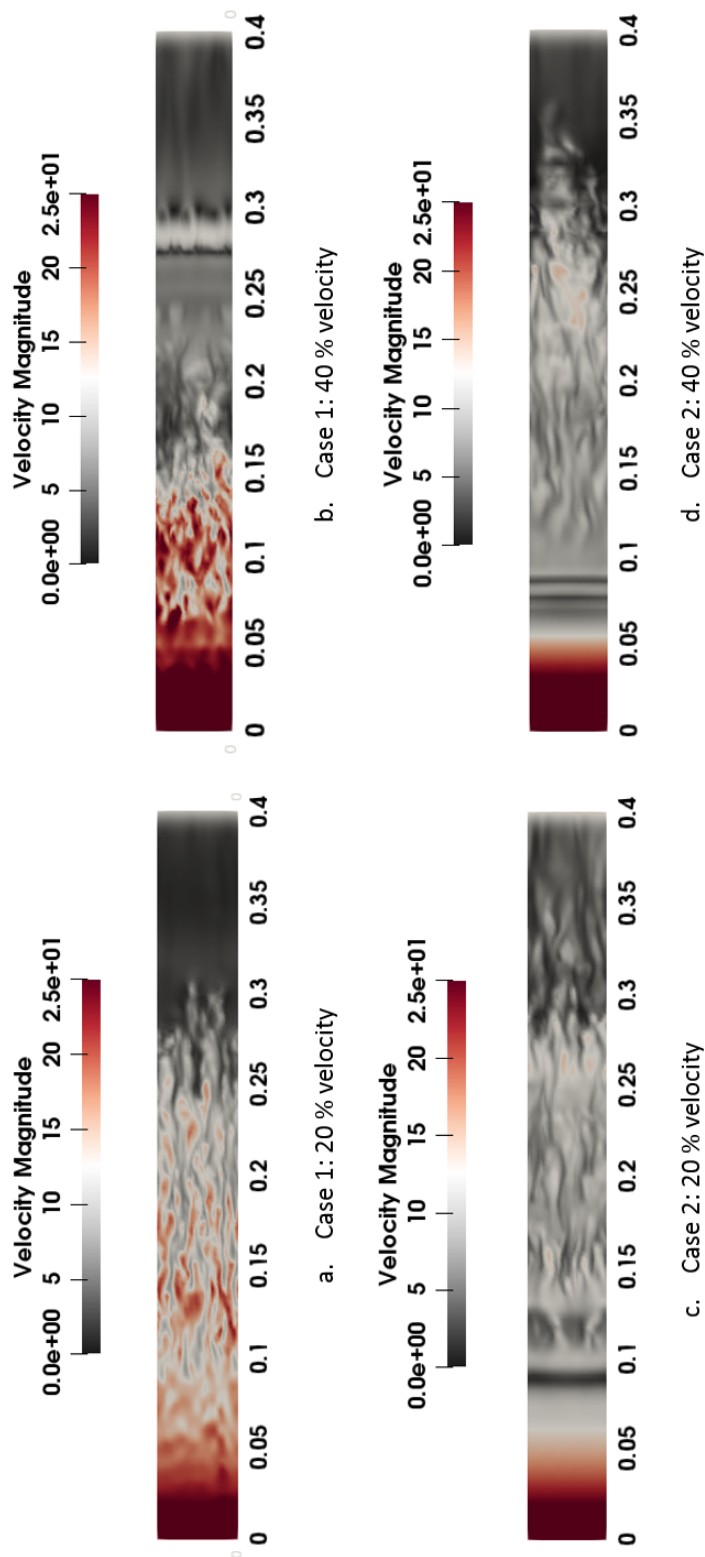


Figure 5.28 Instantaneous velocity in an  $zy$  plane at the high peak velocity. Figures at the top present results for  $f = 12\text{Hz}$  at  $20\%U_{in}$  (left) and  $40\%U_{in}$  (right), and figures at the bottom presents results for  $f = 50\text{Hz}$  at  $20\%U_{in}$  (left) and  $40\%U_{in}$  (right).

Figure 5.29 presents the snapshots at the low peak velocity of each perturbation on the XY plane. The change of  $Sr$  between  $Sr = 0.0048$  and  $Sr = 0.02$  appears to transition the flow at an earlier downstream position for  $f = 50Hz$  for both amplitudes. The velocity shows larger values on the high- $Sr$  case. The low amplitude high- $Sr$  case shows high-velocity structures interacting between each other and traveling downstream. At high amplitude, the structures are not as strong, but the vortex is bigger in size. Besides, we observe spacing between the developed flow and the new vortex. The low- $Sr$  case shows a more stable behavior for both amplitudes. At high amplitude, this case shows less strength in the velocity. The high- $Sr$  case presents more interesting behavior in term of turbulence. Notice the large turbulent structure turns and interacts with the upcoming inflow maintaining a chaotic and complex behavior in the flow.

Figure 5.30 presents the snapshots at the low peak velocity of each perturbation on the XZ plane. The inner region behavior is observed for all four cases. The inner region confirms the transition occurs closer to the jet inlet. The KHI formation is more noticeable in the high- $Sr$  cases. The long strips, characteristic of the turbulent boundary layer, are observed at all amplitudes and frequencies. These structures show a more consistent behavior for the low- $Sr$  case. On the low- $Sr$  case, the velocity remains low within the domain, while for the high- $Sr$  case the velocity ranges from high to low. At the turbulent spots and the beginning of the fully developed region, the velocity is at its higher magnitude for the high- $Sr$  case. the spacing between structures is appreciable in this plane. In the high- $Sr$  case, a high-velocity region is followed by a low-velocity region that will translate in a detachment from the wall.

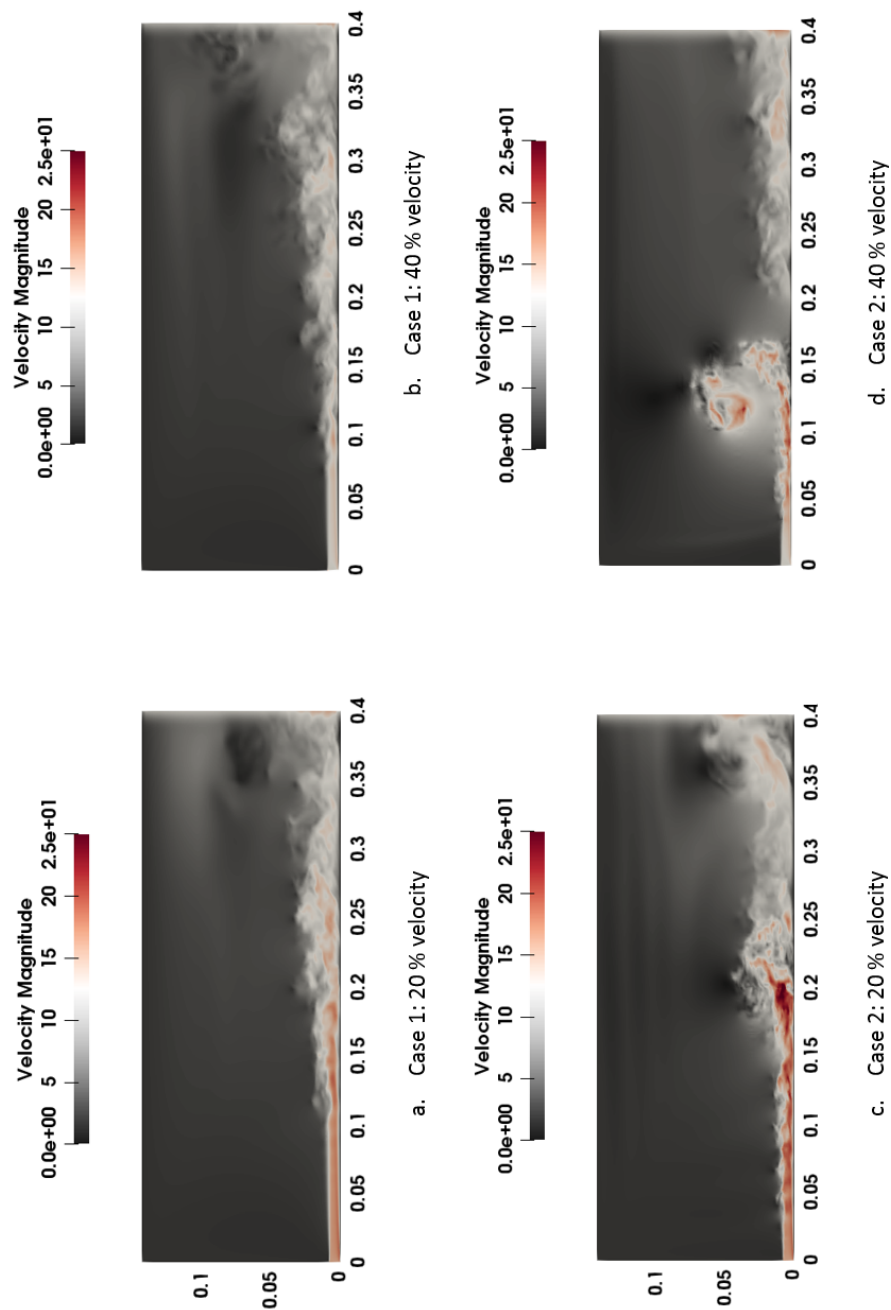


Figure 5.29 Instantaneous velocity in an  $xy$  plane at the low peak velocity. Figures at the top present results for  $f = 12Hz$  at  $20\%U_{in}$  (left) and  $40\%U_{in}$  (right), and figures at the bottom presents results for  $f = 50Hz$  at  $20\%U_{in}$  (left) and  $40\%U_{in}$  (right).

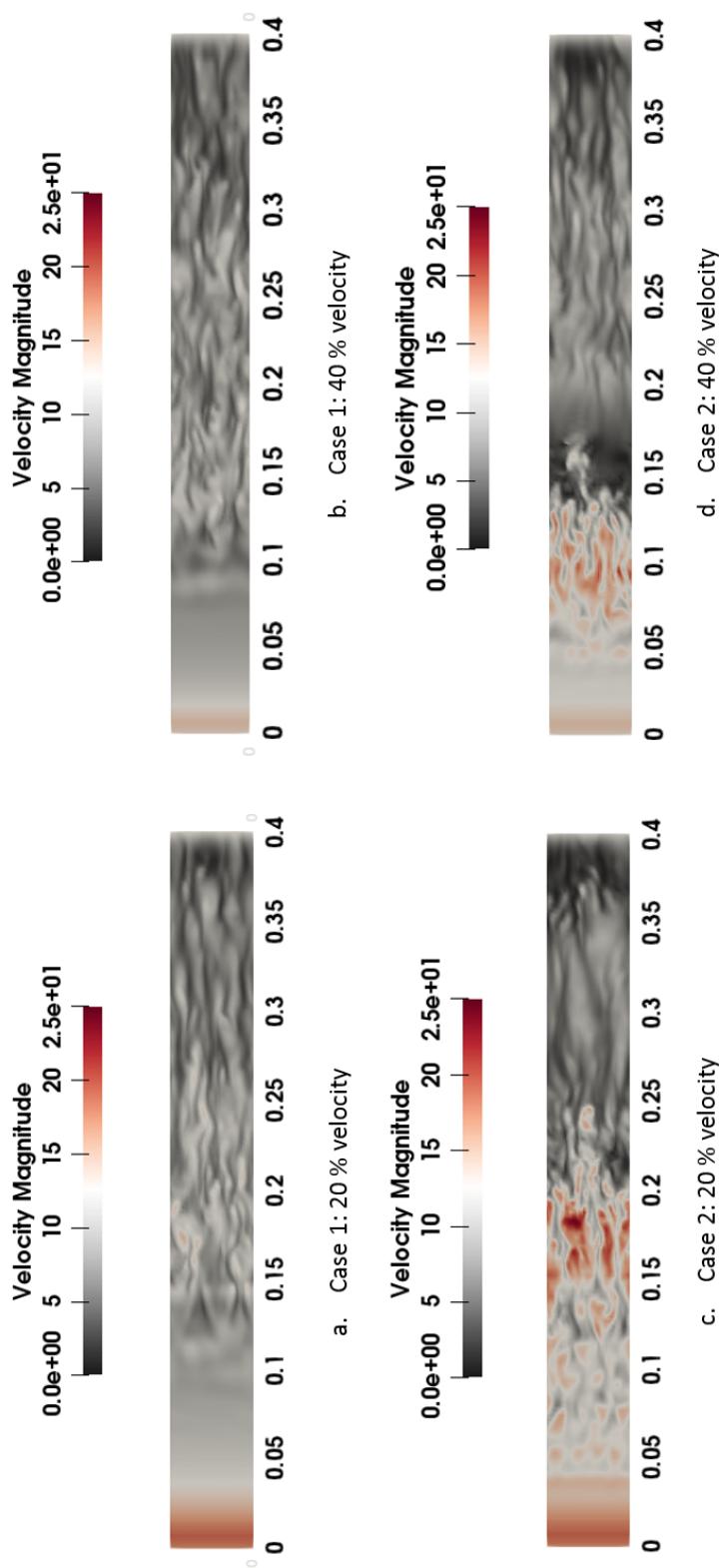


Figure 5.30 Instantaneous velocity in an xz plane at the low peak velocity. Figures at the top present results for  $f = 12Hz$  at  $20\%U_{in}$  (left) and  $40\%U_{in}$  (right), and figures at the bottom presents results for  $f = 50Hz$  at  $20\%U_{in}$  (left) and  $40\%U_{in}$  (right).

## 5.5 Conclusions

A three-dimensional planar incompressible wall-jet, developing in the presence of an external stream, is simulated for unforced and forced velocity profiles. The study is divided into three sections: a refinement study, detailed statistical analysis, and a perturbation parametric analysis. The following conclusions are drawn.

1. Low-resolution simulations compared well qualitatively but not quantitatively, compared to previous studies. They do not capture all the scales of turbulence, classifying them as an under resolved Direct Numerical Simulations.
2. Mean streamwise velocity profiles showed that flow self-similarity is reached after  $x/h=35$  for our high-resolution grids compared to  $x/h=20$  on previous studies, indicating that the sampling area is reduced for statistical analysis.
3. After reaching self-similar behavior ( $x/h > 35$ ), the forced case ( $Sr = 0.0048$ ,  $A = 40\% U_{in}$ ) presents a reduction of the mean coefficient of friction.
4. The high-resolution grids show that mean flow properties are converging for first-order statistics; however, second and third-order turbulent statistics are not fully converged. General trends can however be observed.
5. When increasing the inflow at the top boundary condition from  $2\%U_{in}$  to  $5\%U_{in}$ , the velocity fluctuations appear to be confined to the inner region of the wall-jet which leads to an increase of range for the peak Reynolds stresses in the inner region.
6. The statistical analysis shows that the forced case ( $Sr = 0.0048$ ,  $A = 40\% U_{in}$ ) experiences a decay of maximum velocity at a slower rate than the unforced case.

Turbulent statistics show a reduction in turbulent fluctuations in all directions for the forced case which indicates that the turbulent kinetic energy of the jet is decreasing.

7. Visualizations of the iso-surfaces of the Q-criterion in the outer region of the forced case ( $Sr = 0.0048$ ,  $A = 40\% U_{in}$ ), show the low Strouhal number forcing appears to delay separation from the wall as the wall-jet encounters a cyclic process of re-laminarization. This re-laminarization process is leading to skin friction reduction as the transition region for the flow grows and the billow production by Kelvin-Helmholtz instabilities is reduced in frequency.
8. Cases with forcing at Strouhal number ( $Sr = 0.0048$ ) seem to damp turbulence as the flow becomes more laminar and transition keeps being delayed. At this  $Sr$ , the high amplitude ( $A = 40\% U_{in}$ ) perturbation speeds the process of re-laminarization as the perturbation has a lower velocity at a low peak. The simulation shows that forcing at this Strouhal number and amplitude maybe useful for skin friction reduction applications.
9. Cases at Strouhal number ( $Sr = 0.02$ ) act more like a pulse, supplying frequent big energetic billows and maintaining a chaotic flow over time. At this  $Sr$ , the high amplitude ( $A = 40\% U_{in}$ ) perturbation causes big swirls to interact with each other making the outer layer grow in size at a faster rate than the low amplitude perturbation. Forcing at this Strouhal number and amplitude could be useful for mixing related applications.



## 6. Summary and Future Work

The current work simulates wall-jets flows for two different cases: a two-dimensional compressible wall-jet and a three-dimensional incompressible wall-jet with unforced and forced velocity profiles. The forcing is performed by introducing sine wave perturbation to the inlet velocity at different Strouhal numbers ( $Sr$ ) and amplitudes.

The main takeaways from the compressible case are:

- The velocity fluctuations are affected by the introduction of a cyclic perturbation.

For the case at the low- $Sr$  (0.05), velocity fluctuations increased on the wall-normal direction. For the case at the high- $Sr$  (0.25) the turbulent intensities decrease in all directions.

- The flow encounters an early detachment from the wall. We believe that the size of the physical tripping device height maybe the culprit in the early detachment.

The major findings observed for the three-dimensional incompressible case are:

- The forced velocity profile at low- $Sr$  (0.0048) shows that the flow experiences turbulence damping and becomes overall more laminar while at high- $Sr$  (0.02) the flow has a frequent re-supply of energy that maintains the chaotic complex flow in the downstream.
- The turbulence intensities are confined to the inner region. We suspect that the cause is the increase of inflow at the top boundary condition.

To continue this study of wall-jet flows, the following recommendations should be considered. For the compressible wall-jet simulation:

- The case should be expanded to three dimensions for a comprehensive study of turbulence.

- The tripping device should reduce in height and, consequently, the mesh should be refined to account for the tripping effects.

For the incompressible wall-jet simulation:

- The virtual tripping force should be modified to promote an earlier flow transition to turbulence, thus increasing the available streamwise length of study for the self-similar planar wall-jet.
- To reach convergence in second and third-order statistics, the simulation time needs to be longer for statistical convergence.

Finally, the current results confirm that introducing a sine wave at the initial shear layer of the flow modifies KHI billow production; however, more in-depth analysis is needed to find the optimum Strouhal number and amplitude of the sine wave perturbation to allow for drag reduction and enhancement of mixing. The current measurements focused on the analysis of turbulence transport employing turbulence intensities and triple velocity correlations. Reynolds stresses and turbulent energy budgets should be calculated to further quantitative analysis. The decomposition of Reynolds stresses and turbulent energy provides insightful information regarding energy transfer and turbulence transport between layers. As a final note, a three-dimensional study involving compressible and incompressible cases should be performed, with the same amplitude and Strouhal number forced inlet profiles. This will allow for comparisons of compressibility effects on the flow development and turbulent structures.

## REFERENCES

- Adrian, R. J. (2007). Hairpin vortex organization in wall turbulence. *Physics of Fluids*, 19(4), 041301. doi: 10.1063/1.2717527
- Adrian, R. J., Meinhart, C. D., and Tomkins, C. D. (2000). Vortex organization in the outer region of the turbulent boundary layer. *Journal of Fluid Mechanics*, 422, 1-54. doi: 10.1017/S0022112000001580
- Ahlman, D., Brethouwer, G., and Johansson, A. V. (2007). Direct numerical simulation of a plane turbulent wall-jet including scalar mixing. *Physics of fluids*, 19(6), 065102.
- Ahlman, D., Velter, G., Brethouwer, G., and Johansson, A. V. (2009). Direct numerical simulation of nonisothermal turbulent wall jets. *Physics of fluids*, 21(3), 035101.
- Argonne National Laboratory. (2017). *NEK5000 Version 17.0*. Illinois. (<https://nek5000.mcs.anl.gov>)
- Banyassady, R., and Piomelli, U. (2014). Turbulent plane wall jets over smooth and rough surfaces. *Journal of Turbulence*, 15(3), 186–207.
- Banyassady, R., and Piomelli, U. (2015). Interaction of inner and outer layers in plane and radial wall jets. *Journal of Turbulence*, 16(5), 460-483. doi: 10.1080/14685248.2015.1008008
- Barenblatt, G., Chorin, A., and Prostokishin, V. (2005). The turbulent wall jet: A triple-layered structure and incomplete similarity. *Proceedings of the National Academy of Sciences*, 102(25), 8850–8853.
- Bhatt, S. (2019). Scale interactions within a perturbed plane wall jet.
- Bradshaw, B., and Gee, M. (1962). *Turbulent wall jets with and without an external stream*. Citeseer.
- Chevalier, M., Schlatter, P., Lundbladh, A., and Henningson, D. S. (2007). *Simson: A pseudo-spectral solver for incompressible boundary layer flows*.
- Davidson, P. A., Kaneda, Y., and Sreenivasan, K. R. (2012). *Ten chapters in turbulence*. Cambridge University Press.
- Dejoan, A., and Leschziner, M. (2005). Large eddy simulation of a plane turbulent wall jet. *Physics of Fluids*, 17(2), 025102.
- Eriksson, J. (2003). *Experimental studies of the plane turbulent wall jet* (Unpublished doctoral dissertation). Mekanik.

- Eriksson, J., Karlsson, R., and Persson, J. (1998). An experimental study of a two-dimensional plane turbulent wall jet. *Experiments in fluids*, 25(1), 50–60.
- George, W. K., Abrahamsson, H., Eriksson, J., Karlsson, R. I., Löfdahl, L., and Wosnik, M. (2000). A similarity theory for the turbulent plane wall jet without external stream. *Journal of Fluid Mechanics*, 425, 367–411.
- Glauert, M. (1956). The wall jet. *Journal of Fluid Mechanics*, 1(6), 625–643.
- Gnanamanickam, E. P., Bhatt, S., Artham, S., and Zhang, Z. (2019). Large-scale motions in a plane wall jet. *Journal of Fluid Mechanics*, 877, 239–281.
- Gnanamanickam, E. P., Bhatt, S. B., Artham, S. K., and Zhang, Z. (2017). *Turbulence control by targeting the large-scale motions within boundary layers*.
- Gogineni, S., and Shih, C. (1997). Experimental investigation of the unsteady structure of a transitional plane wall jet. *Experiments in fluids*, 23(2), 121–129.
- Harun, Z., Monty, J. P., Mathis, R., and Marusic, I. (2013). Pressure gradient effects on the large-scale structure of turbulent boundary layers. *Journal of Fluid Mechanics*, 715, 477 - 498. doi: 10.1017/jfm.2012.531
- Holmén, V. (2012). Methods for vortex identification. *Masters Theses in Mathematical Sciences*.
- Hussain, A. F. (1986). Coherent structures and turbulence. *Journal of Fluid Mechanics*, 173, 303–356.
- Huynh, H. T. (2007). A flux reconstruction approach to high-order schemes including discontinuous galerkin methods. In *18th aiaa computational fluid dynamics conference* (p. 4079).
- Irwin, H. P. A. (1973). Measurements in a self-preserving plane wall jet in a positive pressure gradient. *Journal of Fluid Mechanics*, 61(1), 33–63.
- Katz, Y., Horev, E., and Wygnanski, I. (1992). The forced turbulent wall jet. *Journal of Fluid Mechanics*, 242, 577–609.
- Kopriva, D. A. (1998). A staggered-grid multidomain spectral method for the compressible navier–stokes equations. *Journal of computational physics*, 143(1), 125–158.
- Launder, B., and Rodi, W. (1983). The turbulent wall jet measurements and modeling. *Annual Review of Fluid Mechanics*, 15(1), 429–459.
- Mansour, N. N., Kim, J., and Moin, P. (1988). Reynolds-stress and dissipation-rate budgets in a turbulent channel flow. *Journal of Fluid Mechanics*, 194, 15–44.

- Mathews, J., and Fink, K. (2003). *Numerical methods using matlab*. Pearson Prentice Hall.
- Moin, P., and Mahesh, K. (1998). Direct numerical simulation: A tool in turbulence research. *Annual Review of Fluid Mechanics*, 30(1), 539-578. doi: 10.1146/annurev.fluid.30.1.539
- Myers, G., Schauer, J., and Eustis, R. (1963). Plane turbulent wall jet flow development and friction factor. *Journal of Basic Engineering*, 85(1), 47–53.
- Naqavi, I. Z., Tucker, P. G., and Liu, Y. (2014). Large-eddy simulation of the interaction of wall jets with external stream. *International Journal of Heat and Fluid Flow*, 50, 431–444.
- Naqavi, I. Z., Tyacke, J. C., and Tucker, P. G. (2017). A numerical study of a plane wall jet with heat transfer. *International Journal of Heat and Fluid Flow*, 63, 99–107.
- Naqavi, I. Z., Tyacke, J. C., and Tucker, P. G. (2018). Direct numerical simulation of a wall jet: flow physics. *Journal of Fluid Mechanics*, 852, 507–542.
- Narasimha, R., Narayan, K. Y., and Parthasarathy, S. (1973). Parametric analysis of turbulent wall jets in still air. *The Aeronautical Journal*, 77(751), 355–359.
- Offermans, N. (2017). *Towards adaptive mesh refinement in nek5000* (No. 2017:18).
- Patera, A. T. (1984). A spectral element method for fluid dynamics: Laminar flow in a channel expansion. *Journal of Computational Physics*, 54(3), 468 - 488. doi: [https://doi.org/10.1016/0021-9991\(84\)90128-1](https://doi.org/10.1016/0021-9991(84)90128-1)
- Paul F. Fischer, J. W. L., and Kerkemeier, S. G. (2008). *nek5000 Web page*. (<http://nek5000.mcs.anl.gov>)
- Pope, S. B. (2001, oct). Turbulent flows. *Measurement Science and Technology*, 12(11), 2020–2021. doi: 10.1088/0957-0233/12/11/705
- Pouransari, Z., Biferale, L., and Johansson, A. V. (2015). Statistical analysis of the velocity and scalar fields in reacting turbulent wall-jets. *Physics of Fluids*, 27(2), 025102.
- Pouransari, Z., Brethouwer, G., and Johansson, A. V. (2011). Direct numerical simulation of an isothermal reacting turbulent wall-jet. *Physics of fluids*, 23(8), 085104.
- Pouransari, Z., Vervisch, L., Fuchs, L., and Johansson, A. V. (2016, Oct 01). Dns analysis of wall heat transfer and combustion regimes in a turbulent non-premixed wall-jet flame. *Flow, Turbulence and Combustion*, 97(3), 951–969. doi: 10.1007/s10494-016-9716-7

- Pouransari, Z., Vervisch, L., and Johansson, A. V. (2013). Heat release effects on mixing scales of non-premixed turbulent wall-jets: A direct numerical simulation study. *International Journal of Heat and Fluid Flow*, 40, 65–80.
- Pouransari, Z., Vervisch, L., and Johansson, A. V. (2014, Jun 01). Reynolds number effects on statistics and structure of an isothermal reacting turbulent wall-jet. *Flow, Turbulence and Combustion*, 92(4), 931–945. doi: 10.1007/s10494-014-9539-3
- Robinson, S. K. (1991). Coherent motions in the turbulent boundary layer. *Annual Review of Fluid Mechanics*, 23(1), 601–639.
- Rostamy, N., Bergstrom, D., Sumner, D., and Bugg, J. (2011). The effect of surface roughness on the turbulence structure of a plane wall jet. *Physics of Fluids*, 23(8), 085103.
- Saha, P., Biswas, G., Mandal, A., and Sarkar, S. (2017). Investigation of coherent structures in a turbulent channel with built-in longitudinal vortex generators. *International Journal of Heat and Mass Transfer*, 104, 178–198.
- Schlatter, P., and Örlü, R. (2012). Turbulent boundary layers at moderate reynolds numbers: inflow length and tripping effects. *Journal of Fluid Mechanics*, 710, 5-34.
- Schober, M., and Fernholz, H.-H. (2000). Turbulence control in wall jets. *European Journal of Mechanics-B/Fluids*, 19(4), 503–528.
- Schwarz, W. H., and Cosart, W. P. (1961). The two-dimensional turbulent wall-jet. *Journal of Fluid Mechanics*, 10(4), 481–495. doi: 10.1017/S0022112061000299
- Smith, B. S. (2008). *Wall jet boundary layer flows over smooth and rough surfaces* (Unpublished doctoral dissertation). Virginia Tech.
- Sun, Y., Wang, Z. J., and Liu, Y. (2007). High-order multidomain spectral difference method for the navier-stokes equations on unstructured hexahedral grids. *Communications in Computational Physics*, 2(2), 310–333.
- Tachie, M., Balachandar, R., and Bergstrom, D. (2004). Roughness effects on turbulent plane wall jets in an open channel. *Experiments in Fluids*, 37(2), 281–292.
- Tang, Z., Rostamy, N., Bergstrom, D., Bugg, J., and Sumner, D. (2015). Incomplete similarity of a plane turbulent wall jet on smooth and transitionally rough surfaces. *Journal of Turbulence*, 16(11), 1076–1090.
- Tennekes, H., Lumley, J. L., Lumley, J., et al. (1972). *A first course in turbulence*.
- Tomboulides, A., Lee, J., and Orszag, S. (1997). Numerical simulation of low mach number reactive flows. *Journal of Scientific Computing*, 12(2), 139–167.

- Tsai, Y., Hunt, J., Nieuwstadt, F., Westerweel, J., and Gunasekaran, B. (2007). Effect of strong external turbulence on a wall jet boundary layer. *Flow, Turbulence and Combustion*, 79(2), 155.
- Visbal, M., Gaitonde, D., and Gogineni, S. (1998). Direct numerical simulation of a forced transitional plane wall jet. In *29th aiaa, fluid dynamics conference* (p. 2643).
- Witherden, F., Farrington, A., and Vincent, P. (2014). Pyfr: An open source framework for solving advection-diffusion type problems on streaming architectures using the flux reconstruction approach. *Computer Physics Communications*, 185(11), 3028 - 3040. doi: <https://doi.org/10.1016/j.cpc.2014.07.011>
- Witherden, F., Vincent, P., and Jameson, A. (2016). High-order flux reconstruction schemes. In *Handbook of numerical analysis* (Vol. 17, pp. 227–263). Elsevier.
- Wynanski, I., Katz, Y., and Horev, E. (1992). On the applicability of various scaling laws to the turbulent wall jet. *Journal of Fluid Mechanics*, 234, 669–690.
- Zhou, M., Heine, C., and Wynanski, I. (1996). The effects of excitation on the coherent and random motion in a plane wall jet. *Journal of Fluid Mechanics*, 310, 1–37.
- Zhou, M., and Wynanski, I. (1993). Parameters governing the turbulent wall jet in an external stream. *AIAA journal*, 31(5), 848–853.